

UNIVERSITY OF SOUTHAMPTON

FACULTY OF PHYSICAL AND SCIENCES AND ENGINEERING

School of Physics and Astronomy

**The Leading Order Strange Quark-Connected Contribution to the
Muon Anomalous Magnetic Moment From Lattice QCD**

by

Matthew W. Spraggs

Thesis for the degree of Doctor of Philosophy

November 2016

UNIVERSITY OF SOUTHAMPTON

ABSTRACT

FACULTY OF PHYSICAL AND SCIENCES AND ENGINEERING

School of Physics and Astronomy

Doctor of Philosophy

THE LEADING ORDER STRANGE QUARK-CONNECTED CONTRIBUTION TO
THE MUON ANOMALOUS MAGNETIC MOMENT FROM LATTICE QCD

by [Matthew W. Spraggs](#)

I present a calculation of the leading strange quark-connected contribution to the anomalous magnetic moment of the muon, $a_\mu^{(2)\text{had},s}$, using lattice QCD. The calculation is performed on two ensembles with lattice extents of $48^3 \times 96$ and $64^3 \times 128$ with associated inverse lattice spacings of $1.730(4)\text{GeV}$ and $2.359(7)\text{GeV}$. These were generated with the Iwasaki gauge action and 2+1 dynamical quark flavours, which, along with the valence quarks, are represented on the lattice using the Möbius domain wall fermion action. To account for a slight mistuning in the strange quark mass I use both unitary and partially quenched measurements on each ensemble.

I principally use the hybrid method to determine $a_\mu^{(2)\text{had},s}$, and I implement several variations of the method in order to quantify a systematic error associated with the selection of any particular variation. In addition, I use a Fourier transformation to compute the hadronic vacuum polarisation (HVP) at momenta not accessible on the lattice, a technique called sine cardinal interpolation (SCI). All these techniques produce results that are highly consistent with one another. Finite volume corrections are expected to be negligible, since G -parity prevents the strange vector current from coupling to pions in the isospin limit. My final result is

$$a_\mu^{(2)\text{had},s} = 53.1(9)_{(-3)}^{(+1)} \times 10^{-10},$$

where the first error is statistical and the second is systematic. The total error on this result (roughly 2%) is dominated by the statistical uncertainty, which suggests that the methods used here to compute $a_\mu^{(2)\text{had},s}$ in the case of the strange HVP are robust.

Contents

Declaration of Authorship	xiii
Acknowledgements	xv
Nomenclature	xvii
1 Introduction	1
2 The Standard Model	3
2.1 Matter Content	3
2.2 Lagrangian Formulation	6
2.2.1 Quantum Chromodynamics	6
2.2.2 Electroweak Theory	8
2.3 Ward Identities	11
2.4 Symmetries of QCD	13
2.4.1 Chiral Symmetry	13
2.4.2 Isospin Symmetry	15
2.4.3 G -parity	16
3 The Muon Anomalous Magnetic Moment	19
3.1 The QED Vertex Function	19
3.2 Standard Model Contributions	22
3.2.1 Electroweak Theory	22
3.2.2 QCD	24
3.3 The Hadronic Vacuum Polarisation	29
3.3.1 Spectral Representation	30
3.3.2 Vector Ward Identity	33
3.3.3 Ultraviolet Divergence	35
3.4 Euclidean Space Formulation	38
4 Lattice QCD	41
4.1 Discretising QCD	41
4.1.1 Euclidean Path Integrals	41
4.1.2 Field Discretisation	42
4.1.3 Gauge Actions	44
4.1.4 Fermion Actions	45
4.2 Lattice Methodology	46
4.2.1 Ensemble Generation	46

4.2.2	Correlation Functions	48
4.2.3	Quark Sources	51
4.3	Vector Ward Identity	52
4.4	Domain Wall Fermions	54
4.4.1	Chiral Symmetry on the Lattice	54
4.4.2	Continuum	55
4.4.3	Discretisation	57
5	Lattice Computation of $a_{\mu}^{(2)\text{had},s}$	61
5.1	The Hadronic Vacuum Polarisation in Lattice QCD	61
5.1.1	HVP Computation	62
5.1.2	Ensembles and Measurements	64
5.1.3	Source Selection	66
5.2	The Hybrid Method	71
5.2.1	Low- Q^2 Parametrisations	73
5.2.2	Matching at Low- Q^2	76
5.2.3	Integrating the Low- and Mid- Q^2 Regions	79
5.2.4	Integrating the High- Q^2 Region	80
5.3	Sine Cardinal Interpolation	82
5.4	Physical Mass and Continuum Extrapolations	83
5.5	Statistical Error Propagation	84
5.6	Systematic Error Estimation	86
5.6.1	Parametrisation Selection	87
5.6.2	Selection of Momentum Cuts	88
5.6.3	Numerical Integration Technique Selection	89
5.6.4	Sine Cardinal Interpolation Tuning	90
5.6.5	Distribution Results	90
5.6.6	Finite Volume Effects	93
5.7	Final Result	94
6	Conclusions	95
A	The Dirac Gamma Matrices	99
A.1	Pauli Matrices	99
A.2	Minkowski Space	99
A.3	Euclidean Space	100
B	Euclidean Space Integral for the Anomalous Magnetic Moment	101
C	The Källén–Lehmann Representation of the HVP	105
D	The Equivalence of Domain Wall and Overlap Fermions	109
E	Transverse Projectors	113
F	The QCD β-function	117
	References	119

List of Figures

2.1	The matter content of the SM. Note the quark masses as stated here are approximate. The electric charge is given in units of the positron charge, e . The masses of the up, down and strange quarks are given in $\overline{\text{MS}}$ at 2 GeV. The charm and bottom quark masses are given in $\overline{\text{MS}}$ at the scale of the respective quark masses. The top quark mass is that computed directly from experimental measurements.	4
2.2	The three possible vertices permitted by the QCD Lagrangian.	7
2.3	Running behaviour of α_s with energy scale. Taken from [5].	8
3.1	Feynman diagrams for some of the contributions to the muon anomalous magnetic moment. The one-loop QED contribution, or Schwinger term, is given in panel (a) (where the loop boson is a photon). The one-loop contributions from the weak interaction are given in panels (a), (b) and (c) (where the loop boson in (a) is the Z). Panels (d) and (e) contain the diagrams for the LO hadronic contribution, the subject of this work, and the HLbL contribution, respectively.	23
3.2	Cross section data from e^+e^- collisions illustrating the ω resonance (panel (a)) and the ϕ resonance (panel (b)). The shaded green band indicates the result applying the trapezoidal rule within correlated errors. In both cases the number of experimental data points is not sufficient to perform a trapezoidal integration without introducing a bias. Taken from [71]. . .	27
3.3	The two types of possible within the HVP. Panel (a) shows the quark-connected contribution, whilst panel (b) shows the quark-disconnected contribution. For clarity and simplicity I have omitted gluons and additional quark loops from these diagrams, which in panel (b) connect the two quark loops.	29
3.4	An example spectral density function $\rho(\mu^2)$ for an interacting theory. . . .	31
3.5	The contour used in Equation (3.26).	32
3.6	The renormalised photon propagator $D_{\mu\nu}(q)$, written as an infinite series of one-particle-irreducible diagrams.	34
3.7	The one-loop QED vacuum polarisation in Euclidean space, Wick rotated from Equation (3.48) such that $Q^2 = -q^2$. The lepton mass in this case has been set at the mass of the electron.	37
3.8	Plots of the integrand in Equation (3.54) where the one-loop QED vacuum polarisation has been used in place of $\hat{\Pi}$. Panel (a) shows the integrand produced when the vacuum polarisation loop contains an electron, whilst panel (b) shows the integrand when the same loop contains a muon. . . .	39
4.1	Pictorial representations of the Wilson plaquette (left) and rectangle (right) operators.	44

4.2	Quark flow diagrams of a meson two-point function. In the quark-connected diagram in panel (a), a quark-antiquark pair is created by the operator $\bar{\psi}_i(x)\Gamma\psi_j(x)$ at the source point x and propagated to the sink at point y , where the pair is annihilated by the operator $\bar{\psi}_j(y)\Gamma\psi_i(y)$. Panel (b) shows the quark-disconnected contribution, where each particle is created and annihilated at the same quark source. This second case is only possible where the quark flavours i and j are identical.	49
5.1	The strange quark-connected HVPs computed as a result of the two unitary measurements using \mathbb{Z}_2 wall sources described in Table 5.2. The upper plot shows data computed using the 48I ensemble, whilst the lower plot shows data for the 64I ensemble. The corresponding partially quenched HVPs are closely aligned with the unitary data, and so I do not show them here.	67
5.2	The low- Q^2 region of the strange, quark-connected HVPs shown in Figure 5.1. The left-hand plot shows data from the 48I ensemble, whilst the right-hand plot shows data from the 64I ensemble.	68
5.3	Values of $\delta\Pi(\hat{Q}_{\min}^2)$ under various analysis conditions, where $\delta\Pi$ is defined in Equation (5.8). Here \hat{Q}_{\min}^2 refers to the lowest non-zero value of \hat{Q}^2 . Note that the \mathbb{Z}_2 wall sources only provide an improvement over point sources when the ZMS procedure is used.	68
5.4	The first five rows and columns of the covariance matrix of $C_{11}(t, \mathbf{Q} = \mathbf{0})$ (left) and $C_{11}^{\text{ZMS}}(t, \mathbf{Q} = \mathbf{0})$ (right), for both point sources (panel (a)) and \mathbb{Z}_2 wall sources (panel (b)). $C_{11}(t, \mathbf{Q} = \mathbf{0})$ is the original position-space two-point function defined in Equation (5.1), projected to zero spatial momentum with $\mu = \nu = 1$. $C_{11}^{\text{ZMS}}(t, \mathbf{Q} = \mathbf{0})$ is the position-space representation of the HVP correlator at zero spatial momentum, computed with ZMS as defined in Equation (5.10), also with $\mu = \nu = 1$. The data shown here was computed using the unitary strange quark mass on the 48I ensemble.	70
5.5	The distribution of bootstrap values of $\sum_x C_{11}(x)$ where $C_{11}(x)$ was computed using both point and \mathbb{Z}_2 wall sources. This data was computed using unitary strange quark masses on the 48I ensemble.	71
5.6	Schematic overview of the hybrid method, with a sketch of some HVP overlaid with dashed lines denoting the three regions that the integral in Equation (3.54) is partitioned into.	73
5.7	A comparison of the a^2 scaling behaviour of $a_\mu^{(2)\text{had},s}$ when the analysis is performed with either lattice Fourier momenta $Q_\mu = 2\pi n_\mu/L_\mu$ or improved momenta $\hat{Q}_\mu = \frac{2}{a} \sin(aQ_\mu/2)$. Note that in both cases the lattice Fourier transform is performed with respect to the Fourier momentum Q_μ . Panel (a) shows values of $a_\mu^{(2)\text{had},s}$ computed using a χ^2 fit and panel (b) shows values of $a_\mu^{(2)\text{had},s}$ computed using discrete moments. In both cases the HVP form factor was parametrised using an $R_{1,1}$ Padé approximant, with $Q_{\text{low}}^2 = 0.7 \text{ GeV}^2$ and $Q_{\text{high}}^2 = 5.0 \text{ GeV}^2$. Note also that I neglect the effects of the strange quark mass mistuning, presenting results here computed using only unitary strange quark masses.	79

- 5.8 Resulting parametrisation after matching the Padé $R_{1,1}$ (see Equation (5.16)) using a χ^2 fit. The low cut in this case is 0.7 GeV^2 . This curve is typical of the parametrisations generated using the various analytical expressions and matching methods described in this paper. I find that these results typically pass within negligible distance of the lattice data point central values, meaning a fraction of the error on the lattice data points. 80
- 5.9 Effect of the change of variables specified in Equation (5.23) on the form of the integrand in Equation (3.54). In panel (a) I show the integrand before the change of variables (note the logarithmic scale on the x -axis), whilst in panel (b) I show the integrand resulting from the change of variables. The parametrisation is achieved using discrete moments to constrain an $R_{1,1}$ Padé. The red lattice data points are computed using unitary strange data on the 48I ensemble. The blue curves indicate the result of multiplying the constrained parametrisation with the QED kernel. 81
- 5.10 Example continuum and strange quark mass extrapolations. Here δm_s denotes the relative error in the strange quark mass as compared to the physical value. In the continuum limit plot we have subtracted out the variation in the values of $a_\mu^{(2)\text{had},s}$ resulting from the strange quark mass variation, and vice versa. 84
- 5.11 Histograms of a^{-1} for each of the ensembles used in this study, each overlaid with a normal distribution generated using the central value and the associated bootstrap error of the data. The left-hand plot illustrates the distribution of a^{-1} values for the 48I ensemble, whilst the right-hand plot corresponds to the 64I ensemble. 86
- 5.12 Dependence of $a_\mu^{(2)\text{had},s}$ on the number of parameters in the parametrisation used to represent the HVP in the low- Q^2 region. The data here was computed using the 48I ensemble with unitary strange quark masses. Within the hybrid method a fit was used to constrain the parametrisations with a low cut of 0.9 GeV^2 and a high cut of 5.0 GeV^2 88
- 5.13 Dependence of $a_\mu^{(2)\text{had},s}$ on the value of Q_{high}^2 for values computed using unitary strange quark masses on the 48I ensemble. Here I have used the hybrid method, constraining the $R_{1,1}$ parametrisation using discrete time moments with a low cut of 0.7 GeV^2 89
- 5.14 Stacked histograms describing the 73 values of $a_\mu^{(2)\text{had},s}$ computed using the various analysis techniques, colour coded by the low- Q^2 parametrisation (panel (a)), the method used to match these parametrisations (panel (b)), the low- Q^2 cut (panel (c)) and the numerical method used to integrate the mid- Q^2 region (panel (d)). The large grey band illustrates the final statistical error in the result. 91
- 5.15 Dependence of $a_\mu^{(2)\text{had},s}$ on the value of the energy threshold used in the definition of the conformal polynomial. In this figure I show data for the P_3^E parametrisation, constrained using both matching methods with low and high cuts of 0.5 GeV^2 and 5.0 GeV^2 92
- 5.16 Parametrisations resulting from constraining the $P_3^{0.2\text{GeV}}$ parametrisation using both a χ^2 fit (left) and discrete moments (right). In both cases a high cut of 0.5 GeV^2 was used. 92

List of Tables

2.1	Third component of weak isospin T_3 , weak hypercharge Y and electric charge Y for the twelve fermions in the SM.	9
2.2	Isospin quantum numbers of selected low-lying hadronic states.	16
2.3	Isospin, charge conjugation and G -parity quantum numbers of selected low-lying hadronic states in the limit of isospin symmetry.	17
3.1	Contributions to the theoretical value of a_μ compared to the experimental result, along with uncertainties δa_μ [5].	22
3.2	A summary of lattice determinations of $a_\mu^{(2)\text{had}}$ to date. Where two errors are quoted, the first is statistical and the second is systematic. The study of [72] states three values of $a_\mu^{(2)\text{had}}$, each computed using a different lattice volume and spacing. The study of [73] states two values of $a_\mu^{(2)\text{had}}$, with the difference lying in the ansatz used to extrapolate to the physical light quark mass.	28
5.1	Properties of the ensembles used in this study [9].	64
5.2	Summary of measurements performed in this study. Propagators on a single configuration use sources on different timeslices evenly spaced along the temporal extent, starting at $t = 0$	66

Declaration of Authorship

I, [Matthew W. Spraggs](#) , declare that the thesis entitled *The Leading Order Strange Quark-Connected Contribution to the Muon Anomalous Magnetic Moment From Lattice QCD* and the work presented in the thesis are both my own, and have been generated by me as the result of my own original research. I confirm that:

- this work was done wholly or mainly while in candidature for a research degree at this University;
- where any part of this thesis has previously been submitted for a degree or any other qualification at this University or any other institution, this has been clearly stated;
- where I have consulted the published work of others, this is always clearly attributed;
- where I have quoted from the work of others, the source is always given. With the exception of such quotations, this thesis is entirely my own work;
- I have acknowledged all main sources of help;
- where the thesis is based on work done by myself jointly with others, I have made clear exactly what was done by others and what I have contributed myself;
- parts of this work have been published as: [\[1,2\]](#)

Signed:.....

Date:.....

Acknowledgements

I would like to thank my supervisor Andreas Jüttner for all the help and advice he has given me over the course of my PhD. I also wish to thank Antonin Portelli for his patient guidance during my work on the HVP and $g - 2$.

I also wish to thank my colleagues in the RBC/UKQCD $g - 2$ subgroup for their input into this project, namely Tom Blum, Peter Boyle, Luigi Del Debbio, Jamie Hudspith, Taku Izubuchi, Christoph Lehner, Randy Lewis, Kim Maltman and Marina Krstić Marinkovic.

Financially I am supported by EPSRC Doctoral Training Centre grant (EP/G03690X/1).

Thanks also to all those I shared an office with in room 4007 for being great fun and putting up with my inane physics-related questions.

Finally I thank Miranda, whose love and support means more than I can say.

Nomenclature

BSM	Beyond Standard Model
DWF	Domain Wall Fermion
EWSB	Electroweak Symmetry Breaking
FV	Finite Volume
HLbL	Hadronic Light-by-Light
HVP	Hadronic Vacuum Polarisation
LO	Leading Order
MDWF	Möbius Domain Wall Fermion
NLO	Next-to-leading Order
QCD	Quantum Chromodynamics
QED	Quantum Electrodynamics
SCI	Sine Cardinal Interpolation
SM	Standard Model
SSB	Spontaneous Symmetry Breaking
UV	Ultraviolet
ZMS	Zero-mode Subtraction

Chapter 1

Introduction

The detection of a Higgs-like boson during the summer of 2012 [3, 4] completed the experimental verification of the particle content of the Standard Model of particle physics (SM). However, various questions remain that the SM cannot account for, both conceptually and experimentally [5]. For example:

- What is the nature of dark matter?
- Is dark energy a cosmological constant or a scalar field?
- Why do neutrinos oscillate?
- Do the three interactions of the SM unify at some energy scale? Can this be formulated as a grand unified theory?
- Can general relativity be reconciled with quantum mechanics?

Although this is by no means an exhaustive list, it illustrates the magnitude of the task that physicists still face in trying to understand the universe.

In this thesis I consider the anomalous magnetic moment of the muon, a_μ . Historically there has been a persistent tension between the theoretical and experimental determinations of this quantity, though not at the level of statistical significance required to indicate the presence of new physics [5, 6]. With new experiments at both Fermilab [7] and J-PARC [8] set to reduce the uncertainty in the experimental determination of this quantity, there is growing pressure on physicists to reduce the error in the theoretical determination. The majority of the uncertainty in this quantity comes from the various hadronic contributions, indicating where efforts should be concentrated when refining the theoretical determination of a_μ .

Much of the difficulty in computing the hadronic contributions to a_μ from first principles lies in the non-perturbative nature of quantum chromodynamics (QCD) at low energies,

which renders perturbative techniques unreliable [6]. Lattice QCD, however, is a non-perturbative technique capable of computing hadronic effects at energies inaccessible to perturbation theory. The method is computationally intensive, with some calculations taking several months to complete. Advances in algorithms, developments in field theory and increases in computing power over the past decade mean that calculations using lattice QCD can now be done using physical quark masses [9–15], simplifying calculations significantly and minimising systematic errors. These advances also facilitate results with smaller statistical errors. In this work I apply lattice QCD to the computation of the leading order strange contribution to a_μ . This calculation forms part of a wider program within the RBC/UKQCD collaboration to compute both the leading order (LO) hadronic and hadronic light-by-light (HLbL) contributions to a_μ , which in combination are responsible for most of the error on the total value of this quantity. I discuss these two contributions in more detail in Chapter 3.

In Chapter 2 I briefly review the SM, focussing in particular on QCD and some of its associated symmetries. A discussion of Ward identities, which are of particular relevance to the present work, is also included.

In Chapter 3 I introduce the muon anomalous magnetic moment through a consideration of the QED vertex function. This is followed by a discussion of the various contributions to a_μ . The rest of the chapter is dedicated to the hadronic vacuum polarisation (HVP), which describes the hadronic contribution to the photon self-energy and is central in the computation of the LO hadronic contribution to a_μ .

In Chapter 4 I discuss lattice QCD as a discretised formulation of QCD. An overview of both gauge and fermionic lattice actions is included, along with some of the difficulties in translating continuum QCD to the lattice. I also provide some discussion of how lattice QCD is performed in practice.

In Chapter 5 I present the calculation of the leading strange contribution to the muon anomalous magnetic moment, $a_\mu^{(2)\text{had},s}$. The method used to compute the HVP in this work is first detailed. I then proceed to discuss how $a_\mu^{(2)\text{had},s}$ is computed from the HVP, using several analysis methods to better understand the systematic effects associated with the selection of any particular technique. A detailed discussion of each aspect of these methods is included, from which I derive a systematic uncertainty on the final computed value of $a_\mu^{(2)\text{had},s}$.

In Chapter 6 I present my conclusions, putting my result in context and discussing the outlook for the computation of $a_\mu^{(2)\text{had}}$ on the lattice.

Chapter 2

The Standard Model

The Standard Model (SM) is currently the most successful theory in our attempts to understand the fundamental particles that exist in nature and their interactions with one another. It describes three of the four known fundamental forces of nature, namely the electromagnetic, weak and strong interactions, and has proven remarkably robust when subject to experimental tests [3–5]. Despite this, it has several shortcomings, notably the assumption that neutrinos are massless, which has since been shown to be false through the existence of neutrino oscillations that mix flavour and mass eigenstates [16, 17]. Whilst there are various other tensions between the SM and experimental measurements, none has reached the 5σ level of statistical significance required to be classed as a discovery [5].

In this chapter I will introduce the various elements of the SM that feed into this work. I will begin by describing the matter content of the SM in Section 2.1, followed by a description of the various components of its Lagrangian and their associated gauge symmetries in Section 2.2. This is followed by a discussion of Ward identities in Section 2.3, which describe how quantities within the SM are conserved. Finally, I follow this with a description of the symmetries of quantum chromodynamics (QCD) in Section 2.4.

2.1 Matter Content

The SM contains seventeen fundamental particles (see Figure 2.1) [5]. These particles can be subdivided into two categories: fermions, which have spin $\frac{1}{2}$, and bosons, which have integral spin. The fermions account for the matter content of the SM, whilst the bosons act as mediators of the three interactions the theory describes. The behaviours of these two types of particle are also distinctive: bosonic fields are commutative, whilst fermionic fields are anti-commutative. This latter result can be shown to produce the Pauli exclusion principle, whereby no two fermions with the same quantum numbers may

	Mass → 2.3 MeV Charge → +2/3 Spin → 1/2 u	1.275 GeV +2/3 1/2 c	173.21 GeV +2/3 1/2 t	0 0 1 g	125.7 GeV 0 1 H
QUARKS	4.8 MeV -1/3 1/2 d	95 MeV -1/3 1/2 s	4.18 GeV -1/3 1/2 b	0 0 1 γ	
LEPTONS	0.511 MeV -1 1/2 e	105.7 MeV -1 1/2 μ	1.777 GeV -1 1/2 τ	91.2 GeV 0 1 Z	
	< 2 eV 0 1/2 ν_e	< 0.19 MeV 0 1/2 ν_μ	< 18.2 MeV 0 1/2 ν_τ	80.4 GeV 1 1 W	VECTOR BOSONS

Figure 2.1: The matter content of the SM. Note the quark masses as stated here are approximate. The electric charge is given in units of the positron charge, e . The masses of the up, down and strange quarks are given in \overline{MS} at 2 GeV. The charm and bottom quark masses are given in \overline{MS} at the scale of the respective quark masses. The top quark mass is that computed directly from experimental measurements.

coexist. Fermions therefore obey Fermi-Dirac statistics. Bosons, on the other hand, are not constrained in this way, instead obeying Bose-Einstein statistics. In addition, the fundamental fermionic particles can exist as either particles or anti-particles, whilst for the bosons there is no such distinction. The possible exception to this classification are the neutrinos, as the question remains over whether or not neutrinos are their own anti-particles [18]. Anti-particles possess the same mass but opposite charge (including electric charge) to their respective particles.

The behaviour of the fields of the SM under Lorentz transformations can be further used to classify their spin structure [19]. The Lorentz algebra can be related to the algebra of $SU(2)$ through the latter being a double cover of $SO(3)$. Taken in combination with the Weyl representation of spinors, this allows for the transformation properties of a field to be described using two multiples of $\frac{1}{2}$. For the fundamental fields of the standard model the four relevant categorisations are:

- $(0, 0) \rightarrow$ scalar field;
- $(\frac{1}{2}, 0) \rightarrow$ left-handed spinor field;
- $(0, \frac{1}{2}) \rightarrow$ right-handed spinor field;
- $(\frac{1}{2}, \frac{1}{2}) \rightarrow$ vector field.

These categories introduce the notion of *handedness* or *chirality*, which, as I will later describe, plays an important role in both the weak interaction and chiral symmetry.

The twelve fermions of the SM can be further divided into quarks and leptons. The quarks interact via all three interactions described by the SM (weak, electromagnetic and strong). In units of the positron charge e , the up-type quarks, the up, charm and top, have charge $+\frac{2}{3}$, whilst the down-type quarks, the down, strange and bottom, have charge $-\frac{1}{3}$. There is also a mass hierarchy among the three different flavours of these two quark types, which naturally separates them into three generations. The up, charm and top quarks have masses of $2.3({}_{-5}^{+7})$ MeV, $1.275(25)$ GeV and $173.21(87)$ GeV respectively, whilst the down, strange and bottom quarks have masses $4.8({}_{-3}^{+5})$ MeV, $95(5)$ MeV and $4.18(3)$ GeV, respectively¹ [5]. Finally, quarks possess a colour charge, one of red, green or blue, which allows them to interact via the strong interaction. Unlike electromagnetism and the weak interaction, the strong interaction appears to forbid particles with a net colour charge, with the result that quarks only form colour singlet states. This phenomenon is known as colour confinement.

The leptons of the SM are also divided into three generations. Similarly to quarks there are two distinct types: the electron-like fermions with non-zero electric charge and the neutrinos with zero electric charge. The electron, muon and tau particles all have electric charge $-e$ and interact via both the electromagnetic and weak interactions and have masses [5]

$$m_e = 0.510998928(11) \text{ MeV}, \quad (2.1)$$

$$m_\mu = 105.6583715(35) \text{ MeV}, \quad (2.2)$$

$$m_\tau = 1776.82(12) \text{ MeV}. \quad (2.3)$$

The neutrinos interact only via the weak interaction, and within the SM are considered to be massless. In reality they satisfy the mass constraints $m_{\nu_e} < 2 \text{ eV}$, $m_{\nu_\mu} < 0.19 \text{ MeV}$ and $m_{\nu_\tau} < 18.2 \text{ MeV}$ [5].

The three forces accounted for by the SM are mediated by the four gauge bosons within it. The electromagnetic interaction is mediated by the photon, the weak by the Z and W^\pm bosons and the strong by the gluon. Of these interactions, only the electromagnetic has infinite range, since the W^\pm and Z are massive, giving them a finite lifetime, and the gluon possesses a colour charge, making it subject to colour confinement. The weak interaction is unusual in that it acts only on left-handed particles, meaning the theory of the weak interaction is not invariant under parity.

The final particle of the seventeen within the SM is the Higgs boson, which, through spontaneous symmetry breaking, gives mass to the W^\pm and Z . The discovery of a scalar

¹Here the up, down and strange masses are the “current-quark masses” defined in $\overline{\text{MS}}$ at 2 GeV. The charm and bottom masses are the “running masses”, defined in $\overline{\text{MS}}$ at the scale of the quark mass. The top quark mass is that computed directly from experimental measurements.

boson at the LHC in 2012 with properties akin to the hypothesised Higgs boson [3, 4] is one of the great triumphs of particle physics in recent years.

2.2 Lagrangian Formulation

The SM exhibits a local $SU(3)_C \times SU(2)_L \times U(1)_Y$ gauge symmetry. The respective groups correspond to the conservation of colour charge, weak isospin and weak hypercharge. Here I introduce the Lagrangians that respect the conservation of these quantities.

2.2.1 Quantum Chromodynamics

The conservation of colour charge relates exclusively to the strong interaction, which is understood through the theory of quantum chromodynamics (QCD). The QCD Lagrangian has the form [20]

$$\mathcal{L}_{\text{QCD}} = \sum_f \bar{q}_f(x) (\mathbf{i}\not{D} - m_f) q_f(x) - \frac{1}{4} F_{\mu\nu}^a F_a^{\mu\nu}, \quad (2.4)$$

where q_f is the quark field of quark flavour f , \bar{q}_f is the corresponding anti-quark field, γ^μ are the Dirac matrices, whose properties I summarise in Appendix A, and m_f is the mass of quark flavour f . Feynman slash notation has been used such that $\not{D} = \gamma^\mu D_\mu$. The summation is over the six quark flavours in the standard model. Einstein summation convention has been used for the Lorentz indices μ and ν and the $SU(3)$ colour indices a, b and c . The objects D_μ and $F_{\mu\nu}^a$ are the covariant derivative and gluon field strength tensor, respectively, given by

$$D_\mu = \partial_\mu + \mathbf{i}g_s A_\mu(x), \quad A_\mu(x) = \frac{1}{2} \lambda_a A_\mu^a(x), \quad (2.5)$$

and

$$F_{\mu\nu}^a = \partial_\mu A_\nu^a(x) - \partial_\nu A_\mu^a(x) - g_s f^{abc} A_{\mu,b}(x) A_{\nu,c}(x), \quad (2.6)$$

where g_s is the strong coupling constant, λ_a are the Gell-Mann matrices, which produce the generators of the $SU(3)$ gauge group, $\frac{1}{2} \lambda_a$. $A_\mu^a(x)$ is the gauge field and f^{abc} are the structure constants for the gauge group.

The gauge field A_μ^a is required to preserve the gauge symmetry of the Lagrangian under $SU(3)$ colour rotations. Mathematically, if we transform the quark fields using a local $SU(3)$ transformation, such that $q'(x) = g(x)q(x)$, where $g(x)$ is some member of $SU(3)$, then we require that the gauge field transforms under the adjoint representation, such that

$$A_\mu(x) \rightarrow A'_\mu(x) = g(x)A_\mu(x)g^\dagger(x) + \frac{\mathbf{i}}{g_s} (\partial_\mu g(x))g^\dagger(x), \quad (2.7)$$

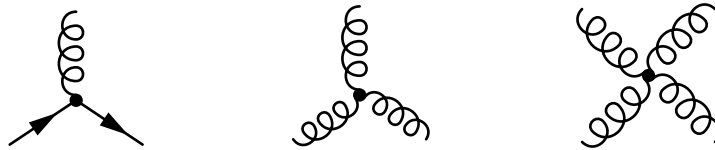


Figure 2.2: The three possible vertices permitted by the QCD Lagrangian.

and

$$F_{\mu\nu}(x) \rightarrow F'_{\mu\nu}(x) = g(x)F_{\mu\nu}(x)g^\dagger(x). \quad (2.8)$$

Transforming the quark and gauge fields in this way leaves the Lagrangian invariant. This symmetry corresponds to the conservation of colour at a point. I shall outline the relationship between symmetries and conservation laws in Section 2.3.

From Equations (2.4), (2.5) and (2.6) it is apparent that there are three possible vertex Feynman rules in QCD. In addition to the fermion-gluon three-point vertex, the non-abelian nature of the QCD gauge group allows for gluon self-interactions. The associated three- and four-point vertices are illustrated in Figure 2.2, along with the fermion-gluon vertex.

The non-perturbative nature of QCD at low energies, however, is not obvious from the Lagrangian of Equation (2.4). The renormalised theory dictates that the coupling constant g_s is scale dependent such that $g_s \sim \mathcal{O}(1)$ in this regime. Specifically, the renormalised QCD Lagrangian requires that $\alpha_s = g_s^2/4\pi$ obeys the following differential equation

$$\mu^2 \frac{d\alpha_s}{d\mu^2} = \beta(\alpha_s(\mu^2)), \quad (2.9)$$

where μ is the renormalisation scale and β is the QCD β -function, which is negative at one-loop in perturbation theory (see Appendix F). As a consequence of this, QCD is *asymptotically free* [21, 22], such that $\alpha_s \rightarrow 0$ as $\mu \rightarrow \infty$ (see Figure 2.3). Integrating this equation also reveals that $\alpha_s \sim \mathcal{O}(1)$ at low energies. As an immediate consequence, perturbative approaches are unreliable in this regime, meaning non-perturbative techniques such as lattice QCD are required to compute observable quantities at low energy scales. In addition, quarks exhibit confinement, meaning isolated quarks and gluons are unobservable at low energies. A corollary of this phenomenon is that QCD exhibits a *mass gap*, meaning that there is a non-zero difference between the energy of the vacuum and the lowest-lying QCD state. Asymptotic freedom and confinement give rise to a plethora of complex behaviour, whereby the quarks within the SM produce a vast zoo of hadronic states. Rather than seeking to understand a given phenomenon via the fundamental degrees of freedom of QCD (quarks and gluons), one must instead consider it via the spectrum of hadrons associated with the given interaction.

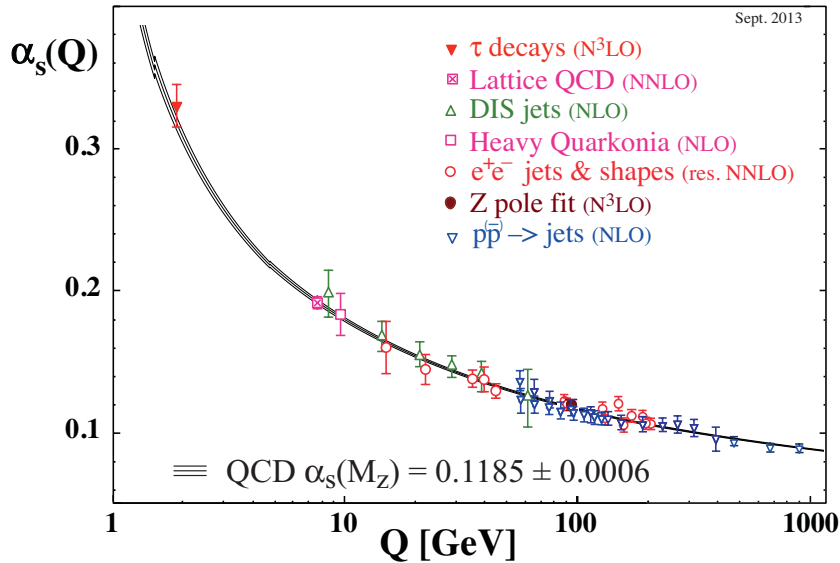


Figure 2.3: Running behaviour of α_s with energy scale. Taken from [5].

2.2.2 Electroweak Theory

The remaining $SU(2)_L \times U(1)_Y$ symmetry relates to the electroweak theory that describes the electromagnetic and weak interactions. The W^\pm vector bosons couple to only left-handed fermions, and as such these can be grouped together into $SU(2)$ doublets [23–25]. For example in the case of leptons

$$\Psi_{L,i} = \begin{pmatrix} \nu_{L,i} \\ \ell_{L,i} \end{pmatrix}, \quad (2.10)$$

where ν and ℓ are neutrino and charged lepton spinors, respectively, of the same generation i . A similar set of doublets exist for the three quark generations, with up-type quarks paired with down-type quarks of the same generation. The right-handed counterparts to these particles form singlets under $SU(2)$, since right-handed particles do not couple to the W^\pm . I will label these singlets $\Psi_{R,i}$, or where necessary by the type of particle, i.e. charged lepton as $\ell_{R,i}$, up-type quark as $u_{R,i}$ and down-type quark as $d_{R,i}$. The doublets transform under the $SU(2)_L \times U(1)_Y$ gauge symmetry as

$$\Psi_{L,i} \rightarrow \Psi'_{L,i} = U_L U_Y \Psi_{L,i}, \quad (2.11)$$

where U_L and U_Y are local $SU(2)$ and $U(1)$ group elements, respectively. Explicitly:

$$U_L(x) = e^{i\omega_i(x)\tau^i} \quad \text{and} \quad U_Y(x) = e^{i\omega_0(x)\frac{Y}{2}}, \quad (2.12)$$

where Y is the weak hypercharge that generates the $U(1)$ group, ω_0 and ω_i are spacetime-dependent transformation parameters, $\tau^i = \frac{1}{2}\sigma^i$ are the generators of $SU(2)$, and σ^i are the Pauli matrices, which I define in Appendix A. The generators obey the following Lie

Particles	T_3	Y	Q
e_L, μ_L, τ_L	$-1/2$	-1	-1
e_R, μ_R, τ_R	0	-2	-1
$\nu_{e,L}, \nu_{\mu,L}, \nu_{\tau,L}$	$+1/2$	-1	0
u_L, c_L, t_L	$+1/2$	$+1/3$	$+2/3$
u_R, c_R, t_R	0	$+4/3$	$+2/3$
d_L, s_L, b_L	$-1/2$	$+1/3$	$-1/3$
d_R, s_R, b_R	0	$-2/3$	$-1/3$

Table 2.1: Third component of weak isospin T_3 , weak hypercharge Y and electric charge Y for the twelve fermions in the SM.

algebra:

$$[\tau^i, \tau^j] = i\epsilon_{ijk}\tau^k, \quad (2.13)$$

where ϵ_{ijk} is the rank three Levi–Civita tensor. The weak hypercharge Y is related to the electric charge Q and the third component of weak isospin T_3 via

$$Q = T_3 + \frac{Y}{2}. \quad (2.14)$$

A table of these values for the twelve SM fermions is given in Table 2.1. The right-handed singlets $\Psi_{R,i}$ transform similarly under $U(1)_Y$:

$$\Psi_{R,i} \rightarrow \Psi'_{R,i} = U_Y \Psi_{R,i}. \quad (2.15)$$

From Table 2.1, it should be apparent that these singlets do not transform in the same way as the left-handed doublets under $U(1)_Y$. The Lagrangian for the electroweak interaction must be constructed such that it remains invariant under these transformations.

Within the SM, the Weinberg–Salam theory of electroweak interactions posits that the vector bosons of the theory are all massless above the scale of electroweak symmetry breaking (EWSB) [23–25]. The W^\pm and Z bosons gain their mass through the Higgs mechanism, a form of spontaneous symmetry breaking [26–29]. Before this process occurs, the electroweak Lagrangian takes the form

$$\mathcal{L}_{\text{EW}} = \sum_i [\bar{\Psi}_{L,i}(i\not{D})\Psi_{L,i} + \bar{\Psi}_{R,i}(i\not{D})\Psi_{R,i}] \quad (2.16a)$$

$$- \frac{1}{4}B_{\mu\nu}B^{\mu\nu} - \frac{1}{4}W_{\mu\nu}^a W_a^{\mu\nu} \quad (2.16b)$$

$$+ (D_\mu\Phi)^\dagger D^\mu\Phi - \lambda \left(\Phi^\dagger\Phi - \frac{v^2}{2} \right)^2 \quad (2.16c)$$

$$- \sum_i \left[y_i^\ell (\Psi_{L,i}^\dagger \Phi^c) \ell_{R,i} + \text{h.c.} \right] \quad (2.16d)$$

$$- \sum_{i,j} \left[y_{ij}^u (\Psi_{L,i}^\dagger \Phi) u_{R,j} + y_{ij}^d (\Psi_{L,i}^\dagger \Phi^c) d_{R,j} + \text{h.c.} \right], \quad (2.16e)$$

where the sums over the indices i and j run over the three generations in the SM. Much is encoded in this Lagrangian, so I will briefly explain what each line represents. The first line contains the following covariant derivative:

$$D_\mu \Psi_{L,i} = \left[\partial_\mu + i\frac{g}{2}W_\mu + i\frac{g'}{2}B_\mu \right] \Psi_{L,i}, \quad (2.17)$$

$$D_\mu \Psi_{R,i} = \left[\partial_\mu + i\frac{g'}{2}B_\mu \right] \Psi_{R,i}, \quad (2.18)$$

where $W_\mu = W_\mu^k \tau_k$ and B_μ are the $SU(2)_L$ and $U(1)_Y$ vector boson fields that, through EWSB, produce the three electroweak vector bosons in the SM. Hence the covariant derivative describes the coupling between these bosons and the fermions of the SM. To preserve the form of these terms, the gauge fields must transform like

$$B_\mu \rightarrow B'_\mu = B_\mu + \frac{2}{g'} \partial_\mu \omega_0, \quad (2.19)$$

$$W_\mu \rightarrow W'_\mu = U_L W_\mu U_L^\dagger + \frac{2i}{g} (\partial_\mu U_L) U_L^\dagger, \quad (2.20)$$

where ω_0 and U_L are specified in Equation (2.12). The next line in the Lagrangian (line (2.16b)) contains terms that are dependent solely on the gauge fields of the theory. The field strength tensors $B_{\mu\nu}$ and $W_{\mu\nu}^a$ may be written

$$B_{\mu\nu} = \partial_\mu B_\nu - \partial_\nu B_\mu, \quad (2.21)$$

$$W_{\mu\nu}^a = \partial_\mu W_\nu^a - \partial_\nu W_\mu^a - \frac{g}{2} \epsilon^{abc} W_{\mu b} W_{\nu c}. \quad (2.22)$$

This line therefore describes the kinetic behaviour of the gauge bosons. In a manner similar to QCD, the $W_{\mu\nu}^a$ also describes the self-interaction of the three W_μ^a bosons. From Equation (2.19) it should be obvious that the tensor $B_{\mu\nu}$ is invariant under $U(1)_Y$. The tensor $W_{\mu\nu}$ transforms as

$$W_{\mu\nu} \rightarrow W'_{\mu\nu} = U_L W_{\mu\nu} U_L^\dagger, \quad (2.23)$$

which under the trace in the action preserves the form of the pure gauge terms.

The third line of the Lagrangian contains the Higgs doublet Φ , which can be written explicitly as

$$\Phi = \begin{pmatrix} \phi_1 + i\phi_2 \\ \phi_3 + i\phi_4 \end{pmatrix}, \quad (2.24)$$

where $\phi_{1,2,3,4}$ are four, real-valued fields. The kinetic term $D_\mu \Phi^\dagger D^\mu \Phi$ describes the coupling between the Higgs boson and the four fields W_μ^a and B_μ , with D_μ acting on Φ in the same way as it acts upon $\Psi_{L,i}$. The potential is quartic in the Higgs doublet with a set of minima where $\Phi^\dagger \Phi = v^2/2$. The variable v is the vacuum expectation value (VEV) of the Higgs field. In the present formulation of the Lagrangian there is no constraint on the four real values that make up the Higgs doublet. Under the $SU(2)_L \times U(1)_Y$ gauge

symmetry, the Higgs doublet transforms in a manner identical to the fermion doublets:

$$\Phi \rightarrow \Phi' = U_Y U_L \Phi. \quad (2.25)$$

After EWSB, the field Φ is constrained at a particular minimum and the Lagrangian is expanded around this value. Introducing the real-valued fields ρ , σ , τ and h , which describe the perturbation of the Higgs doublet around the VEV, the $SU(2)_L$ gauge symmetry is spontaneously broken by setting $\phi_1(x) = \rho(x)$, $\phi_2(x) = \sigma(x)$, $\phi_3(x) = v + h(x)/\sqrt{2}$ and $\phi_4(x) = \tau(x)$. As a result of this process, line (2.16c) in Equation (2.16) changes significantly and mass terms for the W^\pm and Z are created. Specifically, the kinetic term becomes

$$(D_\mu \Phi)^\dagger D^\mu \Phi \stackrel{\text{EWSB}}{=} \frac{1}{2} \partial_\mu h \partial^\mu h + \frac{(g')^2}{2} W_\mu^- W^{+\mu} (v + h/\sqrt{2})^2 + \frac{1}{4} (g^2 + (g')^2) Z_\mu Z^\mu (v + h/\sqrt{2})^2, \quad (2.26)$$

where I have absorbed the fields ρ , σ and τ into the Higgs doublet using a unitary transformation.

The final two lines in the Lagrangian contain the Yukawa couplings that give masses to the fermions of the SM. The object Φ^c is defined by

$$\Phi^c = i\sigma^2 \Phi^*. \quad (2.27)$$

Of particular interest are the Yukawa couplings y_{ij}^u and y_{ij}^d . Unlike in the lepton case², mixing can occur between the various quark generations. This gives rise to the Cabibbo-Kobayashi-Maskawa (CKM) matrix, which describes how quark flavour and mass eigenstates mix through weak interactions [30, 31].

2.3 Ward Identities

In classical field theory, symmetries and conservation laws are related to one another via Noether's theorem [32, 33], which states that the invariance of a theory's Lagrangian under some differentiable transformation requires the existence of some conserved current. Noether's theorem also applies in quantum field theory, and Ward identities arise when considering symmetry transformations in the context of operators. Since conserved quantities are found throughout both QCD and particle physics in general, I will now outline how Noether's theorem is used to derive conserved currents and associated Ward identities. This will be useful when I come to discuss the symmetries of QCD in the next section and the vector Ward identity in the next chapter, where I will discuss

²Neutrino oscillations imply mixing between neutrino mass and flavour eigenstates. However, this is not accounted for in the SM, and so I omit it from the present discussion.

the transversality of the hadronic vacuum polarisation (HVP). The HVP is an essential ingredient in the computation of the LO hadronic contribution to a_μ .

In quantum field theory the expectation value of some operator O can be defined using the path integral formalism. If we consider some general field theory with a set of fields $\phi_a(x)$, then the expectation value of O can be computed as

$$\langle O \rangle = \frac{1}{Z} \int \mathcal{D}\phi O e^{iS[\phi_a]}, \quad (2.28)$$

where the integration measure $\mathcal{D}\phi = \prod_a \mathcal{D}\phi_a$, $Z = \langle \cdot \rangle$ is the expectation value of the vacuum and S is the action for the theory in question. We can then consider the result of applying a symmetry transformation to one of the fields, such that $\phi_a \rightarrow \phi'_a = \phi_a + \delta\phi_a$. The transformation parameter(s) on which the perturbation $\delta\phi_a$ depends can be taken to be spacetime-dependent parameter(s) in the first instance such the transformation is local. The Ward identity corresponding to a global symmetry can then be taken as the limiting case where the transformation parameter(s) are constant in spacetime. For the rest of this discussion I will assume that such a transformation can be encoded via the local parameter $\alpha(x)$.

These generalised field transformations carry the possibility of altering the integration measure used in the path integral. In these cases the Jacobian of the transformation must be computed and incorporated into the transformed expectation value. This process introduces an anomaly into the resulting Ward identity. One example of this is the axial anomaly arising from applying an axial transformation to the path integral [34,35]. Ignoring this possibility for the moment and assuming the integration measure is invariant under the aforementioned transformation, one arrives at the following relationship

$$\langle \delta O \rangle + i \langle O \delta S \rangle = 0. \quad (2.29)$$

We therefore require

$$\left\langle O \frac{\delta S}{\delta \alpha(x)} \right\rangle = i \left\langle \frac{\delta O}{\delta \alpha(x)} \right\rangle, \quad (2.30)$$

where I have introduced functional derivatives that will act to remove the α -dependence from the final expression. Specifically, since $\frac{\delta \alpha(y)}{\delta \alpha(x)} = \delta^{(4)}(y-x)$, a functional derivative has the effect of introducing a delta function into the expression for the action. The integral over spacetime within the action then acts to select a specific spacetime coordinate.

The invariance of $\langle O \rangle$ under a transformation of the fields of the theory can be used to derive an expression for the associated conserved current, whose conservation is trivially realised by selecting $O = \mathbb{1}$. Importantly, such derivations are not restricted to local symmetries of the Lagrangian, which would limit the discussion to gauge symmetries alone. Instead, it is possible to promote global symmetries to local symmetries for the

purpose of the derivation with the understanding that the limit of constant transformation parameters is taken later. Indeed, this technique will be of great relevance in the following section, where I discuss global symmetries of the QCD Lagrangian. Depending on the choice of the operator O or the nature of the symmetry transformation, the resulting Ward identity in Equation (2.30) may have a non-zero right-hand side.

2.4 Symmetries of QCD

Besides gauge symmetry, which is enforced by introducing a gauge field into the Lagrangian, QCD also possesses various other symmetries. Through Noether's theorem, these symmetries will have associated conserved currents. In addition, the behaviour of the various states of QCD under these symmetry transformations allows the former to be categorised in a phenomenologically relevant manner. Several of the accidental symmetries are also relevant to the present work, and these I will describe in this section.

2.4.1 Chiral Symmetry

We can define the positive and negative chirality projection operators $P_{\pm} = \frac{1}{2}(1 \pm \gamma^5)$, which can be used to project out the right- and left-handed components of a fermion spinor, respectively. A spinor can hence be split and written as $\psi = \psi_R + \psi_L$, where $\psi_{R/L} = P_{\pm}\psi$. Chiral symmetry is the invariance of the Lagrangian of a theory under independent rotations of these left- and right-handed fields [18, 36–40]. The N_f flavours of the theory can be grouped into chiral multiplets ψ_L and ψ_R , to which transformations $U(N_f)_L$ and $U(N_f)_R$ are applied, respectively. For example $\psi_R \rightarrow \psi'_R = U_R \psi_R$ for some $U_R \in U(N_f)_R$, and similarly for the left-handed field ψ_L . In this sense chiral symmetry is also a flavour symmetry for $N_f > 1$, since the multiple flavours can be grouped and undergo chiral rotations simultaneously.

Within QCD we can introduce q_R and q_L for the three lightest flavours as

$$q_{R/L} = \begin{pmatrix} q_{R/L,u} \\ q_{R/L,d} \\ q_{R/L,s} \end{pmatrix}, \quad (2.31)$$

allowing us to rewrite the fermionic part of the QCD Lagrangian for the three lightest flavours as

$$\mathcal{L}_\chi = i\bar{q}_L \not{D} q_L + i\bar{q}_R \not{D} q_R + \bar{q}_L \mathcal{M} q_R + \bar{q}_R \mathcal{M} q_L, \quad (2.32)$$

where I have introduced the mass matrix $\mathcal{M} = \text{diag}(m_u, m_d, m_s)$. The mass terms in this case explicitly break the aforementioned $U(3)_{R/L}$ symmetry, since they mix left- and right-handed quark fields. However, the masses of the three lightest quark flavours, i.e. the up, down and strange, are smaller than the typical energy scale at which QCD

becomes non-perturbative³, and hence QCD is said to have an approximate chiral symmetry for these three flavours. The strange is an order of magnitude heavier than the up and down and is sometimes excluded from this symmetry on these grounds. The discussion that follows will focus on three-flavour chiral symmetry.

As well as its explicit breaking by non-zero quark masses, chiral symmetry is also broken spontaneously [36,38,39]. In a similar manner to EWSB, the theory exhibits a degenerate ground state that is invariant under chiral rotations. In its initial formulation, therefore, the system respects chiral symmetry. This symmetry is then spontaneously broken by selecting a particular ground state from these degenerate minima. In contrast, explicit symmetry breaking involves introducing terms into the Lagrangian that at no point respect the symmetry being broken. The chiral symmetry group $U(3)_L \times U(3)_R$ can be decomposed into $SU(3)_L \times SU(3)_R \times U(1)_V \times U(1)_A$, with each subgroup possessing a related Ward identity. The $U(1)_V$ symmetry corresponds to baryon (or quark) number conservation, with the conserved current $j^{V\mu} = \bar{q}(x)\gamma^\mu q(x)$. The $U(1)_A$ symmetry is satisfied only at the classical level: after the fields are quantised the associated axial Ward identity (AWI) gains an axial anomaly that is present even in the chiral limit of massless quarks:

$$\partial_\mu j^{A\mu}(x) = 2i\bar{q}(x)\gamma^5 \mathcal{M}q(x) + \frac{3g_s^2}{32\pi^2}\epsilon_{\mu\nu\rho\sigma}F_a^{\mu\nu}F^{\rho\sigma a}, \quad (2.33)$$

where $\epsilon_{\mu\nu\rho\sigma}$ is the completely anti-symmetric Levi-Civita tensor and the convention $\epsilon_{0123} = +1$ is used. The current $j^{A\mu}$ is given by

$$j^{A\mu}(x) = \bar{q}(x)\gamma^\mu\gamma^5 q(x). \quad (2.34)$$

The symmetry $SU(3)_L \times SU(3)_R$ also has associated axial and vector Noether currents

$$j_a^{A\mu}(x) = \bar{q}(x)\gamma^\mu\gamma^5\frac{\lambda_a}{2}q(x) \quad (2.35)$$

$$j_a^{V\mu}(x) = \bar{q}(x)\gamma^\mu\frac{\lambda_a}{2}q(x), \quad (2.36)$$

where λ_a are the Gell-Mann matrices as described in Section 2.2.1. Promoting the global $SU(3)_L \times SU(3)_R$ symmetry to a local one within Equation (2.30) and setting $O = \mathbb{1}$, one can derive the following current divergences:

$$\partial_\mu j_a^{A\mu}(x) = i\bar{q}(x)\left\{\mathcal{M}, \frac{\lambda_a}{2}\right\}\gamma^5 q(x) \quad (2.37)$$

$$\partial_\mu j_a^{V\mu}(x) = i\bar{q}(x)\left[\mathcal{M}, \frac{\lambda_a}{2}\right]q(x). \quad (2.38)$$

³This scale is inherently difficult to quantify, though one may consider $\Lambda_{\text{QCD}} \sim 250 \text{ MeV}$ [5] as one possibility.

In the case of degenerate quark masses, the commutator in Equation (2.38) vanishes and the non-singlet vector current is conserved. The *partially conserved axial current* (PCAC) $j_a^{A\mu}$ is only conserved in the case of perfect chiral symmetry, where $\mathcal{M} = 0$. In the case of degenerate quark masses, however, the divergence of the PCAC becomes proportional to the pseudoscalar density [37]. These non-singlet currents have associated charge operators \hat{Q}_a^A and \hat{Q}_a^V . These operators commute with the Hamiltonian, and it is possible to show that if the former annihilate the vacuum, then there must be degenerate negative parity states associated with those of positive parity. However, this is contradicted by experimental measurements [41, 42]. For example there is no baryon octet of negative parity to partner that with positive parity. The solution to this discrepancy is to assert that the operators \hat{Q}_a^A do not annihilate the vacuum and chiral symmetry is spontaneously broken. Specifically the symmetry group $SU(3)_L \times SU(3)_R$ is broken to $SU(3)_V$. Indeed, the operators \hat{Q}_a^V have been shown to annihilate the vacuum, meaning the vacuum is invariant under $SU(3)_V$. Using Coleman's theorem [43], this implies that we should expect $SU(3)_V$ multiplets to exist in the hadron spectrum. The lowest-lying of these is the octet of pseudoscalar mesons [41]

$$\phi = \begin{pmatrix} \frac{1}{\sqrt{2}}\pi^0 + \frac{1}{\sqrt{6}}\eta & \pi^+ & K^+ \\ \pi^- & -\frac{1}{\sqrt{2}}\pi^0 + \frac{1}{\sqrt{6}}\eta & K^0 \\ K^- & \bar{K}^0 & -\frac{2}{\sqrt{6}}\eta \end{pmatrix}, \quad (2.39)$$

which, given their small masses, are called *pseudo-Goldstone bosons*. In the limit of vanishing quark mass, these correspond to the eight Goldstone bosons predicted by Goldstone's theorem.

2.4.2 Isospin Symmetry

If we restrict the discussion of chiral symmetry to the two lightest quark flavours, then the resulting $SU(2)_L \times SU(2)_R$ chiral symmetry is spontaneously broken to $SU(2)_V$. This symmetry is known as isospin symmetry [18, 39, 44]. We can group the up and down quarks into an $SU(2)$ isospin doublet. This doublet can then have global isospin rotations $U_I = e^{i\omega_k \tau^k}$ effected upon it such that the Lagrangian remains invariant.

At the mathematical level, isospin shares many properties with spin as encountered in basic quantum mechanics [44]: a particle's isospin properties may be characterised by the isospin quantum numbers I and I_3 , corresponding to a particle's total isospin and isospin parallel to the third axis in isospin space. Both the up and down quarks have $I = 1/2$, though the up has $I_3 = +1/2$ and the down $I_3 = -1/2$.

In reality isospin symmetry is only approximate, with the non-zero value of $m_u - m_d$ and the differing charges of the up and down quarks resulting in this symmetry being explicitly broken. The incorporation of isospin symmetry and its breaking into the quark

Particle	I	I_3
π^+	1	+1
π^0	1	0
π^-	1	-1
η	0	0
K^+	1/2	+1/2
K^0	1/2	-1/2
K^-	1/2	-1/2
\bar{K}^0	1/2	+1/2
p	1/2	+1/2
n	1/2	-1/2

Table 2.2: Isospin quantum numbers of selected low-lying hadronic states.

model describe various phenomena observed in the lowest-lying states of the hadron spectrum. A summary of the hadronic isospin quantum numbers most relevant to the present work are given in Table 2.2. From these quantum numbers it is possible to group certain particles together into multiplets [41, 45]: the three pions form an isospin triplet, whilst the K^+ and K^0 , K^- and \bar{K}^0 , and proton and neutron form isospin doublets. Isospin symmetry breaking in this last case can explain why the proton is lighter than the neutron, despite its electric charge: the non-zero value of $m_u - m_d$ has a stronger effect on isospin symmetry breaking than the difference in the electric charges of the u and d quarks. Historically, this was evidence for the down-quark having a larger mass than the up. Similarly, the mass splitting of the charged and neutral pions is described by the breaking of isospin symmetry.

2.4.3 G -parity

G -parity combines charge conjugation with an isospin rotation of π about the second axis of isospin space [46, 47], i.e.:

$$G = C e^{i\pi\tau_2}, \quad (2.40)$$

where C is the charge conjugation matrix⁴ $C = \gamma^0\gamma^2$ and $\tau_2 = \frac{1}{2}\sigma_2$. In the isospin limit of degenerate up- and down-quarks, G -parity is a symmetry of the QCD Lagrangian, since the Lagrangian is invariant under charge conjugation and isospin rotations.

G -parity acts on states as

$$G|\eta_G\rangle = \eta_G|\eta_G\rangle, \quad (2.41)$$

where $\eta_G = \pm 1$ is the G -parity quantum number. In general, $\eta_G = \eta_C(-1)^I$, where η_C is the charge conjugation quantum number and I is the previously mentioned total isospin. Table 2.3 contains total isospin, charge conjugation and G -parity quantum numbers for

⁴This representation of the charge conjugation matrix assumes the gamma matrices are in the chiral representation (see Appendix A).

Particle/State	I	η_C	η_G
π	1	-1	-1
2π	0, 1, 2	1	-1, +1
$\rho(770)$	1	-1	+1
K	1/2	-	-
$2K$	0, 1	1	-1, +1
$\phi(1020)$	0	-1	-1

Table 2.3: Isospin, charge conjugation and G -parity quantum numbers of selected low-lying hadronic states in the limit of isospin symmetry.

selected meson states in the isospin limit. Since the QCD Lagrangian is invariant under charge conjugation and isospin rotations in the isospin limit, it must also be invariant under G -parity in this limit. Indeed, this property of QCD will be useful later in this work, when considering the possible intermediate states that may be produced by the vector current $(\bar{\psi}_s \gamma_\mu \psi_s)(x)$. Specifically, the consideration of how this operator couples to the mesonic states in Table 2.3 will motivate the identification of the lowest-lying eigenstate (see Section 5.6.1), which in turn indicates the degree to which $a_\mu^{(2)\text{had},s}$ is affected by finite volume effects (see Section 5.6.6).

Chapter 3

The Muon Anomalous Magnetic Moment

In this chapter I introduce the main subject of this work, namely the muon anomalous magnetic moment, a_μ . I accompany this with a discussion of the hadronic vacuum polarisation (HVP), which is required to compute the leading order hadronic contribution to a_μ . I begin by motivating the anomalous magnetic moment through the study of the QED vertex function in Section 3.1. I then discuss the phenomenology and current experimental status of a_μ in Section 3.2. In this section I necessarily treat various topics relating to the HVP in a superficial manner, expanding upon them later in Section 3.3. Finally, in Section 3.4 I describe how the HVP is combined with results from perturbation theory to produce a formula for calculating the anomalous magnetic moment in Euclidean space.

3.1 The QED Vertex Function

I will now motivate the anomalous magnetic moment by considering the QED vertex function. A particle's magnetic dipole $\boldsymbol{\mu}$ describes its interaction with a magnetic field \mathbf{B} via the potential energy [6, 40, 48]

$$V = -\boldsymbol{\mu} \cdot \mathbf{B}, \tag{3.1}$$

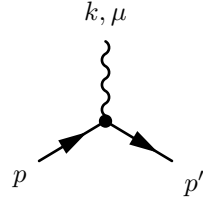
such that it is energetically favourable for a particle's magnetic dipole to align with the magnetic field. The magnetic dipole of a charged fermion can be related to its spin \mathbf{S} as

$$\boldsymbol{\mu} = g \frac{Q}{2m} \mathbf{S}, \tag{3.2}$$

where g , Q and m are the Landé g -factor, electric charge and mass of the fermion in question, respectively. Before the electromagnetic field is quantised, the Dirac equation [49]

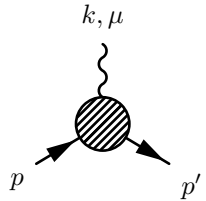
predicts $g = 2$ for charged leptons. However, loop corrections to the lepton-photon vertex result in this quantity being fractionally larger than 2. This work is concerned with computing the leading order (LO) hadronic corrections to g_μ , meaning the g -factor for the muon. In this section I will provide a brief overview of the QFT associated with g_μ .

In tree-level QED, the lepton-photon vertex is given by [6, 40, 50–52]



$$= -ie\gamma^\mu \quad (k = p' - p).$$

Beyond tree-level, the Dirac gamma matrix is replaced with the vertex function $\Gamma^\mu(p, p')$ [53, 54]:



$$= -ie\Gamma^\mu(p, p') \quad (k = p' - p).$$

The form of $\Gamma^\mu(p, p')$ can be constrained using Lorentz invariance and the Ward–Takahashi identity $k_\mu \Gamma^\mu = 0$ [55, 56]¹. Lorentz invariance dictates that the vertex function should transform as a four-vector, meaning it should have the form

$$\Gamma^\mu(p, p') = \gamma^\mu \cdot A + (p'^\mu + p^\mu) \cdot B + (p'^\mu - p^\mu) \cdot C, \quad (3.3)$$

where A , B and C are to be determined. The Dirac equation can be used to eliminate any terms containing \not{p} or \not{p}' such that A , B and C can only be functions of the fermion mass m and k^2 . The Ward identity then requires that $C = 0$, and the Gordon decomposition identity,

$$\bar{u}(p')\gamma^\mu u(p) = \bar{u}(p') \left[\frac{p^\mu + (p')^\mu}{2m} + \frac{i\sigma^{\mu\nu}(p'_\nu - p_\nu)}{2m} \right] u(p), \quad (3.4)$$

where $\sigma^{\mu\nu} = \frac{i}{2}[\gamma^\mu, \gamma^\nu]$, can then be used to write $\Gamma^\mu(p, p')$ as

$$\Gamma^\mu(p, p') = \gamma^\mu F_1(k^2) + \frac{i\sigma^{\mu\nu}k_\nu}{2m} F_2(k^2), \quad (3.5)$$

where F_1 and F_2 are form factors dependent on k^2 .

To understand the meaning of F_1 , we can consider the conventional vertex renormalisation condition for QED. This posits that for $k^2 = 0$, the vertex Feynman rule should

¹This requires that the fermions be on-shell, which we can assume is true in the case of the muon anomalous magnetic moment, since experimental measurements use on-shell muons.

equal that of the tree-level theory, i.e. $-ie\Gamma^\mu(p, p' = p) = -ie\gamma^\mu$. At $k = 0$, Equation (3.5) reduces to $\Gamma^\mu(p, p' = p) = \gamma^\mu F_1(0)$. To satisfy the renormalisation condition we therefore require $F_1(0) = 1$ at all orders of perturbation theory.

The physical significance of F_2 can be understood by considering a nonrelativistic electron being scattered by a static vector potential. The amplitude for this process takes the form

$$i\mathcal{M} = ie\bar{u}(p') \left(\gamma^i F_1(k^2) + \frac{i\sigma^{i\nu} k_\nu}{2m} F_2(k^2) \right) u(p) \tilde{A}^i(\mathbf{k}), \quad (3.6)$$

where $\tilde{A}^i(\mathbf{k})$ is a classical vector potential. To take the nonrelativistic limit, we must use the nonrelativistic expansion of the spinors, keeping the first order momenta terms:

$$u(p) \approx \sqrt{m} \begin{pmatrix} (1 - \mathbf{p} \cdot \boldsymbol{\sigma}/2m)\xi \\ (1 + \mathbf{p} \cdot \boldsymbol{\sigma}/2m)\xi \end{pmatrix}. \quad (3.7)$$

Applying this approximation to the product $\bar{u}(p')\gamma^i u(p)$ and discarding terms independent of spin gives

$$\bar{u}(p')\gamma^i u(p) = 2m\xi^\dagger \left(\frac{-i}{2m} \epsilon^{ijk} k^j \sigma^k \right) \xi, \quad (3.8)$$

where the Levi-Civita tensor arises from use of the identity $\sigma^i \sigma^j = \delta^{ij} + i\epsilon^{ijk} \sigma^k$. The F_2 term in Equation (3.5) has the nonrelativistic limit

$$\bar{u}(p') \left(\frac{i}{2m} \sigma^{i\nu} k_\nu \right) u(p) = 2m\xi^\dagger \left(\frac{-i}{2m} \epsilon^{ijk} k^j \sigma^k \right) \xi. \quad (3.9)$$

The original matrix element hence has the following form in the nonrelativistic limit:

$$i\mathcal{M} = -i(2m) \cdot e\xi^\dagger \left(-\frac{1}{2m} \boldsymbol{\sigma} [F_1(0) + F_2(0)] \right) \xi \cdot \tilde{\mathbf{B}}(\mathbf{k}), \quad (3.10)$$

where the magnetic field $\tilde{\mathbf{B}}$ is related to the vector potential as $\tilde{B}^k(\mathbf{k}) = -i\epsilon^{ijk} k^i \tilde{A}^j(\mathbf{k})$. Again, interpreting this as the Born approximation to an electron scattering off a magnetic potential, we can compare it to the potential $V(\mathbf{x}) = -\langle \boldsymbol{\mu} \rangle \cdot \mathbf{B}(\mathbf{x})$ and find that

$$\langle \boldsymbol{\mu} \rangle = \frac{e}{m} [F_1(0) + F_2(0)] \xi^\dagger \frac{\boldsymbol{\sigma}}{2} \xi. \quad (3.11)$$

Equating this result to Equation (3.2) and using the previous result $F_1(0) = 1$ gives $g = 2 + 2F_2(0)$.

At LO in QED, $F_2(0) = 0$, which implies $g = 2 + \mathcal{O}(\alpha)$. The additional contributions arise from the aforementioned loop corrections, known collectively as the anomalous magnetic moment, $a = (g - 2)/2$.

Contribution	$a_\mu \times 10^{10}$	$\delta a_\mu \times 10^{10}$
QED (5-loop)	11658471.895	0.008
Electroweak (2-loop)	15.5	0.1
LO hadronic (HVP) [57]	692.3	4.2
LO hadronic (HVP) [58]	694.9	4.3
NLO hadronic	-9.84	0.06
NNLO hadronic	1.24	0.01
HLbL	10.5	2.6
Total [57]	11659181.5	4.9
Total [58]	11659184.1	5.0
Experimental	11659209.1	6.3

Table 3.1: Contributions to the theoretical value of a_μ compared to the experimental result, along with uncertainties δa_μ [5].

3.2 Standard Model Contributions

The vertex function Γ^μ receives contributions from all sectors of the SM. Here I summarise the current status of these calculations. The associated values for a_μ are given in Table 3.1. The current experimental value is known to approximately 540ppb [5], and there has been a tension between the theoretical and experimental determinations of this quantity for some time [5]. The current discrepancy between these determinations stands at 3.6σ [5]. A reduction in the errors on both of these determinations is therefore essential to determining whether the current tension is indicative of physics beyond the SM (BSM). The new $g - 2$ experiments at Fermilab $g - 2$ (E989 collaboration) [7] and J-PARC (J-PARC $g - 2$ /EDM collaboration) [8] are expected to be able to measure a_μ with accuracies of 140ppb and ~ 100 ppb, respectively. This puts pressure on the theory community to increase the level of precision in the theoretical determination.

3.2.1 Electroweak Theory

The NLO contribution to Γ^μ in QED, the Schwinger term, is computed from the Feynman diagram in panel (a) of Figure 3.1. This contribution is equal to $\alpha/2\pi$, where the fine structure constant $\alpha = e^2/4\pi$. Historically this was the first loop correction to g to be computed and is the dominant term in the perturbative expansion [54]. Currently the loop corrections to g from QED are known to five loops [59]. To be clear, the value specified in Table 3.1 is not the result of computing all possible QED Feynman diagrams up to and including those with five loops. The diagrams can be split into universal diagrams, which do not contain any internal lepton loops, and mass-dependent diagrams, which do contain such loops. The five-loop QED result contains the direct computation of all universal diagrams up to and including four loops. The universal five-loop diagrams are, however, still largely unknown, and their effect is included in the total universal five-loop computation through the use of an estimated upper bound.

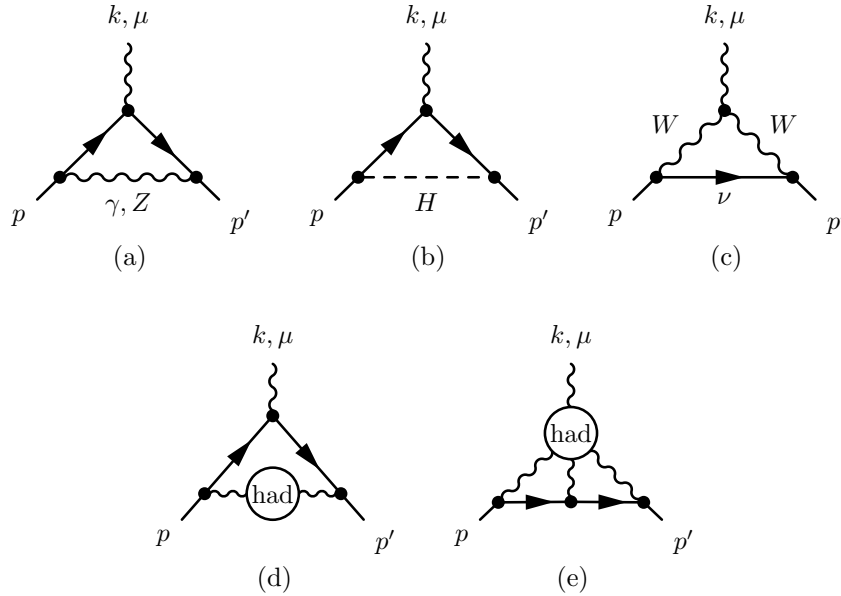


Figure 3.1: Feynman diagrams for some of the contributions to the muon anomalous magnetic moment. The one-loop QED contribution, or Schwinger term, is given in panel (a) (where the loop boson is a photon). The one-loop contributions from the weak interaction are given in panels (a), (b) and (c) (where the loop boson in (a) is the Z). Panels (d) and (e) contain the diagrams for the LO hadronic contribution, the subject of this work, and the HLbL contribution, respectively.

The mass-dependent contributions to a_μ first appear necessarily at two loops via photon vacuum polarisation effects. Since there are three lepton generations in the SM, the total number of mass-dependent diagrams up to and including five loops is formidable. The work can be simplified through phase space considerations: the contribution of a diagram containing four τ loops, for example, will be significantly smaller than the same diagram with a different combination of lepton generations. The numerous diagrams can therefore be prioritised depending on the extent to which they are enhanced [6].

Combining the five-loop QED result with the two-loop electroweak calculation, which I discuss further below, one obtains a value of $g_e - 2$ for the electron that agrees with experimental measurements to ten significant figures [60, 61], making this one of the most accurately verified quantities in physics. The five-loop QED calculation alone accounts for nine of these significant figures, indicating the extent to which this quantity is dominated by QED. Besides the considerable intellectual efforts applied to its computation and measurement, the level of agreement between the theoretical determination of $g_e - 2$ and the experimental measurement is also a result of the physics relating to the interaction. To understand this, we can consider the role of a_ℓ in the mediation of helicity flipping transitions. Helicity is a conserved quantity in interactions between massless particles. This is not the case in interactions between massive particles, where the amplitude of a transition is proportional to the mass of the particle. The probability of a transition is the modulus square of the amplitude, which suggests that the shift

in the anomalous magnetic moment of a lepton ℓ arising from quantum fluctuations of heavier degrees of freedom is given by [6, 62]

$$\delta a_\ell \propto \frac{m_\ell^2}{M^2}, \quad (3.12)$$

where m_ℓ is the mass of the lepton and M is a large mass scale, such as the mass of a heavy SM or BSM particle or an ultraviolet (UV) cut-off beyond which the SM fails as a theory. The electron is considerably lighter than the muon, so from Equation (3.12) one can conclude that a_e is dominated by contributions from QED and, to a lesser extent, the weak interaction. At the current level of precision, therefore, the effects of heavier degrees of freedom are not significant enough to affect the theoretical determination of a_e . The muon, on the other hand, is roughly 200 times heavier than the electron, and so the deviation in a_μ resulting from heavier states will be much greater. One may question why a_τ is not studied more extensively, given the τ is approximately 17 times heavier than the muon. Unfortunately the mean lifetime of the τ is shorter than the typical timescales over which the strong interaction takes place, making this a difficult quantity to study experimentally [5].

There are similar contributions to a_μ from the weak interaction. Panels (a), (b) and (c) of Figure 3.1 illustrate the three one-loop processes that must be computed to obtain the LO weak contribution to a_μ (the first of these containing a Z boson in the loop rather than a photon). The Higgs exchange diagram in panel (b) contributes significantly less to the total value of a_μ than the diagrams in panels (a) and (c). Specifically, given a lower bound on the Higgs mass of 114 GeV, the contribution from this diagram is at most 5×10^{-14} , five orders of magnitude smaller than the other two diagrams. The electroweak contribution to a_μ has been computed up to two loops [5].

3.2.2 QCD

From Table 3.1, it is clear that the source of most of the uncertainty in the total value of a_μ comes from hadronic effects, specifically the LO hadronic (HVP) and hadronic light-by-light (HLbL). I will now discuss each of these contributions in turn.

The LO hadronic contribution, which I denote $a_\mu^{(2)\text{had}}$, is both the largest of the hadronic contributions and also that with the greatest uncertainty, with the Feynman diagram in panel (d) of Figure 3.1. The blob in this diagram is the hadronic vacuum polarisation (HVP),



which describes the hadronic contribution to the photon self-energy. The HVP tensor $\Pi_{\mu\nu}$ is computed as

$$i\Pi^{\mu\nu}(q) = \int d^4x e^{iq\cdot x} \langle 0 | j^\mu(x) j^\nu(0) | 0 \rangle, \quad (3.13)$$

where the vector current $j^\mu(x)$ is given by

$$j^\mu(x) = \sum_f Q_f \bar{\psi}_f(x) \gamma^\mu \psi_f(x), \quad (3.14)$$

and Q_f , ψ_f and $\bar{\psi}_f$ are the electric charge, quark and antiquark fields of quark flavour f , respectively. The HVP is therefore an essential ingredient in the computation of $a_\mu^{(2)\text{had}}$. The Feynman diagram in panel (d) of Figure 3.1 implies the presence of a loop integral over all q , which must be evaluated to determine $a_\mu^{(2)\text{had}}$. Unfortunately, evaluating the HVP analytically at small q^2 is not possible due to the non-perturbative nature of low-energy QCD [21, 22].

In the absence of a method for determining $a_\mu^{(2)\text{had}}$ purely from first principles, computations have been performed using analytical results from QFT and experimental measurements [57, 63]. I will now briefly discuss the analytical ingredients in this method, expanding upon them later in Section 3.3. The Ward identity (see Section 3.3.2) allows the HVP tensor to be decomposed as $\Pi^{\mu\nu}(q) = (q^2 g^{\mu\nu} - q^\mu q^\nu) \Pi(q^2)$, where $\Pi(q^2)$ is the dimensionless HVP form factor. The HVP form factor can be expressed using a dispersion relation. However, the vacuum polarisation in general contains a logarithmic UV divergence (see Section 3.3.3) that must be renormalised using a subtraction scheme such as $\overline{\text{MS}}$. The HVP form factor is therefore expressed using the once-subtracted dispersion relation:

$$\Pi(q^2) - \Pi(0) = q^2 \int_{4m_\pi^2}^{\infty} \frac{\rho(s)}{s(s - q^2 - i\epsilon)}, \quad (3.15)$$

where the vector spectral density $\rho(s) = \text{Im}\Pi(s)/\pi$. This spectral density can be related to the hadronic vector two-point function via the Källén–Lehmann spectral decomposition [64, 65] (see Section 3.3.1). As was shown in [66], this allows $a_\mu^{(2)\text{had}}$ to be expressed as

$$a_\mu^{(2)\text{had}} = \frac{\alpha}{\pi} \int_0^\infty ds \frac{f(s)}{s} \rho(s) \equiv \frac{\alpha}{\pi^2} \int_0^\infty ds \frac{f(s)}{s} \text{Im}\Pi(s), \quad (3.16)$$

where the QED kernel f in Minkowski space is given by

$$f(s) = x^2 \left(1 - \frac{x^2}{2}\right) + (1+x)^2 \left(1 + \frac{1}{x^2}\right) \left(\log(1+x) - x + \frac{x^2}{2}\right) + \frac{1+x}{1-x} x^2 \log x, \quad (3.17)$$

where $x = (1 - \beta_\mu)/(1 + \beta_\mu)$ and $\beta_\mu = (1 - 4m_\mu^2/s)^{1/2}$. The optical theorem [67–70] (see Section 3.3.1) can then be used to relate the forward scattering amplitude to the total cross-section. This allows the HVP form factor to be related to the total cross-section

of an electron-positron collision:

$$\text{Im } \Pi(s) = \frac{s}{4\pi\alpha(s)} \sigma_{\text{tot}}(e^+e^- \rightarrow \text{hadrons}) \equiv \frac{\alpha(s)}{3} R(s), \quad R(s) = \sigma_{\text{tot}} \bigg/ \frac{4\pi\alpha^2(s)}{3s}, \quad (3.18)$$

where α is the QED running coupling and σ_{tot} is the total cross section. The normalisation factor $4\pi\alpha^2(s)/3s$ is the tree-level cross section for the process $e^+e^- \rightarrow \mu^+\mu^-$ in the limit $s \gg 4m_\mu^2$. Combining these results gives

$$a_\mu^{(2)\text{had}} = \frac{\alpha^2}{3\pi^2} \int_{4m_\pi^2}^{\infty} ds \frac{f(s)}{s} R(s). \quad (3.19)$$

The most recent determinations of $a_\mu^{(2)\text{had}}$ using this method use data from the BaBar and KLOE experiments [57, 58] and differ in how the experimental data is treated before being used in this computation. More specifically, the measurements from each experiment contain cross-sections for a variety of hadronic final-state channels. There is the possibility of correlations existing both between different channels and different experiments. In [57] the authors try to account for these correlations in their analysis, whilst in [58] the authors state that they see no well-defined way to incorporate them.

The primary drawback of the current determination of $a_\mu^{(2)\text{had}}$ is that the computation is not *ab initio*: in principal the experimental data used in this computation will already contain the effects of all physical degrees of freedom, including any resulting from BSM physics. In practice this would imply the presence of a BSM particle with a relatively small mass. Since no such particle has been detected experimentally [5], this would suggest that the current determination is not adversely affected by BSM physics. However, evaluating the integral in Equation (3.19) is not a simple process, requiring various procedures to treat the experimental data appropriately. I have already mentioned the difficulty in combining data from various channels and experiments such that correlations between them are accounted for. In addition, a chief concern is the subtraction of radiation in the initial and final states, which does not contribute to the HVP. Initial state radiation can be accounted for analytically using QED. Final state radiation presents more of a challenge, though it is typically subtracted using a generalised form of scalar QED where one exchanges the point pion form-factor with that determined from experiment [6]. This necessarily introduces some model-dependence into the analysis. In addition to this, the cross-section data is sparse over some regions of the integral. In these cases it is necessary to parametrise the cross-section data to avoid any bias when computing $a_\mu^{(2)\text{had}}$ using a numerical integration method such as the trapezium rule. Figure 3.2 illustrates cross-section data for both the ω (left) and ϕ (right) resonances [71]. It is clear that applying the trapezium rule in these cases leads to an overestimation of the value of the integral. In both cases the data is fitted with a parametrisation to account for the low number of experimental data points. The parametrisation in this particular case consists of a Breit–Wigner distribution summed with either one (in the

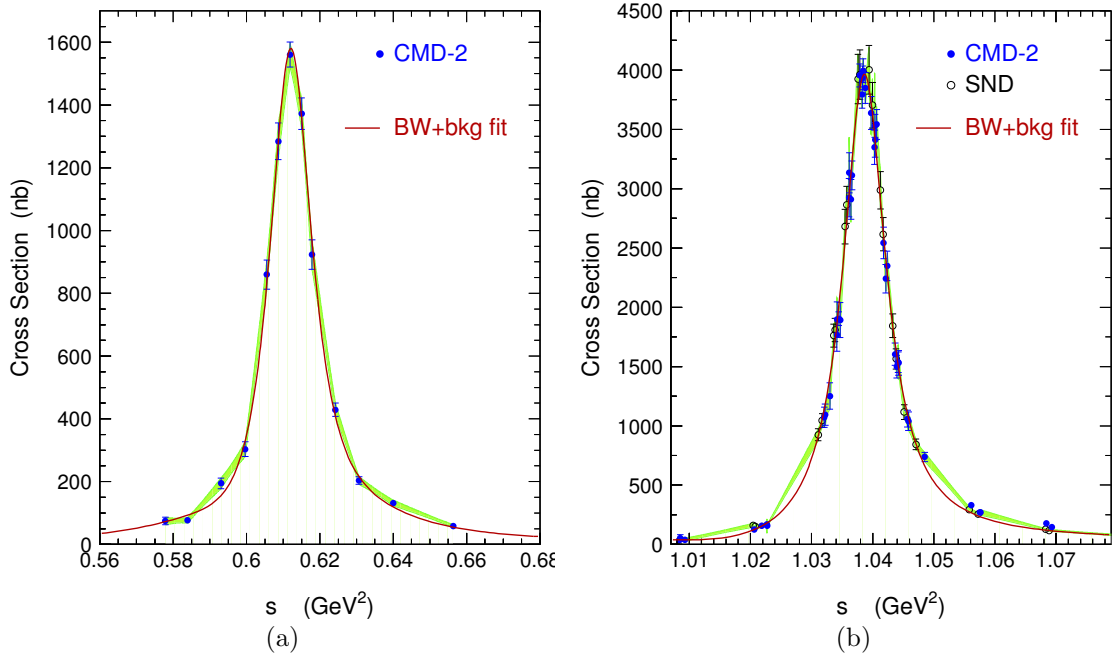


Figure 3.2: Cross section data from e^+e^- collisions illustrating the ω resonance (panel (a)) and the ϕ resonance (panel (b)). The shaded green band indicates the result applying the trapezoidal rule within correlated errors. In both cases the number of experimental data points is not sufficient to perform a trapezoidal integration without introducing a bias. Taken from [71].

case of the ω) or two (in the case of the ϕ) Gaussian curves. Selecting a particular parametrisation in this way has the potential to introduce a systematic uncertainty into the determination of $a_\mu^{(2)\text{had}}$. In summary there are various steps in the calculation of the current determination where one must select a particular analysis strategy or model that will introduce systematic effects that are difficult to quantify. This is cause to treat the current tension with a level of scepticism. A first principles calculation of $a_\mu^{(2)\text{had}}$ is therefore highly desirable. If such a method were capable of matching the value and precision of the current theoretical determination then this would promote confidence in the present method.

Table 3.2 summarises the lattice computations of the value of $a_\mu^{(2)\text{had}}$ to date. Omitted from the table are calculations of various individual contributions to $a_\mu^{(2)\text{had}}$. Specifically the quark-disconnected contribution, the definition of which I give in the next section, was computed as $-9.6(3.3)(2.3) \times 10^{-10}$ in [79] and estimated as $-0.14(5)\%$ of the light quark-connected contribution in [80]. The systematic error arising from neglecting the disconnected contribution altogether was also estimated as being of the order of 4–5% in [81]. The quark-connected strange and charm contributions to $a_\mu^{(2)\text{had}}$ were determined as $53.4(6) \times 10^{-10}$ and $14.4(4) \times 10^{-10}$, respectively, in [82].

From Table 3.2 and the various values I state in the preceding text it is clear how much interest there is within the lattice community in calculating $a_\mu^{(2)\text{had}}$. Indeed, one may

Author/Collaboration	Year	$a_\mu^{(2)\text{had}} \times 10^{10}$
T. Blum	2003	318(69), 378(96), 460(78) [72]
C. Aubin and T. Blum	2007	713(15), 748(21) [73]
ETMC	2011	572(16) [74]
Della Morte et al.	2012	618(64) [75]
UKQCD	2012	641(33)(32) [76]
ETMC	2014	674(21)(18) [77]
HPQCD	2016	666(6)(12) [78]

Table 3.2: A summary of lattice determinations of $a_\mu^{(2)\text{had}}$ to date. Where two errors are quoted, the first is statistical and the second is systematic. The study of [72] states three values of $a_\mu^{(2)\text{had}}$, each computed using a different lattice volume and spacing. The study of [73] states two values of $a_\mu^{(2)\text{had}}$, with the difference lying in the ansatz used to extrapolate to the physical light quark mass.

conclude from the table that more recent results satisfy the requirements of an *ab initio* computation of $a_\mu^{(2)\text{had}}$ with acceptable errors. However, what is not clear from the table is the nature of these various computations. In the first instance, none of the results I quote include isospin breaking effects, which are expected to contribute $\sim 1\%$ to the total value of $a_\mu^{(2)\text{had}}$. There are additional subtleties in the calculations of the quoted results. The study in [74], for example, neglects the effect of virtual strange quark loops in the QCD vacuum, and [76] uses an effective theory to model the HVP at small values of q^2 . In addition, all of the entries in Table 3.2 employ non-physical light quark masses, requiring an extrapolation to reach the physical pion mass. In the calculation performed by HPQCD in [78], this is more correctly an interpolation, since some lattice calculations were performed using pion masses lighter than the physical value. However, the methods used in [78] cannot be considered *ab initio*, as again effective field theories were employed in the analysis in order to account for various lattice artefacts. In summary there is still much progress to be made in understanding the systematic effects of various lattice simulation and analysis methods when computing $a_\mu^{(2)\text{had}}$.

As stated in Table 3.1, there are various additional hadronic contributions beyond LO. The most notable of these is the hadronic light-by-light (HLbL) contribution, which has the greatest uncertainty after the LO hadronic contribution. The associated Feynman diagram is given in panel (e) of Figure 3.1. There is currently no known method for computing this contribution from experimental data, though there has been some progress towards a method to achieve this [83–87]. The value I quote here is computed using an effective field theory approach incorporating both a $1/N_c$ expansion and chiral perturbation theory. This is a necessarily complex task, not least because the diagram in Figure 3.1 is accompanied by all possible permutations of the photon legs. Again, a first-principles computation of this contribution could instil confidence in the current determination. Indeed, there are currently efforts underway to calculate this contribution using lattice QCD [88–90]. Of particular note is the method developed in [88] and

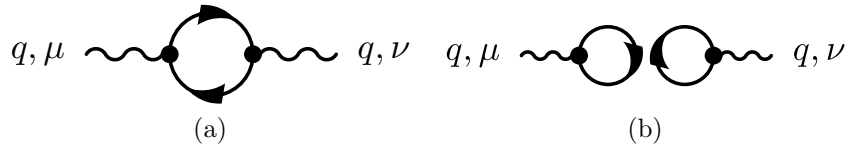


Figure 3.3: The two types of possible within the HVP. Panel (a) shows the quark-connected contribution, whilst panel (b) shows the quark-disconnected contribution. For clarity and simplicity I have omitted gluons and additional quark loops from these diagrams, which in panel (b) connect the two quark loops.

used in [89], where both QED and the muon are included in the lattice simulation.

3.3 The Hadronic Vacuum Polarisation

From Section 3.2.2 it is evident that the HVP is an essential ingredient in the computation of $a_\mu^{(2)\text{had}}$. In the same section I discussed various properties of the HVP in a superficial manner. Here I discuss them in more detail.

First I will discuss the various contributions to the HVP. The electromagnetic current $j^\mu(x)$ in Equation (3.14) contains contributions from all six quark flavours. From Wick's theorem [91], the HVP therefore receives a quark-connected contributions such as

$$\langle 0 | \overline{\psi}_i(x) \gamma^\mu \psi_i(x) \overline{\psi}_i(0) \gamma^\nu \psi_i(0) | 0 \rangle, \quad (3.20)$$

from each quark flavour i , as well as quark-disconnected contributions such as

$$\langle 0 | \overline{\psi}_i(x) \gamma^\mu \psi_i(x) \overline{\psi}_j(0) \gamma^\nu \psi_j(0) | 0 \rangle, \quad (3.21)$$

from quark flavours i and j . This latter set of contributions are not truly disconnected since the two quark loops are connected via gluons. I illustrate these two types of contributions pictorially in Figure 3.3, where I have omitted virtual gluons and additional quark loops for clarity.

It is well known that the quark-disconnected contribution to the HVP will vanish in the limit of $SU(3)$ flavour symmetry amongst the up, down and strange quark flavours, since $\sum_{i,j=u,d,s} Q_i Q_j = 0$ [72]. As a result it has been neglected from past calculations of $a_\mu^{(2)\text{had}}$ where this symmetry is approximately maintained [76, 82]. A calculation using $SU(2)$ NLO chiral perturbation theory indicates that the ratio of the disconnected to connected contributions is equal to $-1/10$ [92], which suggests the dominant contribution to $a_\mu^{(2)\text{had}}$ comes from the quark-connected Wick contractions. Recent work by the RBC/UKQCD collaboration suggests that at physical quark masses the disconnected contributions are small at $\sim 1\%$ of the total value of $a_\mu^{(2)\text{had}}$ [79].

3.3.1 Spectral Representation

Equation (3.16) originates from the Källén–Lehmann spectral representation of the HVP, which arises from considering the possible intermediate vector states that may be generated from the QCD vacuum. I will first discuss this representation in the context of a generic vacuum polarisation before describing where and how the HVP deviates from this more generic case. Starting from the definition of the vacuum polarisation tensor in Equation (3.13), one can derive the Källén–Lehmann spectral representation [64, 65] for the HVP by using the completeness relation for vector states (for a more complete and pedagogical derivation, see Appendix C):

$$\mathbf{1} = |\Omega\rangle\langle\Omega| + \sum_{\lambda} \int \frac{d^3\mathbf{p}}{(2\pi)^3} \frac{1}{2E_{\mathbf{p}}(\lambda)} |\lambda_{\mathbf{p}}^s\rangle\langle\lambda_{\mathbf{p}}^s|, \quad (3.22)$$

where $|\Omega\rangle$ is the vector ground state and $|\lambda_{\mathbf{p}}^s\rangle$ is an eigenstate of energy and spin. This process expands the two-point function into a spectrum of vector propagators:

$$\Pi_{\mu\nu}(q) = \int_0^{\infty} \frac{d\mu^2}{2\pi} \rho(\mu^2) \frac{-i}{q^2 - \mu^2 + i\epsilon} \left(g_{\mu\nu} - \frac{q_{\mu}q_{\nu}}{q^2} \right), \quad (3.23)$$

where the spectral density is given by [66]

$$\rho(\mu^2) = \frac{1}{3} \sum_{\lambda} (2\pi) \delta(\mu^2 - m_{\lambda}^2) \langle\Omega|j^{\mu}(0)|\lambda_{\mathbf{0}}^s\rangle\langle\lambda_{\mathbf{0}}^s|j_{\mu}(0)|\Omega\rangle. \quad (3.24)$$

This spectral function describes the distribution of states according to the mass parameter μ . Figure 3.4 shows a typical spectral density for an interacting theory, with the one-particle state producing the lowest-lying peak in the spectrum. Further bound states with larger masses produce additional peaks at larger values of μ^2 , followed by a continuous spectrum of free two-particle states that produce a branch cut in the spectrum for $\mu^2 \geq (2m)^2$.

The one-particle state can be extracted from Equation (3.23), allowing us to write

$$\begin{aligned} \Pi_{\mu\nu}(q) = & \frac{-iZ_3}{q^2 - m^2 + i\epsilon} \left(g_{\mu\nu} - \frac{q_{\mu}q_{\nu}}{q^2} \right) \\ & + \int_{4m^2}^{\infty} \frac{d\mu^2}{2\pi} \rho(\mu^2) \frac{-i}{q^2 - \mu^2 + i\epsilon} \left(g_{\mu\nu} - \frac{q_{\mu}q_{\nu}}{q^2} \right), \end{aligned} \quad (3.25)$$

where the field strength renormalisation factor $Z_3 = \langle\Omega|j^{\mu}(0)|1_{\mathbf{0}}^s\rangle\langle 1_{\mathbf{0}}^s|j_{\mu}(0)|\Omega\rangle$ is the probability of the current $j_{\mu}(0)$ creating the one-particle state from the vacuum. In a theory without interactions this would be a certainty such that $Z_3 = 1$.

The HVP two-point function contains vector meson intermediate states. Experimental evidence indicates that a one-particle pole in the spectrum does not exist [5]. Instead, the lightest hadronic vector state is given by two free pions. As such there are no poles in the

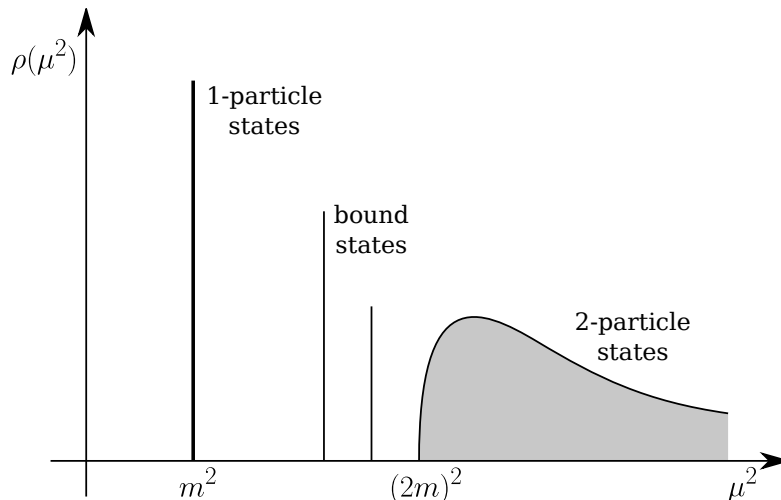


Figure 3.4: An example spectral density function $\rho(\mu^2)$ for an interacting theory.

vector spectral function, with the branch cut starting at $4m_\pi^2$. Instead, one considers the resonances of the spectrum. For example, the three lightest single-particle resonances are the ρ , the ω and the ϕ with masses of 775.26(25) MeV, 782.65(12) MeV and 1019.461(19) MeV, respectively [5]. However, the spectrum is also populated by various other multi-particle states that satisfy the same quantum numbers, such as K^+K^- .

The branch cut in the vacuum polarisation arises from the nonzero imaginary component of this quantity [93]. Indeed, the imaginary component of the form factor $\Pi(q^2)$ can be used to completely define the entire function in the complex plane through analytical continuation, which produces the dispersion relation of Equation (3.15).

To understand this we must consider the role of the branch cut in $\Pi(q^2)$. We start with Cauchy's integral formula, which allows us to write

$$\Pi(q^2) = \frac{1}{2\pi i} \oint_{\mathcal{C}} ds \frac{\Pi(s)}{s - q^2}, \quad (3.26)$$

where the contour \mathcal{C} is given in Figure 3.5. Ultimately we wish to take the limit $R \rightarrow \infty$ such that the integral over the circle of radius R vanishes, leaving an integral along the real axis starting at $4m^2$. However, this requires that $\lim_{|s| \rightarrow \infty} \Pi(s) \rightarrow 0$, and the form factor $\Pi(q^2)$ is UV divergent so does not satisfy this condition (see Section 3.3.3). Instead we must use the infrared subtracted form factor, which is UV convergent. From Cauchy's integral formula one can derive

$$\Pi(q^2) - \Pi(0) = \frac{q^2}{2\pi i} \oint_{\mathcal{C}} ds \frac{\Pi(s)}{s(s - q^2)}. \quad (3.27)$$

Below the branch cut there is insufficient energy to allow multi-particle states to go on-shell, meaning the vacuum polarisation must be real such that $\Pi(s) = \Pi^*(s^*)$ for $s < 4m^2$. This implies that $\text{Im}\Pi(s + i\epsilon) = -\text{Im}\Pi(s - i\epsilon)$. We can analytically continue Π to the entire complex plane and use the behaviour of the imaginary part to determine

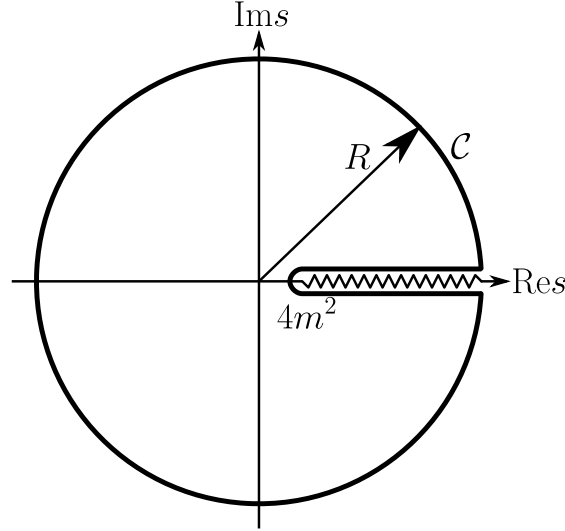


Figure 3.5: The contour used in Equation (3.26).

the discontinuity across the branch cut as

$$\lim_{\delta \rightarrow 0} (\Pi(s + i\delta) - \Pi(s - i\delta)) = 2i\text{Im}\Pi(s), \quad s \in \mathbb{R}, s > 4m^2. \quad (3.28)$$

This relationship can then be used within the integral of Equation (3.27). Taking the limits $R \rightarrow \infty$ and $\delta \rightarrow 0$ gives

$$\Pi(q^2) - \Pi(0) = \frac{q^2}{\pi} \int_{4m^2}^{\infty} ds \frac{\text{Im}\Pi(s)}{s(s - q^2 - i\epsilon)} \equiv q^2 \int_{4m^2}^{\infty} ds \frac{\rho(s)}{s(s - q^2 - i\epsilon)}, \quad (3.29)$$

which is the dispersion relation in Equation (3.15). This result can be combined with the optical theorem to express the vacuum polarisation form factor as a function of the total cross-section $\sigma_{\text{tot}}(e^+e^- \rightarrow \text{anything})$. Specifically the optical theorem in QFT is given by [70]

$$-i(\mathcal{M}_{a \rightarrow b} - \mathcal{M}_{b \rightarrow a}^*) = \sum_f \int d\Pi_f \mathcal{M}_{b \rightarrow f}^* \mathcal{M}_{a \rightarrow f}, \quad (3.30)$$

where $\mathcal{M}_{a \rightarrow b}$ indicates the amplitude of a process with initial and final states a and b . The sum over f indicates a sum over all possible final states f of the process. In the case of forward scattering, where the initial and final states both contain two particles p_1 and p_2 such that $a = b = p_1 p_2$, this equation becomes

$$\text{Im} \mathcal{M}_{p_1 p_2 \rightarrow p_1 p_2} = 2E_{\text{cm}} p_{\text{cm}} \sigma_{\text{tot}}(p_1 p_2 \rightarrow \text{anything}), \quad (3.31)$$

where E_{cm} is the total centre-of-mass energy and p_{cm} is the magnitude of the momentum of either particle in the centre-of-mass frame. In the context of the HVP we can identify the form factor $\Pi(s)$ with the matrix element $\mathcal{M}_{p_1 p_2 \rightarrow p_1 p_2}$. The right-hand side of the optical theorem must then contain the total cross section for the process $e^+e^- \rightarrow \text{hadrons}$, which may be obtained through experimental measurements at e^+e^- colliders.

3.3.2 Vector Ward Identity

In Section 3.2.2 I specified the tensor decomposition of the HVP and named the Ward identity [55, 56] as one of the ingredients in deriving this decomposition. This identity arises via gauge invariance when applying a local $U(1)$ transformation to the fermion fields in the QED Lagrangian, i.e.

$$\psi(x) \rightarrow \psi'(x) = e^{iQ\alpha(x)}\psi(x), \quad (3.32)$$

where Q is the generator of the $U(1)$ transformation, equal to the charge of the fermion in question, and α is a spacetime-dependent parameter. Recalling the general formula for deriving a Ward identity given some action S and operator O

$$\left\langle O \frac{\delta S}{\delta \alpha(x)} \right\rangle = i \left\langle \frac{\delta O}{\delta \alpha(x)} \right\rangle, \quad (2.30)$$

we can now determine the Ward identity associated with the transformation in Equation (3.32), obtaining²

$$\partial_\mu \langle j^\mu(x) O \rangle = i \left\langle \frac{\delta O}{\delta \alpha(x)} \right\rangle, \quad (3.33)$$

where the conserved vector current $j^\mu(x) = \bar{\psi}(x)\gamma^\mu\psi(x)$ is the same current as used in Equation (3.13), and I have made use of the fact that partial derivatives commute with the expectation value. There remains some freedom in the choice of the operator O . If we were to select the identity in place of O , this would make the conserved nature of the current j^μ immediately apparent. The quantity that is conserved in this particular case is electric charge, making j^μ a charged current. Since the $U(1)$ group element commutes trivially with the spinor structures within the vector current, one can show that the right-hand side of the Ward identity vanishes in the case where j^μ is inserted in place of O , leaving us with

$$\partial_\mu \langle j^\mu(x) j^\nu(0) \rangle = 0. \quad (3.34)$$

Applying a Fourier transform to this result gives $q_\mu \Pi^{\mu\nu}(q) = 0$, which indicates that gauge invariance requires that the HVP is purely transverse with respect to the motion of the photon. Although the present discussion concerns the hadronic component of the vacuum polarisation, this result arises from QED and hence is generally applicable to the vacuum polarisation.

One should note that Equation (3.34) pertains to the continuum theory only. The discretised spacetime of lattice QCD means that the Ward identity assumes a different form. I will discuss the details of this in the next chapter, in Section 4.3.

With the Ward identity derived it is now possible to extract the tensor structure from $\Pi^{\mu\nu}(q)$. First we note that the HVP has no pole at $q^2 = 0$, since the QCD mass gap

²The action in Equation (2.30) is a real number and so commutes trivially with the operator O .

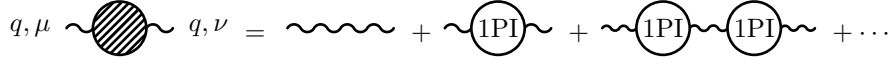


Figure 3.6: The renormalised photon propagator $D_{\mu\nu}(q)$, written as an infinite series of one-particle-irreducible diagrams.

indicates that there can be no massless intermediate states. In addition, the HVP tensor is symmetric under $\mu \leftrightarrow \nu$. Therefore the only two Lorentz structures that can appear in the decomposition are $g^{\mu\nu}$ and $q^\mu q^\nu$ such that the most general tensor decomposition is given by

$$\Pi^{\mu\nu}(q) = \Pi_1(q^2) \cdot q^2 g^{\mu\nu} - \Pi_2(q^2) \cdot q^\mu q^\nu. \quad (3.35)$$

To satisfy the Ward identity, we require that $\Pi_1 = \Pi_2 \equiv \Pi$ such that

$$\Pi^{\mu\nu}(q) = (q^2 g^{\mu\nu} - q^\mu q^\nu) \Pi(q^2). \quad (3.36)$$

This is the origin of the HVP form factor, $\Pi(q^2)$.

The vector Ward identity has direct consequences for the photon self-energy, which can be written as the series of one-particle-irreducible diagrams shown in Figure 3.6. Mathematically one can write this expansion as³ [94, 95]

$$D_{\mu\nu}(q) = \frac{-ig_{\mu\nu}}{q^2} + \frac{-ig_{\mu\rho}}{q^2} [i(q^2 g^{\rho\sigma} - q^\rho q^\sigma) \Pi(q^2)] \frac{-ig_{\sigma\nu}}{q^2} + \dots \quad (3.37)$$

This expression can be simplified by contracting the tensor structures in the expansion and evaluating the infinite geometric series in $\Pi(q^2)$, such that

$$D_{\mu\nu}(q) = -\frac{i}{q^2(1 - \Pi(q^2))} \left(g_{\mu\nu} - \frac{q_\mu q_\nu}{q^2} \right) - \frac{i}{q^2} \left(\frac{q_\mu q_\nu}{q^2} \right). \quad (3.38)$$

When this exact propagator is included in an S -matrix calculation, it must be connected to at least one fermion line. In this case the Ward identity dictates that terms proportional to q_μ or q_ν must vanish, giving us an abbreviated form of the exact propagator:

$$D_{\mu\nu}(q) = -\frac{ig_{\mu\nu}}{q^2(1 - \Pi(q^2))}, \quad (3.39)$$

which shows that the photon is massless at all orders of perturbation theory. This is a direct consequence of the Ward identity and gauge invariance.

The residue of the pole in the renormalised photon propagator at $q^2 = 0$ is given by

$$\frac{1}{1 - \Pi(0)} \equiv Z_3, \quad (3.40)$$

³For the remainder of this subsection $\Pi(q^2)$ represents the subtracted form of the vacuum polarisation form factor.

where Z_3 is the charge renormalisation constant, which relates the unobservable bare charge e_0 to the observed charge e via $e = \sqrt{Z_3}e_0$. One can interpret this as the screening of the bare charge of a particle by a cloud of virtual particle-antiparticle pairs. Since the bare charge is unobservable there is some freedom in the choice of Z_3 . When renormalising QED as a theory, however, one must specify a set of renormalisation conditions in accordance with the renormalisation scheme one is working in. By convention one sets $\Pi(q^2 = 0) = 0$, or $Z_3 = 1$. This motivates the subtraction of the UV divergence in the vacuum polarisation illustrated previously in Equations (3.15) and (3.27).

3.3.3 Ultraviolet Divergence

In Sections 3.2.2, 3.3.1 and 3.3.2 I have stated that the HVP contains a UV divergence that must be subtracted to compute physically meaningful quantities. I now motivate this subtraction by studying the one-loop contribution to the vacuum polarisation in QED.

The QED Feynman rules allow the LO vacuum polarisation tensor to be expressed as

$$\begin{array}{c}
 \begin{array}{c}
 \text{---} k \text{---} \\
 \circlearrowleft \\
 \text{---} k - q \text{---} \\
 \circlearrowright
 \end{array}
 \begin{array}{c}
 q, \mu \\
 \bullet \\
 \bullet \\
 q, \nu
 \end{array}
 \end{array}
 = -e^2 \int \frac{d^4 k}{(2\pi)^4} \frac{\text{Tr}[(\not{k} + m)\gamma^\mu(\not{k} - \not{q} + m)\gamma^\nu]}{(k^2 - m^2 + i\epsilon)((k - q)^2 - m^2 + i\epsilon)}.$$

Superficially this diagram appears to have a quadratic UV divergence. I will now proceed to show that the divergence is actually logarithmic. Evaluating the trace gives

$$i\Pi^{\mu\nu}(q) = -4e^2 \int \frac{d^4 k}{(2\pi)^4} \frac{k^\mu(k + q)^\nu + k^\nu(k + q)^\mu - g^{\mu\nu}(k \cdot (k + q) - m^2)}{(k^2 - m^2 + i\epsilon)((k - q)^2 - m^2 + i\epsilon)}. \quad (3.41)$$

I then adopt the usual procedure⁴ of introducing Feynman parameters, introducing the shifted integration variable $\ell = k + xq$ and completing the square in the denominator. I then Wick rotate the integration variable ℓ such that $\ell^0 \rightarrow iL^0$ and $\ell^i \rightarrow L^i$. This gives

$$\begin{aligned}
 i\Pi^{\mu\nu}(q) = & -4ie^2 \int_0^1 dx \int \frac{d^4 L}{(2\pi)^4} \\
 & \times \frac{\frac{1}{2}g^{\mu\nu}L^2 - 2x(1-x)q^\mu q^\nu + g^{\mu\nu}(m^2 + x(1-x)q^2)}{(L^2 + \Delta)^2}, \quad (3.42)
 \end{aligned}$$

where $\Delta = m^2 - x(1-x)q^2$.

To evaluate this integral we must use some regularisation procedure. Traditional approaches to UV regularisation involve the explicit insertion of a UV cut-off scale [52,

⁴This procedure is well known, and a more detailed derivation may be found in [40].

53, 96, 97]. However, in the vacuum polarisation case these approaches generally violate gauge invariance and hence the Ward identity presented in Equation (3.34). One exception to this is *Pauli–Villars regularisation* [98], though the procedure in this case is complicated [99]. Instead I will employ *dimensional regularisation* [100], which automatically preserves gauge invariance and hence the Ward identity. In summary, the method involves computing the integral in d dimensions, where d can be taken to be sufficiently small to guarantee the convergence of the integral. Using this procedure the integral over L can be evaluated to give

$$i\Pi^{\mu\nu}(q) = -4ie^2 \int_0^1 dx \frac{1}{(4\pi)^{d/2}} \frac{\Gamma(2 - \frac{d}{2})}{\Delta^{2-d/2}} \\ \times [g^{\mu\nu}(-m^2 + x(1-x)q^2) + g^{\mu\nu}(m^2 + x(1-x)q^2) - 2x(1-x)q^\mu q^\nu], \quad (3.43)$$

from which it is apparent that the factor $g^{\mu\nu}q^2 - q^\mu q^\nu$ can be extracted, which indicates the transversality of the vacuum polarisation at one loop. The associated form factor $\Pi(q^2)$ is given by

$$\Pi(q^2) = -\frac{8e^2}{(4\pi)^{d/2}} \int_0^1 dx x(1-x) \frac{\Gamma(2 - \frac{d}{2})}{\Delta^{2-d/2}}. \quad (3.44)$$

Introducing $\epsilon = (4 - d)/2$ and taking the limit $\epsilon \rightarrow 0$, one then uses the following approximation to write out the divergences explicitly in the result

$$\Gamma(\epsilon) \approx \frac{1}{\epsilon} - \gamma + \dots, \quad (3.45)$$

where $\gamma = 0.5772\dots$ is the Euler–Mascheroni constant. This gives the result

$$\Pi(q^2) \xrightarrow{\epsilon \rightarrow 0} -\frac{2\alpha}{\pi} \int_0^1 dx x(1-x) \left(\frac{1}{\epsilon} - \log \Delta - \gamma + \log(4\pi) \right), \quad (3.46)$$

where I have introduced the QED coupling $\alpha = e^2/4\pi$. Equation (3.46) provides the motivation for the infrared subtraction outlined earlier in this chapter: the pole suggests that the vacuum polarisation form factor is infinite. Not only is this undesirable from a mathematical perspective, it also suggests that the bare electric charge e_0 on a particle is infinitely larger than its observed charge e . The subtraction $\Pi(q^2) - \Pi(0)$ removes the pole $1/\epsilon$ as well as γ and $\log(4\pi)$, leaving

$$\Pi(q^2) - \Pi(0) = -\frac{2\alpha}{\pi} \int_0^1 dx x(1-x) \log \left(\frac{m^2}{m^2 - x(1-x)q^2} \right). \quad (3.47)$$

This results contains a branch cut on the real axis starting at $q^2 = 4m^2$, as predicted through the spectral representation discussed in Section 3.3.1. Evaluating the integral over the Feynman parameter x gives [6]

$$\Pi(q^2) - \Pi(0) = -\frac{\alpha}{3\pi} \left[\frac{8}{3} - \beta_\ell^2 + \frac{1}{2}\beta_\ell(3 - \beta_\ell^2) \log \frac{\beta_\ell - 1}{\beta_\ell + 1} \right], \quad \beta_\ell = \sqrt{1 - \frac{4m_\ell^2}{q^2}}, \quad (3.48)$$

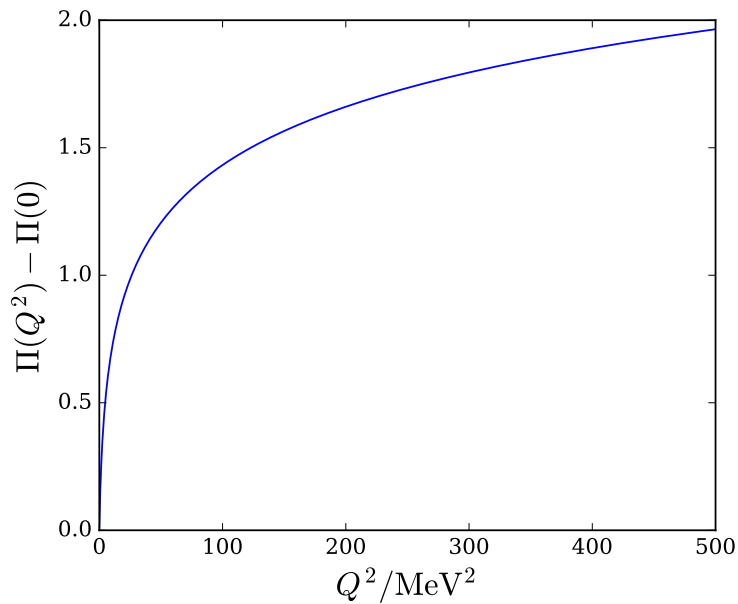


Figure 3.7: The one-loop QED vacuum polarisation in Euclidean space, Wick rotated from Equation (3.48) such that $Q^2 = -q^2$. The lepton mass in this case has been set at the mass of the electron.

which has the imaginary part

$$\text{Im}(\Pi(q^2) - \Pi(0)) = \frac{\alpha}{3} \left(1 + \frac{2m_\ell^2}{q^2} \right) \beta_\ell. \quad (3.49)$$

Figure 3.7 shows the shape of this function in Euclidean space. The qualitative behaviour observed in this plot is also found in the HVP form factor, which I will discuss in more detail in Chapter 5.

For high-energy off-shell photons, where $-q^2 \gg m^2$, the subtracted vacuum polarisation can be evaluated as

$$\Pi(q^2) - \Pi(0) = \frac{\alpha}{3\pi} \left[\log \left(\frac{-q^2}{m^2} \right) - \frac{5}{3} + \mathcal{O} \left(\frac{m^2}{q^2} \right) \right], \quad (3.50)$$

which, when compared with Equation (3.39), implies that the QED coupling α scales with q^2 as

$$\alpha(q^2) = \frac{\alpha}{1 - \frac{\alpha}{3\pi} \left[\log \left(\frac{-q^2}{m^2} \right) - \frac{5}{3} \right]}. \quad (3.51)$$

Therefore at high energies or short distances we expect the effective charge on the electron to increase. One can interpret this as a decrease in the level of charge screening as one penetrates the cloud of virtual particle-antiparticle pairs.

3.4 Euclidean Space Formulation

Lattice QCD calculations take place in Euclidean space, for reasons that I will explain in the next chapter. As such it is necessary to derive a formalism for computing $a_\mu^{(2)\text{had}}$ in Euclidean space. The Feynman diagram for $a_\mu^{(2)\text{had}}$ in panel (d) of Figure 3.1 can be considered equivalent to the pure QED Schwinger term in panel (a) with the photon propagator altered to account for the HVP. This is permissible given that the photon self-energy amounts to a multiplicative renormalisation of the photon propagator.

In Appendix B I derive the following formula for computing the QED Schwinger term in Euclidean space [101]:

$$a_\mu^{(1)\text{QED}} = \frac{\alpha}{\pi} \int_0^\infty dQ^2 f(Q^2), \quad (3.52)$$

where the QED kernel f is defined in Euclidean space by

$$f(Q^2) = \frac{m_\mu^2 Q^2 Z^3 (1 - Q^2 Z)}{1 + m_\mu^2 Q^2 Z^2}, \quad \text{where} \quad Z = -\frac{Q^2 - \sqrt{Q^4 + 4m_\mu^2 Q^2}}{2m_\mu^2 Q^2}, \quad (3.53)$$

and m_μ and Q are the muon mass and Euclidean four-momentum of the photon in the loop, respectively.

With a Euclidean formula derived for computing $a_\mu^{(1)\text{QED}}$, it now remains to include the effects of the HVP on the photon present in the loop. Here we note that the momentum Q in Equation (3.54) is that of the photon. Furthermore, the hadronic contributions to the photon self-energy do not affect the rest of the integral. This allows us to include the hadronic effects by multiplying the integrand f by the infrared-subtracted HVP. Mathematically, we can now write

$$a_\mu^{(2)\text{had}} = \left(\frac{\alpha}{\pi}\right)^2 \int_0^\infty dQ^2 f(Q^2) \times \hat{\Pi}(Q^2), \quad (3.54)$$

where $\hat{\Pi}(Q^2) = \Pi(Q^2) - \Pi(0)$ is the subtracted HVP form factor. One can equally replace $\hat{\Pi}(Q^2)$ with any other vacuum polarisation form factor. Indeed, this can be used to illustrate the validity of Equation (3.54). Using Equation (3.48) in place of $\hat{\Pi}$ we can compute two of the α^2 contributions to a_μ from QED by using either the electron or muon mass in the expression for the vacuum polarisation. One then obtains 5.904×10^{-6} when the electron mass is used and 8.464×10^{-8} when the muon mass is used, both of which are in agreement with values computed in the literature [6, 102, 103]. I plot the integrands associated with these results in Figure 3.8. Both of these plots illustrate the prominent peak present in the integrand at low- Q^2 . The existence of this peak is not limited to the case where $\hat{\Pi}$ is the pure QED photon self-energy. As I will discuss in more detail in Chapter 5, the peak at small Q^2 in the function $f(Q^2)\hat{\Pi}(Q^2)$ creates significant difficulties when computing $a_\mu^{(2)\text{had}}$ on the lattice.

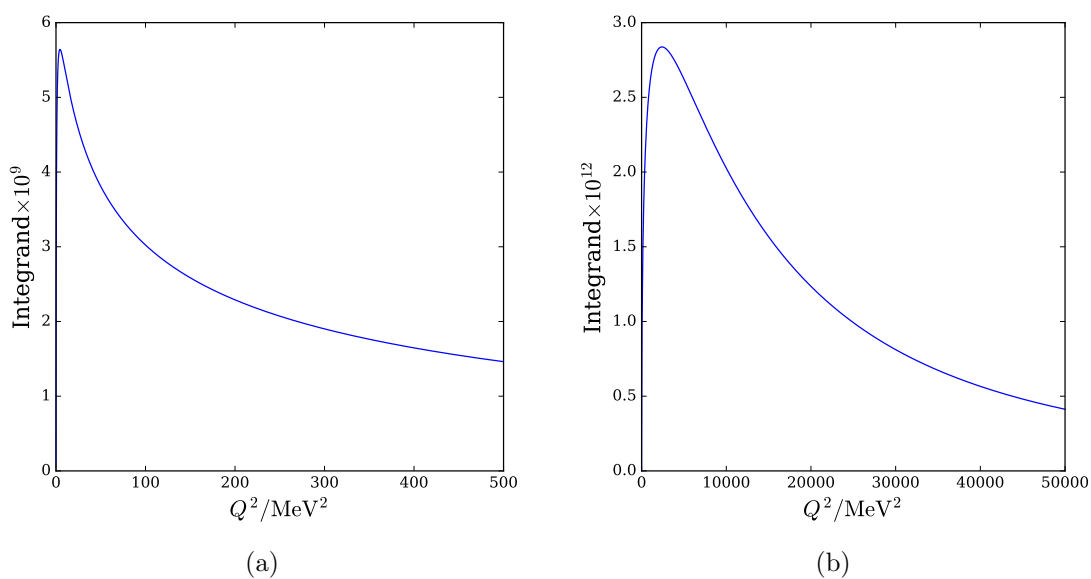


Figure 3.8: Plots of the integrand in Equation (3.54) where the one-loop QED vacuum polarisation has been used in place of $\hat{\Pi}$. Panel (a) shows the integrand produced when the vacuum polarisation loop contains an electron, whilst panel (b) shows the integrand when the same loop contains a muon.

Chapter 4

Lattice QCD

Lattice QCD is the lattice field theory formulation of QCD. It is currently the only viable *ab initio* method for computing QCD observables at low energies, where the coupling $\alpha_s \sim \mathcal{O}(1)$ and perturbative methods are unreliable. This chapter will present the formulation of Lattice QCD and a selection of methods used to calculate observable quantities. In Section 4.1 I will describe how the gauge fields and fermions of QCD are formulated on the lattice. This is followed by a discussion of the general methods used in lattice computations in Section 4.2. In Section 4.3 I describe how the discrete nature of lattice derivatives result in a different form of the vector Ward identity. Finally, in Section 4.4 I discuss domain wall fermions (DWFs), the particular discretisation of fermions used in this work.

4.1 Discretising QCD

I will now describe how the continuum theory of QCD is discretised in a finite volume, hypercubic lattice with periodic boundary conditions. This process imposes explicit infrared and ultraviolet cut-off scales, thus regularising the theory. To compute physical observables, these regulators must be removed, meaning continuum and infinite volume limits must be taken before computed values can be compared to experiment.

4.1.1 Euclidean Path Integrals

Lattice QCD is formulated in Euclidean spacetime, achieved through the use of a Wick rotation [104], such that $t \rightarrow t' = it$ and the path integral becomes [105, 106]

$$\langle O \rangle = \frac{1}{Z} \int \mathcal{D}[\bar{\psi}, \psi, A] O e^{iS[\bar{\psi}, \psi, A]} \rightarrow \frac{1}{Z} \int \mathcal{D}[\bar{\psi}, \psi, A] O e^{-S[\bar{\psi}, \psi, A]}, \quad (4.1)$$

where ψ and $\bar{\psi}$ are the fermionic degrees of freedom, A are the gluonic degrees of freedom, S is the QCD action and $Z = \langle \cdot \rangle$ is the QCD partition function. The fermion fields are represented by anti-commuting Grassmann numbers, which cannot be represented on computers. Instead, we seek to express the path-integral as an integral over the gauge degrees of freedom alone. The partition function above can be re-expressed using the following argument. First, the action can be split into its gluonic and fermionic components, since $S[\bar{\psi}, \psi, A] = S_G[A] + S_F[\bar{\psi}, \psi, A]$. The fermionic component can be written $S_F[\bar{\psi}, \psi, A] = \int d^4x \bar{\psi} D \psi$, where D is the massive Euclidean Dirac operator containing the gauge field via the covariant derivative. Since S_F is bilinear in the fermion fields, the latter can be integrated out using the Matthews–Salam formula [107, 108], introducing the fermion determinant $\det D$ such that

$$Z = \int \mathcal{D}A \det D e^{-S_G[A]}. \quad (4.2)$$

A similar argument also applies when considering the numerator of the path integral, though if O contains Grassmannian fields Wick’s theorem may be required to express the interpolating operator O as a function of only the gauge field. I discuss the details of this process in Section 4.2.2.

4.1.2 Field Discretisation

In translating continuum QCD onto a discrete lattice derivatives are replaced by finite differences and integrals by Riemann sums. Fermions are placed at the nodes, or *sites* of the lattice. This leads to a natural choice when considering an appropriate finite difference approximation to the continuum derivative

$$\partial_\mu f(x) = \frac{1}{2}(\Delta_\mu + \Delta_\mu^*)f(x) + \mathcal{O}(a^2), \quad (4.3)$$

where a is the spacing between lattice sites and the forward and backward first-order discrete derivatives are given by

$$\Delta_\mu f(x) = \frac{f(x + \hat{\mu}) - f(x)}{a} \quad (4.4)$$

$$\Delta_\mu^* f(x) = \frac{f(x) - f(x - \hat{\mu})}{a}, \quad (4.5)$$

and $\hat{\mu}$ is an offset of length a in the μ th axis. Spacetime integrals in the continuum are replaced with a Riemann sum:

$$\int d^4x \rightarrow a^4 \sum_{x \in \Lambda}, \quad (4.6)$$

where Λ is the set of all lattice sites, given by

$$\Lambda = \{x; x_\mu = an_\mu; n_\mu = 0, 1, \dots, N_\mu - 1\}, \quad (4.7)$$

and N_μ is the number of lattice sites in the μ th dimension.

Using these replacements, the free, massless one-flavour QCD action could be approximated by

$$S = a^4 \sum_{x \in \Lambda} \sum_{\mu} \frac{1}{2a} \bar{\psi}(x) \gamma_{\mu} (\psi(x + \hat{\mu}) + \psi(x - \hat{\mu})), \quad (4.8)$$

where the properties of the Euclidean gamma matrices γ_{μ} are outlined in Appendix A. However, if we examine the behaviour of this action under a gauge transformation, such that

$$\psi(x) \rightarrow \psi'(x) = \Omega(x)\psi(x), \quad (4.9)$$

$$\bar{\psi}(x) \rightarrow \bar{\psi}'(x) = \bar{\psi}(x)\Omega^\dagger(x), \quad (4.10)$$

where Ω is an element of $SU(3)$, then the action will not be gauge invariant, since terms such as $\bar{\psi}(x)\psi(x + \hat{\mu})$ will undergo the following transformation:

$$\bar{\psi}(x)\psi(x + \hat{\mu}) \rightarrow \bar{\psi}(x)\Omega^\dagger(x)\Omega(x + \hat{\mu})\psi(x + \hat{\mu}). \quad (4.11)$$

This motivates the gauge field sited on links between lattice sites. We introduce the *gauge link* $U_\mu(x)$ as a group element of $SU(3)$ originating at lattice site x and orientated such that it points towards site $x + \hat{\mu}$ [106]. The link originating at site x and orientated such that it points towards site $x - \hat{\mu}$ is given by $U_{-\mu}(x) \equiv U_\mu^\dagger(x - \hat{\mu})$. The gauge links transform as

$$U_\mu(x) \rightarrow U'_\mu(x) = \Omega^\dagger(x)U_\mu(x)\Omega^\dagger(x + \hat{\mu}), \quad (4.12)$$

meaning that the product $\bar{\psi}(x)U_\mu(x)\psi(x + \hat{\mu})$ is gauge invariant. The relationship between $U_\mu(x)$ and the continuum gauge field $A_\mu(x)$ is given by $U_\mu(x) = e^{iagA_\mu(x)}$ where g is the QCD coupling on the lattice. The gauge is therefore fundamentally expressed as a group element of $SU(3)$ rather than a member of the Lie algebra. Within the QCD path integral this change is reflected through the exchange of the measure $\mathcal{D}[A]$ for the measure $\mathcal{D}[U]$, given explicitly by the product measure

$$\mathcal{D}[U] = \prod_{x \in \Lambda} \prod_{\mu} dU_\mu(x). \quad (4.13)$$

The measure $dU_\mu(x)$ is the *Haar measure*, a measure for integrations over a continuous compact Lie group. One of the defining properties of the Haar measure is that it is gauge invariant.

The procedure of discretisation I have described necessarily produces a lattice action S that is not identical to that of continuum QCD. However, it must be formulated such that it approaches the continuum QCD action when the continuum limit is taken. This removes the UV regulator such that the meaningful physical theory of QCD is simulated.

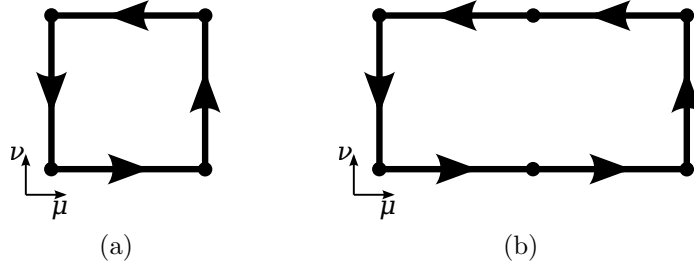


Figure 4.1: Pictorial representations of the Wilson plaquette (left) and rectangle (right) operators.

Furthermore, to compute physically meaningful quantities the IR regulator must also be removed by taking an infinite volume limit.

4.1.3 Gauge Actions

With gauge invariance specified for lattice QCD it is necessary to determine an action that exhibits the correct continuum limit behaviour whilst also being gauge invariant. I shall first discuss the component of the action dependent solely on the gauge field. The simplest gauge invariant object that may be constructed solely from gauge links is the Wilson plaquette (see panel (a) in Figure 4.1). From this the Wilson plaquette action may be constructed [106]:

$$S_G = \frac{2}{g^2} \sum_{x \in \Lambda} \sum_{\mu < \nu} \text{Re tr} [\mathbb{1} - P_{\mu\nu}(x)], \quad (4.14)$$

where the Wilson plaquette $P_{\mu\nu}(x)$ is given mathematically by

$$P_{\mu\nu}(x) \equiv U_\mu(x)U_\nu(x + \hat{\mu})U_\mu^\dagger(x + \hat{\nu})U_\nu^\dagger(x). \quad (4.15)$$

Using the Baker-Campbell-Hausdorff formula, it is possible to show that this action tends toward that of the continuum as the continuum limit is taken. The expansion of the exponentials in the expression of the gauge links $U_\mu(x) = e^{iagA_\mu(x)}$ gives

$$S_G = \frac{a^4}{2g^2} \left[\sum_x \sum_{\mu, \nu} \text{tr}[F_{\mu\nu}^2(x)] + \mathcal{O}(a^2) \right], \quad (4.16)$$

which illustrates that the continuum action is restored in the continuum limit, as $a \rightarrow 0$. The $\mathcal{O}(a^2)$ discretisation errors can be reduced through the inclusion of other terms in the action, such as the rectangle operator, also shown graphically in Figure 4.1. Denoting the rectangle operator $R_{\mu\nu}(x)$, a generic, rectangle-improved gauge action may be written

$$S_G = \frac{2}{g^2} \sum_x \sum_{\mu < \nu} [\mathbb{1} - c_0 P_{\mu\nu}(x) - c_1 R_{\mu\nu}(x)], \quad (4.17)$$

with the condition that $c_0 + 8c_1 = 1$ to ensure the correct continuum limit. The value of c_1 can be tuned using various methods to give different actions. For example, the Lüscher–Weisz action uses $c_1 = -1/12$ [109–111], the Iwasaki action uses $c_1 = -0.331$ [112, 113], and the DBW2 action uses $c_1 = 1.4069$ [114].

4.1.4 Fermion Actions

Using the covariant discrete derivative described in Section 4.1.2, a naïve fermion action would be

$$S_F = a^4 \sum_{x \in \Lambda} \bar{\psi}(x) \left[\sum_{\mu} \gamma_{\mu} \frac{U_{\mu}(x)\psi(x + \hat{\mu}) - U_{\mu}^{\dagger}(x - \hat{\mu})\psi(x - \hat{\mu})}{2a} + m\psi(x) \right], \quad (4.18)$$

where the properties of the Euclidean gamma matrices are outlined in Appendix A. From the specification of the gauge transformations of fermions and the gauge field in Equations (4.9), (4.10) and (4.12) it is apparent that this action is gauge invariant.

Working in the free theory (setting $U_{\mu}(x) = \mathbb{1}$ above) and studying the action in momentum space illustrates a technical difficulty associated with this action. In momentum space

$$S_F = \sum_{p \in \tilde{\Lambda}} \bar{\psi}(p) \tilde{D}(p) \psi(p), \quad (4.19)$$

where the momentum space Dirac matrix $\tilde{D}(p)$ is derived as

$$\tilde{D}(p) = m\mathbb{1} + \frac{i}{a} \sum_{\mu} \gamma_{\mu} \sin(ap_{\mu}), \quad (4.20)$$

and $\tilde{\Lambda}$ is the set of discrete lattice momenta resulting from the imposition of a finite volume with periodic boundary conditions, given by

$$\tilde{\Lambda} = \left\{ p; ap_{\mu} = \frac{2\pi n_{\mu}}{N_{\mu}}; n_{\mu} \in \mathbb{Z}, -\frac{N_{\mu}}{2} \leq n_{\mu} < \frac{N_{\mu}}{2} \right\}, \quad (4.21)$$

where N_{μ} is the extent of the lattice in dimension μ . We can invert this expression to compute the free fermion propagator, obtaining

$$\tilde{D}^{-1}(p) = \frac{m\mathbb{1} - ia^{-1} \sum_{\mu} \gamma_{\mu} \sin(ap_{\mu})}{m^2 + a^{-2} \sum_{\mu} \sin^2(ap_{\mu})}, \quad (4.22)$$

which suggests there will be degenerate poles: in the massless case, for example, the propagator has poles at both 0 and π . In four dimensions we should therefore expect sixteen degenerate fermion states. These degenerate modes are known as *doublers*. If we are to compute meaningful observables using lattice QCD, then we require a non-degenerate pole corresponding to a single physical quark.

One solution to the doubler problem was proposed by Wilson [115]. The solution involves giving a large mass to doublers of the order of the ultraviolet cut-off a^{-1} such that in the continuum limit they become infinitely heavy and decouple. The Wilson Dirac operator takes the form

$$\tilde{D}_W(p) = m\mathbb{1} + \frac{i}{a} \sum_{\mu} \gamma_{\mu} \sin(ap_{\mu}) + \frac{1}{a} \sum_{\mu} (1 - \cos(ap_{\mu})), \quad (4.23)$$

with the summation involving the cosine constituting the Wilson term. In position space the Wilson action is given by

$$S_F = \bar{\psi} D_W \psi \equiv \sum_{x \in \Lambda} \left[\left(m + \frac{4}{a} \right) \bar{\psi}(x) \psi(x) - \frac{1}{2a} \sum_{\mu} \bar{\psi}(x) \left((1 - \gamma_{\mu}) U_{\mu}(x) \psi(x + \hat{\mu}) + (1 + \gamma_{\mu}) U_{\mu}^{\dagger}(x - \hat{\mu}) \psi(x - \hat{\mu}) \right) \right]. \quad (4.24)$$

The disadvantage of Wilson fermions is that they explicitly break chiral symmetry in the massless limit. Since $\{\gamma_{\mu}, \gamma_5\} = 0$, we expect a general, chirally symmetric Dirac operator, which is proportional to γ_{μ} , to also anti-commute with the fifth gamma matrix. From Equation (4.23), it is immediately apparent that the Wilson Dirac operator does not satisfy this condition as a direct result of the inclusion of the Wilson term. Unfortunately a no-go theorem proved by Nielsen and Ninomiya dictates that it is not possible to formulate a lattice Dirac operator D that obeys $\{\gamma_5, D\} = 0$ for a local theory with an even number of dimensions [116]. I will discuss chiral symmetry in more detail later in this chapter.

Wilson fermions are one of many fermion actions used in lattice QCD computations. Various other actions have been proposed, each with their own merits. Later in this chapter I will discuss *domain wall fermions*, the fermion formulation used in the present work.

4.2 Lattice Methodology

In this section I will describe in more detail how lattice simulations are executed in practice, focussing on the techniques of most relevance to the present work.

4.2.1 Ensemble Generation

The Euclidean path integral in Equation (4.1), when considered on a lattice, contains a large number of degrees of freedom, making its explicit evaluation infeasible¹. Instead,

¹For example, the two dynamical ensembles described later in this work each have $\mathcal{O}(10^8)$ lattice sites. At each site there are then 12 degrees of freedom for a four-spinor and 32 degrees of freedom for four $SU(3)$ gauge links.

Monte Carlo methods are used to compute an approximation to the true value of the integral. More specifically, a Markov-chain algorithm is used to generate a series of N_{cfg} field configurations $\{U_n; n = 1, 2, \dots, N_{\text{cfg}}\}$, or *ensembles*, which are sampled from the distribution defined by the probability weight $\det[D] \exp(-S[U])$ [106, 117]. Expectation values of observables are then evaluated by computing the observable on each configuration then averaging the results:

$$\langle O \rangle = \frac{1}{N_{\text{cfg}}} \sum_{n=1}^{N_{\text{cfg}}} O_n + \mathcal{O} \left(\frac{1}{\sqrt{N_{\text{cfg}}}} \right), \quad (4.25)$$

where O_n is the result of measuring the observable O on configuration U_n , and the second term on the right-hand side arises from the stochastic nature of the Monte Carlo algorithm. This error can be estimated using resampling methods such as the statistical jackknife and bootstrap [118], the latter of which I use in the present work.

The Markov process generates a new gauge configuration U_{n+1} from the previous configuration U_n with transition probability $T(U_{n+1}, U_n)$. The transition probability must satisfy the detailed balance equation

$$T(U_{n+1}|U_n)P(U_n) = T(U_n|U_{n+1})P(U_{n+1}), \quad (4.26)$$

where $P(U_n)$ is the probability of the system existing with configuration U_n . Physical measurements in Lattice QCD require that configurations in the ensemble are generated under conditions of equilibrium, which is achieved by running the Markov process for a sufficiently large number of steps, a process known as *thermalisation*. Since each configuration in the ensemble is generated from the previous one, there will be correlation between the two [119]. To account for the resulting *autocorrelation*, measurements are usually performed on configurations separated by a sufficient number of Markov steps [120]. This guarantees that the various measurements fully sample the available phase space and not a subset of it.

Algorithms used to perform the Markov updates are designed to accelerate this sampling process. From a historical perspective, the fermion determinant within the path integral was set to unity [121], since it was very expensive to compute and the systematic error arising from this approximation was anticipated to be less than 10%. This assumption equates to neglecting the effects of virtual quark loops in the QCD vacuum, also known as *sea quarks*. Simulations using this approach are said to use the *quenched approximation*. For quenched simulations, the heatbath [122] and overrelaxation [123] algorithms achieve efficient sampling by exploiting the distribution to select optimal values for the new gauge field. Although this simplifies the calculation, it also introduces a systematic error [124], and modern computations now include the effect of sea quarks to account for this. For dynamical simulations, where the effects of sea quarks are included, the hybrid Monte

Carlo (HMC) [125] algorithm is used to incorporate the fermion determinant into the probability weight in an efficient manner.

4.2.2 Correlation Functions

Hadronic observables computed using lattice QCD require the computation of n -point functions. I shall outline the case of computing the ground state energy of a meson two-point function. The amplitude for the creation and propagation of a quark-antiquark pair from lattice site x to site y is given by the VEV $\langle 0|\mathcal{O}(y)\mathcal{O}^\dagger(x)|0\rangle$, where the meson interpolator $\mathcal{O}(x) = \bar{q}_i(x)\Gamma q_j(x)$ creates an antiquark and quark with flavours i and j , respectively. Γ is a product of gamma matrices specifying the spin structure of the quark-antiquark pair. In addition, to extract the energy of the meson state we must project the correlator to a definite momentum using a Fourier transform. The resulting correlator has the form

$$C(\mathbf{p}, t) = a^3 \sum_{\mathbf{x} \in \Lambda} e^{-i\mathbf{p} \cdot \mathbf{x}} \langle 0|\mathcal{O}(\mathbf{x}, t)\mathcal{O}^\dagger(\mathbf{0}, 0)|0\rangle, \quad (4.27)$$

where Λ is the set of all spatial lattice sites. Translation invariance has also been used to shift the creation of the quark-antiquark pair to the site $(\mathbf{0}, \mathbf{0})$. The operator $\mathcal{O}^\dagger(\mathbf{0}, 0)$ acts at the source location $(\mathbf{0}, 0)$ whilst the operator $\mathcal{O}(\mathbf{x}, t)$ acts at the sink location (\mathbf{x}, t) . Defining

$$\tilde{\mathcal{O}}(\mathbf{p}, t) = a^3 \sum_{\mathbf{x} \in \Lambda} e^{-i\mathbf{p} \cdot \mathbf{x}} \mathcal{O}(\mathbf{x}, t), \quad (4.28)$$

we can write the temporal dependence of the interpolator explicitly using $\mathcal{O}(\mathbf{x}, t) = e^{Ht}\mathcal{O}(\mathbf{x}, 0)e^{-Ht}$. This relationship and the insertion of a complete set of states allows us to write

$$C(\mathbf{p}, t) = a^2 \sum_{n=0}^{\infty} \frac{|\langle 0|\tilde{\mathcal{O}}(\mathbf{0}, 0)|n\rangle|^2}{2E_n} e^{-E_n t}, \quad (4.29)$$

where the energy E_n of state $|n\rangle$ arises from the Hamiltonian H acting on the state. It should hence be possible to determine the matrix elements $\langle 0|\tilde{\mathcal{O}}(\mathbf{0}, 0)|n\rangle$ and the energies E_n by fitting a sum of exponentials to the correlator $C(\mathbf{p}, t)$. If the fit is performed at sufficiently large times then excited states will be exponentially suppressed and the ground state may be obtained. One should note that this derivation has neglected the periodic boundary conditions that are used in lattice simulations, which permit backward propagating states travelling in the negative time direction. In practice this means that the ground state can be approximated at large times by

$$C(t) \stackrel{0 \ll t \ll T}{\approx} A e^{-E_0 t} \pm B e^{-E'_0 (T-t)}, \quad (4.30)$$

where A and B are proportionality constants, T is the temporal extent of the lattice and E_0 and E'_0 are the ground state energies of the forward and backward propagating states,

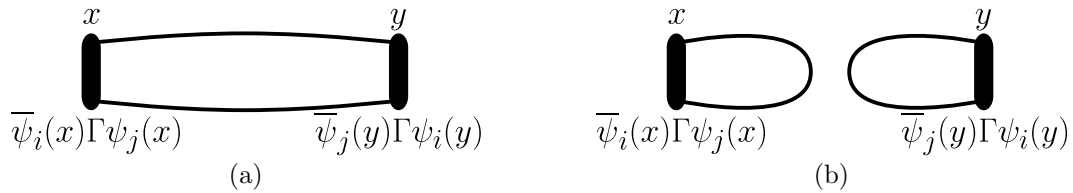


Figure 4.2: Quark flow diagrams of a meson two-point function. In the quark-connected diagram in panel (a), a quark-antiquark pair is created by the operator $\bar{\psi}_i(x)\Gamma\psi_j(x)$ at the source point x and propagated to the sink at point y , where the pair is annihilated by the operator $\bar{\psi}_j(y)\Gamma\psi_i(y)$. Panel (b) shows the quark-disconnected contribution, where each particle is created and annihilated at the same quark source. This second case is only possible where the quark flavours i and j are identical.

respectively. Here I have accounted for the possibility that the forward and backward propagating states are not mass degenerate. Where they are, the correlator takes the shape of a cosh or sinh function.

To compute n -point correlation functions in lattice QCD it is necessary to perform Wick contractions [91] on the fermion fields such that the correlation function can be written purely in terms of ordinary c -numbers. This is achieved in a similar manner to how Wick-contractions are performed in the continuum theory: the product of two quark fields $\psi(x)\bar{\psi}(y)$ is Wick contracted as

$$\overline{\psi(x)\bar{\psi}(y)} = S(x, y), \quad (4.31)$$

where $S(x, y)$ is the lattice propagator for a quark propagating from site x to site y . The propagator is computed by solving the linear equation $D \cdot S = \mathbb{1}$, which requires inverting the Dirac operator D . In practice the latter is represented by a large, square, sparse matrix with the number of rows and number of columns typically being $\mathcal{O}(10^9)$. As such it is impractical to compute the entire inverse of D , so instead one computes a one-to-all propagator, which describes the propagation of a quark from a particular lattice site to all other lattice sites. Although this may appear restrictive, translation invariance guarantees that results calculated this way remain universal. We therefore proceed by computing a single column of S , solving the equation $D\psi = \eta$ for ψ , where η is a source vector representing a single column of the identity matrix. This process is repeated for each of the twelve possible spin-colour combinations at the site of interest, producing a propagator that can be represented as a 12×12 complex matrix at each lattice site. On a practical level this is achieved using an iterative algorithm such as conjugate gradient (CG) [126], with the resulting propagator satisfying $D\psi = \eta$ up to a specified numerical tolerance.

The quantum numbers of a propagating hadronic state dictate the set of Wick contractions required in a calculation [91], and therefore the required set of quark propagators. Returning to the meson two-point function example, the quark-connected contribution,

as shown in panel (a) of Figure 4.2, is computed as the following Wick contraction

$$\langle 0 | \overline{\psi}_j(y) \Gamma \psi_i(y) \overline{\psi}_i(x) \Gamma \psi_j(x) | 0 \rangle = - \langle \text{tr}[\Gamma S_i(y, x) \Gamma S_j(x, y)] \rangle, \quad (4.32)$$

where S_i is the lattice propagator for the quark with flavour i , and the minus sign arises from commuting two of the Grassmannian quark fields. In general the lattice Dirac operator is γ_5 Hermitian such that $\gamma_5 D \gamma_5 = D^\dagger$. This is useful in the case of flavour diagonal mesons, as one can use the substitution $S^\dagger(x, y) = \gamma_5 S(y, x) \gamma_5$ when taking the above trace, allowing us to write

$$\langle 0 | \overline{\psi}(y) \Gamma \psi(y) \overline{\psi}(x) \Gamma \psi(x) | 0 \rangle = - \langle \text{tr}[\Gamma \gamma_5 S^\dagger(x, y) \gamma_5 \Gamma S(x, y)] \rangle, \quad (4.33)$$

thus removing the need to compute two propagators: one from x to y and one from y to x .

If the meson is a flavour singlet such that $i = j$ then its two-point function may receive quark-disconnected contributions (see panel (b) of Figure 4.2), provided each quark loop has quantum numbers identical to the vacuum. Such contributions result in the following expression after Wick contractions have been performed

$$\langle 0 | \overline{\psi}_i(y) \Gamma \psi_i(y) \overline{\psi}_i(x) \Gamma \psi_i(x) | 0 \rangle = \langle \text{tr}[\Gamma S_i(y, y)] \text{tr}[\Gamma S_i(x, x)] \rangle. \quad (4.34)$$

These contributions are computationally expensive for two reasons. The first relates to the need to compute the diagonal of the inverse of the Dirac matrix in order to obtain the propagator at each lattice site such that the resulting correlator can be projected onto a specified momentum as described above. Naïvely this requires the equation $D\psi = \eta$ to be solved twelve times for *every* lattice site such that many more calculations are required in the first instance. The second reason relates to the behaviour of the variance of the two-point function as the separation of the two lattice sites x and y increases. The trace $\text{tr}[\Gamma S_i(x, x)]$ will fluctuate around its central value, and because of translation invariance the magnitude of these fluctuations is independent of the lattice site x . Thus the magnitude of the fluctuations in the product of two such traces is constant with respect to the separation of their positions x and y . As a result, the signal-to-noise ratio in the correlator will deteriorate rapidly as separation between the sites x and y grows. Disconnected correlators are therefore inherently noisier than their connected counterparts, meaning a greater number of measurements are required to obtain the same level of accuracy in the meson mass or energy.

Recently it has been argued in [92] using partially-quenched QCD that each individual Wick contraction contributing to an n -point function has its own separate continuum and infinite volume limit. It is therefore possible to compute the contribution to an observable dependent on said n -point function from each Wick contraction in isolation before summing the results. This also means that the techniques and strategies used to

compute a particular contribution need not be the same as those used to compute the other contributions. Indeed, this allows for the techniques used to compute a particular contribution to be tailored to minimise the error in the final result. This knowledge will be invaluable in Chapter 5, where I discuss the computation of the quark-connected strange contribution to $a_\mu^{(2)\text{had}}$.

4.2.3 Quark Sources

When solving the Dirac equation $D\psi = \eta$ there is some freedom in selecting the source η . The simplest source is a point source, derived from the identity $D \cdot S = \mathbb{1}$ such that η is specified by [127]

$$\eta_{\alpha a}(x) = \delta_{xy} \delta_{\alpha\beta} \delta_{ab}, \quad (4.35)$$

where I have introduced spin and colour indices as Greek and Roman characters, respectively, for clarity. The variables y , β and b are the specified position, spin and colour at which the source should be non-zero.

Point sources are sensitive to spatial variations in the gauge field and do not make use of the entire lattice volume [128]. These drawbacks may be accounted for by averaging over the spatial volume. Stochastic \mathbb{Z}_2 wall sources provide a mechanism for performing this average [129–134]. A series of N_{hits} noise vectors $\eta^{(n)}$ are randomly generated and specified by

$$\eta_{\alpha a}^{(n)}(x) = \begin{cases} z & x_0 = y_0, \alpha = \beta, a = b \\ 0 & \text{otherwise,} \end{cases} \quad (4.36)$$

where y_0 specifies the timeslice at which the source should be located and β and b specify the spin and colour component of the source in the same manner as the point source case. The variable z is a member of the distribution \mathcal{D} , which is constructed such that

$$\lim_{N_{\text{hits}} \rightarrow \infty} \frac{1}{N_{\text{hits}}} \sum_{n=1}^{N_{\text{hits}}} \eta_{\alpha a}^{(n)}(\mathbf{x}) \eta_{\beta b}^{(n)\dagger}(\mathbf{y}) = \delta_{\mathbf{xy}} \delta_{\alpha\beta} \delta_{ab}, \quad (4.37)$$

meaning that a hit average over the stochastic noise is required in addition to the existing gauge average. In the particular case of \mathbb{Z}_2 wall sources \mathcal{D} is the complex $\mathbb{Z}_2 \otimes \mathbb{Z}_2$ distribution

$$\mathcal{D} = \left\{ \frac{1}{\sqrt{2}} (\pm 1 \pm i) \right\}. \quad (4.38)$$

Since both the gauge noise and \mathbb{Z}_2 source noise are uncorrelated, the combined probability distribution arising from both the gauge and source noise can be factorised such that the expectation values of these two distributions commute. This means that, given an ensemble with sufficiently many configurations, it is possible to use few \mathbb{Z}_2 wall sources per gauge configuration (as few as one in some cases) whilst still obtaining the large hit limit [128].

Meson correlators may be computed using \mathbb{Z}_2 wall sources via the *one-end trick* [128]. Consider the meson two-point function projected to zero momentum

$$C(\mathbf{0}, t) = a^6 \sum_{\mathbf{x}, \mathbf{y} \in \Lambda} \text{tr}[\gamma_5 \Gamma S(\mathbf{x}, t; \mathbf{y}, 0) \Gamma \gamma_5 S^\dagger(\mathbf{x}, t; \mathbf{y}, 0)], \quad (4.39)$$

where γ_5 -hermiticity has been used to write the correlation function in terms of a single propagator. The large hit limit described in Equation (4.37) can be used to insert a Kronecker delta into this expression, giving

$$C(\mathbf{0}, t) = a^9 \frac{1}{N_{\text{hits}}} \sum_{n=1}^{N_{\text{hits}}} \sum_{\mathbf{x}, \mathbf{y}, \mathbf{z} \in \Lambda} \text{tr}[\gamma_5 \Gamma S(\mathbf{x}, t; \mathbf{y}, 0) \eta^{(n)}(\mathbf{y}) \eta^{(n)\dagger}(\mathbf{z}) \Gamma \gamma_5 S^\dagger(\mathbf{x}, t; \mathbf{z}, 0)], \quad (4.40)$$

which can be written as

$$C(\mathbf{0}, t) = a^3 \frac{1}{N_{\text{hits}}} \sum_{n=1}^{N_{\text{hits}}} \sum_{\mathbf{x} \in \Lambda} \text{tr}[\mathcal{S}(\mathbf{x}, t) \mathcal{S}^{\Gamma\dagger}(\mathbf{x}, t) \gamma_5 \Gamma], \quad (4.41)$$

where

$$\mathcal{S}(\mathbf{x}, t) = a^3 \sum_{\mathbf{y} \in \Lambda} S(\mathbf{x}, t; \mathbf{y}, 0) \eta^{(n)}(\mathbf{y}), \quad (4.42)$$

$$\mathcal{S}^\Gamma(\mathbf{x}, t) = a^3 \sum_{\mathbf{y} \in \Lambda} S(\mathbf{x}, t; \mathbf{y}, 0) (\Gamma \gamma_5)^\dagger \eta^{(n)}(\mathbf{y}). \quad (4.43)$$

If the meson under study is a flavour singlet pseudoscalar, then $\Gamma = \gamma_5$ and $\mathcal{S} = \mathcal{S}^\Gamma$ such that only one set of inversions is required to compute the meson correlator. For all other values of Γ the spin structure can be computed explicitly by restricting the noise to colour space such that only four sets of inversions are required to compute the 16 possible meson correlators [128]. Although the use of \mathbb{Z}_2 wall sources does not guarantee a reduction in the statistical error on any observable, the authors of [128] note the improved statistical accuracy of both meson masses and the K_{l3} form factor when these sources are used.

4.3 Vector Ward Identity

The introduction of discretised spacetime has consequences for the form of the vector Ward identity on the lattice, since derivatives are now computed using finite differences. The immediate result of this is that the conserved vector current on the lattice takes a different form to that in the continuum.

The Euclidean formulation of Equation (2.30),

$$\left\langle O \frac{\delta S}{\delta \alpha(x)} \right\rangle = i \left\langle \frac{\delta O}{\delta \alpha(x)} \right\rangle, \quad (2.30)$$

is obtained by Wick rotating the theory such that $S \rightarrow iS$, giving

$$\left\langle O \frac{\delta S}{\delta \alpha(x)} \right\rangle = \left\langle \frac{\delta O}{\delta \alpha(x)} \right\rangle. \quad (4.44)$$

Since the action is a real-valued scalar, the two terms under the expectation value on the left-hand side can be switched without changing the validity of this equation. Applying a $U(1)$ vector transformation to the lattice fermion fields results in the following Ward identity:

$$\Delta_\mu^* \langle \mathcal{J}_\mu(x) O \rangle = \frac{i}{a^4} \left\langle \frac{\delta O}{\delta \alpha(x)} \right\rangle, \quad (4.45)$$

where $\mathcal{J}_\mu(x)$ is the conserved vector current for the action under consideration and Δ_μ^* is the backward lattice derivative that commutes with the expectation value. The factor of a^{-4} on the right-hand side arises from the discretised version of the spacetime integral in the lattice action. Since there are many variants of the action, we expect each to have a specific form for $\mathcal{J}_\mu(x)$. For example, the conserved vector current associated with Wilson fermions is given by [135]

$$\mathcal{J}_\mu(x) = \frac{1}{2} \left[\bar{\psi}(x + \hat{\mu})(1 + \gamma_\mu) U_\mu^\dagger(x) \psi(x) - \bar{\psi}(x)(1 - \gamma_\mu) U_\mu(x) \psi(x + \hat{\mu}) \right]. \quad (4.46)$$

Following from the discussion in Section 3.3.2, it is prudent to examine the vector Ward identity when O is the local vector current $J_\mu(x) = \bar{\psi}(x) \gamma_\mu \psi(x)$. Under the same $U(1)$ vector transformation this current is invariant, giving the following Ward identity

$$\Delta_\mu^* \langle \mathcal{J}_\mu(x) J_\nu(0) \rangle = 0, \quad (4.47)$$

which is similar form to the continuum Ward identity in Equation (3.34):

$$\partial_\mu \langle j^\mu(x) j^\nu(0) \rangle = 0. \quad (3.34)$$

When \mathbb{Z}_2 wall sources are used, the local vector current J_μ at zero spatial momentum takes the form

$$J_\mu(t) = \lim_{N_{\text{hits}} \rightarrow \infty} \sum_{n=1}^{N_{\text{hits}}} \sum_{\mathbf{x}, \mathbf{y} \in \Lambda} \bar{\psi}(\mathbf{x}, t) \eta^{(n)}(\mathbf{x}, t) \gamma_\mu \eta^{(n)\dagger}(\mathbf{y}, t) \psi(\mathbf{y}, t), \quad (4.48)$$

where $\eta^{(n)}(\mathbf{x}, t)$ is a stochastic \mathbb{Z}_2 wall source at time t . Applying a $U(1)$ vector transformation to this current gives

$$\frac{\delta J_\mu(t')}{\delta \alpha(\mathbf{x}, t)} = i\delta_{t,t'} \left(V_\mu(\mathbf{x}, t') - V_\mu^\dagger(\mathbf{x}, t') \right), \quad (4.49)$$

where

$$V_\mu(\mathbf{x}, t') = \lim_{N_{\text{hits}} \rightarrow \infty} \sum_{n=1}^{N_{\text{hits}}} \sum_{\mathbf{y} \in \Lambda} \bar{\psi}(\mathbf{y}, t') \eta^{(n)}(\mathbf{y}, t') \gamma_\mu \eta^{(n)\dagger}(\mathbf{x}, t') \psi(\mathbf{x}, t'). \quad (4.50)$$

Note that in the large hit limit, where $\eta^{(n)}(\mathbf{y}, t') \eta^{(n)\dagger}(\mathbf{x}, t') \rightarrow \delta_{\mathbf{x}\mathbf{y}}$, we recover the point source case and the functional derivative of $J_\mu(t)$ vanishes. Substituting Equation (4.49) into Equation (4.45) gives

$$\Delta_\mu^* \langle \mathcal{J}_\mu(x) J_\nu(t) \rangle = -\frac{\delta_{t,t'}}{a^4} \left(\langle V_\nu(\mathbf{x}, t') \rangle - \langle V_\nu^\dagger(\mathbf{x}, t') \rangle \right). \quad (4.51)$$

It is therefore apparent that a contact term will appear in the vector Ward identity when \mathbb{Z}_2 wall sources are used to compute this vector meson two-point function away from the large hit limit. This is true even when a conserved current is used at the sink. This contact term must be handled appropriately to avoid the quadratic divergence it introduces. I will discuss the strategy we adopt to avoid such issues in the next chapter when I discuss the HVP on the lattice.

4.4 Domain Wall Fermions

In this section I will describe the domain wall formulation of fermions on the lattice. This formulation manages to preserve chiral symmetry whilst also mitigating the doublers that plague naïve lattice fermions. Although chiral symmetry does not provide any computational advantage when computing the HVP, domain wall fermions are $\mathcal{O}(a)$ improved, which reduces cut-off effects in computed observables.

4.4.1 Chiral Symmetry on the Lattice

In Section 4.1.4 I discussed the Wilson Dirac operator and how the Wilson term, inserted to remove lattice doublers, explicitly breaks chiral symmetry, since it does not satisfy $\{\gamma_5, D\} = 0$. The natural question that arises from this result is whether there exists a Dirac operator on the lattice that does not produce doublers but at the same time preserves chiral symmetry as defined by its anti-commutation with γ_5 . Unfortunately, a no-go theorem proposed by Nielsen and Ninomiya dictates that no such operator exists for a local theory with an even number of dimensions [116]. However, by inserting

irrelevant operators into the chirality condition $\{\gamma_5, D\} = 0$, it is possible to circumvent this theorem.

Rather than use the continuum condition for chiral symmetry it is possible to use renormalisation group transformations to derive a condition for chiral symmetry on the lattice, namely the Ginsparg–Wilson equation [136]:

$$\gamma_5 D + D \gamma_5 = 2a D \gamma_5 D, \quad (4.52)$$

where D is a general lattice Dirac operator. It is apparent that in the continuum limit this relationship reduces to that of the continuum. Chiral rotations are now defined by [137]:

$$\psi \rightarrow \psi' = \exp\left(i\alpha\gamma_5\left(1 - \frac{a}{2}D\right)\right)\psi, \quad \bar{\psi} \rightarrow \bar{\psi}' = \bar{\psi} \exp\left(i\alpha\left(1 - \frac{a}{2}D\right)\gamma_5\right), \quad (4.53)$$

where α is the parameter specifying the rotation. Note that the continuum transformations are also obtained as $a \rightarrow 0$. It is important to stress that the Ginsparg–Wilson equation is not the condition of chirality used in the Nielsen–Ninomiya equation. It is therefore possible in principle to define a chiral, doubler-free Dirac operator that satisfies this non-linear equation.

The overlap action is one possible solution to the Ginsparg–Wilson equation, given by [138–140]

$$D = \frac{1}{a} (1 + \gamma_5 \epsilon(\gamma_5 A)), \quad (4.54)$$

where A is a suitable *kernel* and ϵ is the sign function. Typically the choice $A = D_W$ is made. The sign function applied to some matrix M is computed as

$$\epsilon(M) = \frac{M}{\sqrt{M^\dagger M}}. \quad (4.55)$$

Although the overlap Dirac operator is chirally symmetric, computing the sign function of the matrix $\gamma_5 A$ is computationally expensive. Instead we can seek to approximate the sign function using a rational function, such that chiral symmetry is minimally broken [141].

4.4.2 Continuum

Before describing the lattice formulation of domain wall fermions (DWFs), I will spend some time motivating them in the continuum theory. I will then discuss how they are discretised on the lattice, including some discussion of the different kernels that may be used.

Domain wall fermions are constructed through the introduction of a fifth dimension that is used to separate states of opposite chirality. This is achieved through the introduction

of a domain wall in the fifth dimension. Chiral states remain exponentially localised at the wall, resulting in chiral symmetry within the four-dimensional theory located at the wall.

In the continuum, the five-dimensional Dirac operator may be written [141]

$$D_{\text{DWF}}^5 = \not{D} + \gamma_5 \partial_s + M_5(s), \quad (4.56)$$

where ∂_s is the derivative in the new fifth dimension, \not{D} is the covariant Dirac operator in four dimensions and $M_5(s)$ is a potential function with monotonic asymptotic behaviour such that $M_5(s) \rightarrow \pm M_5^\pm$ as $s \rightarrow \pm\infty$, with $M_5^\pm > 0$. This operator obeys the five-dimensional Dirac equation

$$[\not{D} + \gamma_5 \partial_s + M_5(s)]\Phi(x, s) = 0, \quad (4.57)$$

where Φ is a five-dimensional four-component spinor field defined at the four-dimensional lattice site x and the fifth-dimensional coordinate s . Equation (4.57) is separable by writing Φ as

$$\Phi(x, s) = \sum_{n=0}^{\infty} [a_n(s)P_+ + b_n(s)P_-]\phi_n(x) \quad (4.58)$$

where Φ has been rewritten in terms of four-dimensional energy eigenfunctions $\phi_n(x)$. The functions $a_n(s)$ and $b_n(s)$ are functions of s that determine the behaviour of the positive and negative chiral states, and $P_\pm = \frac{1}{2}(1 \pm \gamma_5)$ are the usual chiral projection operators. Using this factorisation and the chiral projection operators gives the following coupled differential equations:

$$[\partial_s + M_5(s)]a_n(s) = m_n b_n(s), \quad (4.59)$$

$$[-\partial_s + M_5(s)]b_n(s) = m_n a_n(s), \quad (4.60)$$

along with the four-dimensional covariant Dirac equation $(\not{D} + m_n)\phi_n(x) = 0$. The solutions of this equation produce a spectrum of masses m_n , with $|m_n| \gtrsim \mathcal{O}(M_5)$ for $n > 0$ and the ground state $m_0 = 0$. This last case has a solution of the form

$$a_0(s) = N \exp\left(-\int_0^s M_5(s') ds'\right), \quad (4.61)$$

where N is a normalisation factor arising from the integration. Setting $M_5(s)$ equal to a step function gives the solution $a_0(s) = Ne^{-M_5|s|}$. This solution also produces $b_0(s) = Ne^{M_5|s|}$, which is not normalisable and so cannot be considered as physical. The ground state is therefore massless, of definite chirality and exponentially localised at the location of the domain wall at $s = 0$. Furthermore, the gap in the spectrum of m_n means that at low energies only the massless fermion of positive chirality is accessible. The massive modes with $|m_n| \gtrsim \mathcal{O}(M_5)$ propagate freely in the fifth dimension. However,

provided that M_5 is sufficiently large compared to the energy scale of interest, these massive modes should not be a cause for concern.

Translating this formulation to a finite volume with periodic boundary conditions results in some interesting behaviour. Given a finite fifth dimension with extent L_s , the potential $M_5(s)$ must now necessarily contain two defects, which we can define as being located at $s = 0$ and $s = L_s/2$. This produces the two solutions

$$a_0(s) = N \exp\left(-\int_{-L_s/2}^s M_5(s') ds'\right), \quad b_0(s) = N \exp\left(\int_{-L_s/2}^s M_5(s') ds'\right), \quad (4.62)$$

which are both normalisable due to the finite extent of the fifth dimension. We therefore now have both left- and right-handed chiral modes exponentially localised at $s = 0$ and $s = L_s/2$, respectively. These modes will mix and couple to each other at the centre of the fifth dimension, producing a degree of residual chiral symmetry breaking dependent on both the value of L_s and the height of the domain wall. This produces an additive mass renormalisation known as the residual mass, m_{res} . In the limit $L_s \rightarrow \infty$ chiral symmetry is completely restored and $m_{\text{res}} \rightarrow 0$.

4.4.3 Discretisation

To simulate DWFs on the lattice the new fifth dimension must be discretised along with the other four dimensions. The resulting theory shares many features with the continuum finite-volume DWF formulation I discussed briefly at the end Section 4.4.2. In particular there is some residual chiral symmetry breaking due to the exponentially localised left- and right-handed chiral modes mixing in the centre of the fifth dimension. In the limit $L_s \rightarrow \infty$ this mixing is removed and chiral symmetry becomes exact.

The five-dimensional domain wall action on the lattice is given by [9, 142]

$$S_F^5 = \bar{\Psi} D_{\text{DWF}}^5 \Psi, \quad (4.63)$$

where Ψ is a five-dimensional fermion and the operator D_{DWF}^5 is defined in the fifth dimension by the matrix

$$D_{\text{DWF}}^5 = \begin{pmatrix} \tilde{D} & -P_- & 0 & \cdots & 0 & mP_+ \\ -P_+ & \ddots & \ddots & \ddots & \cdots & 0 \\ 0 & \ddots & \ddots & \ddots & \ddots & \vdots \\ \vdots & \ddots & \ddots & \ddots & \ddots & 0 \\ 0 & \cdots & \ddots & \ddots & \ddots & -P_- \\ mP_- & 0 & \cdots & 0 & -P_+ & \tilde{D} \end{pmatrix}, \quad (4.64)$$

where

$$\tilde{D} = (D_-)^{-1} D_+, \quad D_+ = (1 + bD_W), \quad D_- = (1 - cD_W), \quad (4.65)$$

b and c are adjustable parameters that define the nature of the action and D_W is the Wilson Dirac operator as defined in Equation (4.24) with a negative mass parameter $-M_5$. M_5 must satisfy $0 < M_5 < 2$ in order to avoid lattice doublers in the free theory, and its exact value determines the behaviour of the fermions in the fifth dimension. In the free theory the case of $M_5 < 1$ produces fermion states that exponentially decay in a monotonic fashion in the fifth dimension, whilst $M_5 > 1$ produces states that can oscillate whilst decaying. There are various possible choices for b and c . Setting $b = 1$ and $c = 0$ produces the Shamir DWF formulation first proposed in [143], whilst setting $b - c = 1$ and $b + c = \alpha$ produces the Möbius DWF (MDWF) formulation first proposed in [144] and further described in [145, 146]. This latter case exhibits similar properties to the Shamir formulation but with the extent of the fifth dimension scaled by a factor of α . This scaling of the effective fifth dimension allows simulations to be performed closer to the limit of $L_s \rightarrow \infty$.

Although the fermion Ψ is five-dimensional, the gauge field is not. Instead, the same four-dimensional gauge field is used on every slice in the fifth dimension, with $U_5(x, s) = 1$. The four-dimensional quark fields are related to those in the fifth dimension using the projection operators P_{\pm} :

$$\begin{aligned} \psi_R &= P_+ \Psi_{L_s-1} & \psi_L &= P_- \Psi_0, \\ \bar{\psi}_R &= \bar{\Psi}_{L_s-1} P_- & \bar{\psi}_L &= \bar{\Psi}_0 P_+. \end{aligned} \quad (4.66)$$

where ψ are the four-dimensional quark fields and the L and R subscripts denote whether the quarks are left- or right-handed.

The DWF formalism has an additive mass renormalisation associated with the mixing of left- and right-handed chiral states in the middle of the finite fifth dimension. This is known as the residual mass, and is derived from the axial Ward identity [147]

$$\Delta_{\mu}^* \mathcal{A}_{\mu}(x) = 2mP(x) + 2J_{5q}(x), \quad (4.67)$$

where $\mathcal{A}_{\mu}(x)$ is the conserved axial vector current, which is defined for MDWF in [9]. $P(x) = \bar{\psi}(x)\gamma_5\psi(x)$ is the pseudoscalar operator and $J_{5q}(x)$ is a point-split current acting across the centre of the fifth dimension, defined by

$$J_{5q}(x) = -\bar{\Psi}(x, L_s/2 - 1)P_L\Psi(x, L_s/2) + \bar{\Psi}(x, L_s/2)P_R\Psi(x, L_s/2 - 1). \quad (4.68)$$

Comparing Equation (4.67) to its form in the continuum, we should expect the right-hand side to be equal to an effective quark mass multiplied by the pseudoscalar operator P . One can therefore reason that close to the continuum limit $J_{5q}(x) \approx m_{\text{res}}P(x)$ [148].

The additional $J_{5q}(x)$ term therefore defines the extent to which DWFs break chiral symmetry through the residual mass m_{res} . In practice m_{res} can be extracted from the plateau of the function

$$R(t) = \frac{\sum_{\mathbf{x}} \langle J_{5q}(\mathbf{x}, t) P(\mathbf{0}, 0) \rangle}{\sum_{\mathbf{x}} \langle P(\mathbf{x}, t) P(\mathbf{0}, 0) \rangle}, \quad (4.69)$$

such that the residual mass m_{res} is obtained by fitting a constant to this data.

The DWF formulation is related to the four-dimensional overlap formulation via a Schur decomposition, which I describe in more detail in Appendix D. To make contact with the four-dimensional theory it is necessary to introduce pseudofermion Pauli–Villars fields Φ and $\bar{\Phi}$ to remove the heavy degrees of freedom with eigenvalues $\lambda_n \gtrsim \mathcal{O}(M_5)$ that propagate in the fifth dimension [149, 150]. These pseudofermions obey Bose–Einstein statistics rather than Fermi–Dirac statistics. Including these fields in the five-dimensional path integral gives

$$\langle O \rangle_5 = \int \mathcal{D}[\bar{\Psi}, \Psi, \bar{\Phi}, \Phi, U] O e^{-S[\bar{\Psi}, \Psi, \bar{\Phi}, \Phi, U]}, \quad (4.70)$$

where the action can be written as

$$S[\bar{\Psi}, \Psi, \bar{\Phi}, \Phi, U] = S_G[U] + \bar{\Psi} D_{\text{DWF}}^5 \Psi + \bar{\Phi} D_{\text{PV}}^5 \Phi. \quad (4.71)$$

The operator D_{PV}^5 is defined similarly to D_{DWF}^5 in that the four-dimensional operator is the same, though there is some freedom in how the kinetic term in the fifth dimension is specified. From a numerical standpoint it is convenient to define $D_{\text{PV}}^5 \equiv D_{\text{DWF}}^5(m=1)$ [151]. Having defined the Pauli–Villars operator, it is now possible to write the effective overlap operator as

$$D_{\text{ov}} = \frac{1+m}{2} + \frac{1-m}{2} \gamma_5 \frac{(1+H_M)^{L_s} - (1-H_M)^{L_s}}{(1+H_M)^{L_s} + (1-H_M)^{L_s}}. \quad (4.72)$$

Domain wall fermions therefore approximate the sign function in the overlap operator as

$$\epsilon(H_M) \approx \epsilon_{L_s}(H_M) = \frac{(1+H_M)^{L_s} - (1-H_M)^{L_s}}{(1+H_M)^{L_s} + (1-H_M)^{L_s}} = \tanh(L_s \tanh^{-1} H_M). \quad (4.73)$$

In the limit $L_s \rightarrow \infty$ this approximation becomes exact, and exact chiral symmetry is restored.

Chapter 5

Lattice Computation of $a_\mu^{(2)\text{had},s}$

In this chapter I describe the computation of the leading order strange quark-connected contribution to the anomalous magnetic moment of the muon, denoted $a_\mu^{(2)\text{had},s}$. As I discussed in Section 4.2.2, performing an analysis on each Wick contraction of the QCD vector two-point function in isolation is an entirely legitimate process. This motivates the splitting of $a_\mu^{(2)\text{had}}$ into its various contributions such that we can compute the strange quark-connected contribution alone.

A computation of $a_\mu^{(2)\text{had},s}$ requires the evaluation of the Euclidean integral in Equation (3.54). I begin this chapter by discussing the HVP on the lattice in Section 5.1, explaining and investigating the techniques in this work used to determine the HVP form factor using lattice data. In Sections 5.2 and 5.3 I discuss the hybrid method and sine cardinal interpolation, respectively, two techniques I use to evaluate the aforementioned Euclidean integral and compute $a_\mu^{(2)\text{had},s}$. I then detail the extrapolations I perform to produce a final value of $a_\mu^{(2)\text{had},s}$ in Section 5.4. In Section 5.5 I discuss the techniques I use to propagate the statistical error on observables that I use in this calculation. I then explain the computation of the systematic error on $a_\mu^{(2)\text{had},s}$ in Section 5.6. I conclude with a presentation of my final results in Section 5.7.

5.1 The Hadronic Vacuum Polarisation in Lattice QCD

As I explained in Section 3.4, the Euclidean integral for computing $a_\mu^{(2)\text{had}}$,

$$a_\mu^{(2)\text{had}} = 4\alpha^2 \int_0^\infty dQ^2 f(Q^2) \times \hat{\Pi}(Q^2), \quad (3.54)$$

dictates that before $a_\mu^{(2)\text{had}}$ can be computed, one must first compute the HVP form factor $\Pi(Q^2)$. Specifically, I am interested in computing $a_\mu^{(2)\text{had},s}$, so the HVP must be computed from the strange vector two-point function. Since the discussion in what

follows is restricted entirely to the case of the strange HVP, I do not use any notation to indicate this restriction. I do however use notation to distinguish between the various contributions to $a_\mu^{(2)\text{had}}$, since I will have need to refer to the other contributions in what follows.

5.1.1 HVP Computation

In this work the strange quark-connected contribution to the electromagnetic current two-point function is computed in position space as

$$C_{\mu\nu}(x) = \frac{Z_V}{9} \langle \mathcal{J}_\mu^s(x) J_\nu^s(0) \rangle, \quad (5.1)$$

where I have explicitly inserted the strange quark charge and the conserved current \mathcal{J}_μ is motivated by the vector Ward identity as described in Section 4.3. The vector renormalisation constant Z_V is required to renormalise the local current J_ν so that contact can be made between the lattice and continuum HVPs, which both require renormalisation due to ultraviolet divergences. As such Z_V is a finite renormalisation constant, with the limiting behaviour $Z_V \rightarrow 1$ as $\beta \rightarrow \infty$ and the continuum limit is approached. There are various ways to compute Z_V , each of which has different behaviour as the lattice cut-off is varied. I discuss this in more detail below. From Equation (5.1) I compute the momentum-space HVP as

$$\Pi_{\mu\nu}(Q) = a^4 \sum_{x \in \Lambda} e^{-iQ \cdot x} C_{\mu\nu}(x) - a^4 \sum_{x \in \Lambda} C_{\mu\nu}(x), \quad (5.2)$$

where the second term corresponds to a zero-mode subtraction (ZMS). In the infinite volume limit the zero-mode vanishes via Lorentz symmetry, but the finite volume of lattice QCD means that this quantity is non-zero [152, 153]. The ZMS is included in the Fourier transform as it greatly reduces the statistical uncertainty in $\Pi(Q^2)$ at low- Q^2 , as I will discuss further in Section 5.1.2. On the lattice the tensor decomposition of the HVP is more complicated, since rotational symmetry is explicitly broken to the finite hypercubic group through the discretisation of spacetime. The lattice version of the tensor decomposition is then given by

$$\Pi_{\mu\nu}(Q) = (\delta_{\mu\nu} Q^2 - Q_\mu Q_\nu) \Pi(Q^2) + \dots, \quad (5.3)$$

where the ellipsis denotes terms invariant under hypercubic transformations. These terms are either of the form $\sum_\mu Q_\mu^n$ for an even integer n or $Q_\mu^m Q_\nu^n$ for odd integers m and n [152, 154]. In the continuum limit these contributions vanish. When a finite volume is imposed with anisotropic extents, for example when $L \neq T$, hypercubic invariance is further broken and $\Pi_{\mu\nu}(Q)$ becomes sensitive to this anisotropy. In this work I consider only momenta where $Q_\mu = 0$ [76], thus avoiding the terms proportional to $Q_\mu^m Q_\nu^n$ that are dependent on the orientation of the momentum Q [152].

In Section 4.3 I described the contact term that appears at the source timeslice when stochastic \mathbb{Z}_2 wall sources are used to compute the conserved-local vector two-point function. Although this contact term will vanish in the large hit limit, it is possible that this limit is not achieved if the number of measurements that are performed is small. The contact term must therefore be handled appropriately to avoid the quadratic UV divergence that it relates to. In the continuum theory a transverse projector $P_{\mu\nu}$ may be used to project out the transverse, divergence-free component of a tensor $T^{\mu\nu}$. In momentum space this projection acts as

$$(T^\perp)_\mu{}^\nu = P_{\mu\rho} T^{\rho\nu} = \left(g_{\mu\rho} - \frac{q_\mu q_\rho}{q^2} \right) T^{\rho\nu}, \quad (5.4)$$

where \perp denotes the transverse part of the tensor $T^{\mu\nu}$. From the definition of this projector it is clear that $q^\mu P_{\mu\nu} = 0$. On the lattice the transverse projector, which I derive in Appendix E, may be written as

$$P_{\mu\nu} = \delta_{\mu\nu} - e^{iaQ_\mu/2} e^{-iaQ_\nu/2} \frac{\hat{Q}_\mu \hat{Q}_\nu}{\hat{Q}^2}, \quad (5.5)$$

where $\hat{Q}_\mu = \frac{2}{a} \sin(aQ_\mu/2)$ and the exponentials arise from the discrete nature of lattice derivatives. Applying this projector to the HVP gives the purely transverse component of the HVP

$$\Pi_{\mu\nu}^\perp(Q) = \sum_\rho \left(\delta_{\mu\rho} - e^{iaQ_\mu/2} e^{-iaQ_\rho/2} \frac{\hat{Q}_\mu \hat{Q}_\rho}{\hat{Q}^2} \right) \Pi_{\rho\nu}(Q). \quad (5.6)$$

It is therefore apparent that if the analysis is restricted to the diagonal of the HVP tensor, such that $\rho = \nu$, and only momenta where $Q_\rho = 0$ are considered, any possible longitudinal contributions to the HVP can be avoided.

Using the lattice form of the tensor decomposition of the HVP, we can express the HVP form factor as a function of the tensor by dividing through by Q^2 and averaging over equivalent momenta. In this work I restrict the analysis to zero spatial momentum, since, as I will discuss below, I use \mathbb{Z}_2 wall sources to compute $\Pi(Q^2)$, which in this case project $C_{\mu\nu}$ to zero spatial momenta. With this momentum constraint and the restrictions on the tensor decomposition described above, I compute the HVP form factor as

$$\Pi(\hat{Q}^2) = \frac{1}{3} \sum_i \frac{\Pi_{ii}(\hat{Q})}{\hat{Q}^2}, \quad (5.7)$$

where the index i runs over spatial indices only. Note that in this work I compute Π as a function of the lattice momentum \hat{Q} , the square of which is the dual of the lattice Laplacian $\sum_\mu \Delta_\mu^* \Delta_\mu$ (see Appendix E). As I demonstrate further below, this reduces the cut-off dependence in $a_\mu^{(2)\text{had},s}$ under certain circumstances.

	48I	64I
$L^3 \times T/a^4$	$48^3 \times 96$	$64^3 \times 128$
L_s	24	12
β	2.13	2.25
am_l	0.00078	0.000678
am_s	0.0362	0.02661
α	2.0	2.0
a^{-1} / GeV	1.730(4)	2.359(7)
L/fm	5.47(1)	5.35(2)
$m_\pi L$	3.863(6)	3.778(8)
$m_K L$	13.85(5)	13.77(6)
am_s^{phys}	0.03580(16)	0.02539(17)
m_π / MeV	139.2(4)	139.2(5)
m_K / MeV	499.0(1.2)	507.6(1.6)
Z_V	0.71076(25)	0.74293(14)
Z_m	1.32(1)	1.37(1)

Table 5.1: Properties of the ensembles used in this study [9].

5.1.2 Ensembles and Measurements

I used two ensembles generated by RBC/UKQCD [9] with 2+1 dynamical flavours of MDWFs (see Section 4.4). Both ensembles produce physical pion masses and were generated using a Möbius scale α of 2 and the Iwasaki gauge action. The properties of these ensembles are listed in Table 5.1. The inverse lattice spacing and quark masses listed here were constrained using experimental data, specifically the masses of the pion, kaon and omega baryon were used. As a result, these quantities cannot be predicted using these ensembles. The values quoted in Table 5.1 were computed in [9] as part of a *global fit*, so-called because the intention of the fit was to simultaneously determine a range of SM parameters using data from eighteen different ensembles with various lattice spacings, volumes and sea quark masses. In principle the determination of $a_\mu^{(2)\text{had},s}$ could have been included in this global fit, with the advantage being that it would be possible to account for the correlations between $a_\mu^{(2)\text{had},s}$ and the variables required in its computation. However, this would require a fit ansatz to be devised to describe the dependence of $a_\mu^{(2)\text{had},s}$ on the lattice spacings, quark masses and lattice volumes of the various ensembles. The global fit of [9] used chiral perturbation theory as a guide to select the various ansätze to perform the necessary continuum, infinite volume and physical quark mass extrapolations. Such an approach cannot be applied in this case, however, since the HVP is associated with vector states, not pseudoscalars. There is no other obvious, well-motivated ansatz that can describe the dependence of $a_\mu^{(2)\text{had},s}$ on the quark masses and lattice spacings and volumes. Although it may be possible to perform the fit with an ansatz that is not motivated by physics, one is then left with the task of determining the level of systematic uncertainty arising from using a particular ansatz. On this basis the decision was made to not perform a second global fit. Instead,

the errors on the variables required in this analysis were either propagated as described in Sections 5.4 and 5.5 or were assumed to have a sufficiently negligible effect on the total value of $a_\mu^{(2)\text{had},s}$ that they could be ignored.

It is important to note that the kaon masses computed with unitary strange quarks on the two ensembles in Table 5.1 deviate from 495.7 MeV, the mass taken as the target physical value when generating these ensembles [9]. This is indicative of the mistuning of the bare lattice strange quark masses, which deviate by approximately 1% and 5% on the 48I and 64I ensembles, respectively (see Table 5.1). In Table 5.1 I also give the value of the quark mass renormalisation constant Z_m and the vector renormalisation constant Z_V . The former is required to compute the strange quark mass in $\overline{\text{MS}}$, which, as I discuss in Section 5.2.4, is needed when computing the contribution to $a_\mu^{(2)\text{had},s}$ from the large Q^2 region of the integral in Equation (3.54). The latter is required to renormalise the local vector current J_μ used in the computation of the HVP tensor.

The value of Z_V can be computed from lattice matrix elements, possibly in combination with the vector Ward identity. The value stated in Table 5.1 was computed using the ratio of pion two- and three-point functions [9]. It is also possible to use a value of Z_V computed using a ratio of kaon two- and three-point functions, and this will differ from the determination using pions through mass-dependent cut-off effects [13]. However, universality requires that both of these computations agree in the continuum limit, so the choice of Z_V will not affect the value of $a_\mu^{(2)\text{had},s}$ once a continuum extrapolation has been performed.

The HVP correlator as defined in Equation (5.2) was computed by inverting the MDWF Dirac operator on both point and stochastic \mathbb{Z}_2 wall sources. Because of the computational cost of using the MDWF action when generating the two ensembles in Table 5.1, each has a limited number of configurations (the 48I ensemble has 88 configurations whilst the 64I ensemble has 80). To improve the statistical accuracy of the final result we therefore made use of translation invariance and performed inversions on several of the timeslices in each configuration. When selecting the number of sources used on each configuration, a balance was struck between achieving sufficient statistical accuracy and a reasonable simulation time, since additional sources require additional inversions of the Dirac operator. A summary of the measurements used in this work is given in Table 5.2. The table reflects the incremental nature of the way in which the measurements were made. Initially, a set of measurements using unitary strange quark masses was planned as part of a larger run designed to study a broader range of SM processes. This allowed the strange quark propagators, which were not saved for later reuse, to be used in the computation of several n -point functions, thus improving the efficiency of the computation. The partially quenched measurements were performed at a later date to account for the possible sensitivity of $a_\mu^{(2)\text{had},s}$ to the value of the strange quark mass.

Ensemble	Source Type	am_s	Propagators per Configuration	Number of Configurations
48I	\mathbb{Z}_2 Wall	0.0362	48	88
48I	\mathbb{Z}_2 Wall	0.0358	96	22
64I	\mathbb{Z}_2 Wall	0.02661	32	80
64I	\mathbb{Z}_2 Wall	0.02539	128	20
48I	Point	0.0362	12	88
64I	Point	0.02661	8	80

Table 5.2: Summary of measurements performed in this study. Propagators on a single configuration use sources on different timeslices evenly spaced along the temporal extent, starting at $t = 0$.

Figure 5.1 shows the HVPs resulting from the two sets of unitary measurements in Table 5.2 where stochastic \mathbb{Z}_2 wall sources were used. In both cases, the HVP exhibits a high level of statistical precision and qualitatively similar behaviour to the HVPs computed in [76, 153, 155–157]. Figure 5.2 shows both the partially quenched and unitary data in the low- Q^2 region and highlights the precise nature of the data at small Q^2 . The greater degree of mistuning in am_s for the 64I ensemble is clearly discernible when comparing the data from the two ensembles at small Q^2 .

5.1.3 Source Selection

As I will explain below in Section 5.2, one of the main challenges for a lattice computation of $a_\mu^{(2)\text{had}}$ is the difficulty of computing values of $\Pi(Q^2)$ at small Q^2 with a high level of accuracy. On this basis I used the measurements in Table 5.2 to compute the relative errors

$$\delta\Pi(\hat{Q}^2) = \frac{\Delta\Pi(\hat{Q}^2)}{\Pi(\hat{Q}^2)}, \quad (5.8)$$

where $\Delta\Pi(\hat{Q}^2)$ denotes the statistical error in $\Pi(\hat{Q}^2)$. I compared this quantity for the two different source types at the lowest non-zero \hat{Q}^2 , denoted \hat{Q}_{min}^2 , both with and without ZMS. Figure 5.3 indicates the effect of using ZMS on $\delta\Pi(\hat{Q}_{\text{min}}^2)$ for both \mathbb{Z}_2 wall and point sources. In the former case ZMS improves the statistical error in the low- Q^2 region by more than an order of magnitude. Specifically, where twelve \mathbb{Z}_2 wall sources are used per configuration, with a computational cost equal to the point source case, there is a factor of 72 improvement in $\delta\Pi(\hat{Q}_{\text{min}}^2)$. This factor is reduced to 48 when four times as many inversions are performed per configuration. Importantly, both sets of \mathbb{Z}_2 wall source measurements outperform point sources when ZMS is used. This motivates the use of \mathbb{Z}_2 wall sources in combination with ZMS throughout the rest of this work.

To understand the reason why ZMS produces such a drastic reduction in $\delta\Pi(\hat{Q}_{\text{min}}^2)$ when \mathbb{Z}_2 wall sources are used I studied the covariance matrix of the correlator $C_{ii}(x)$, which

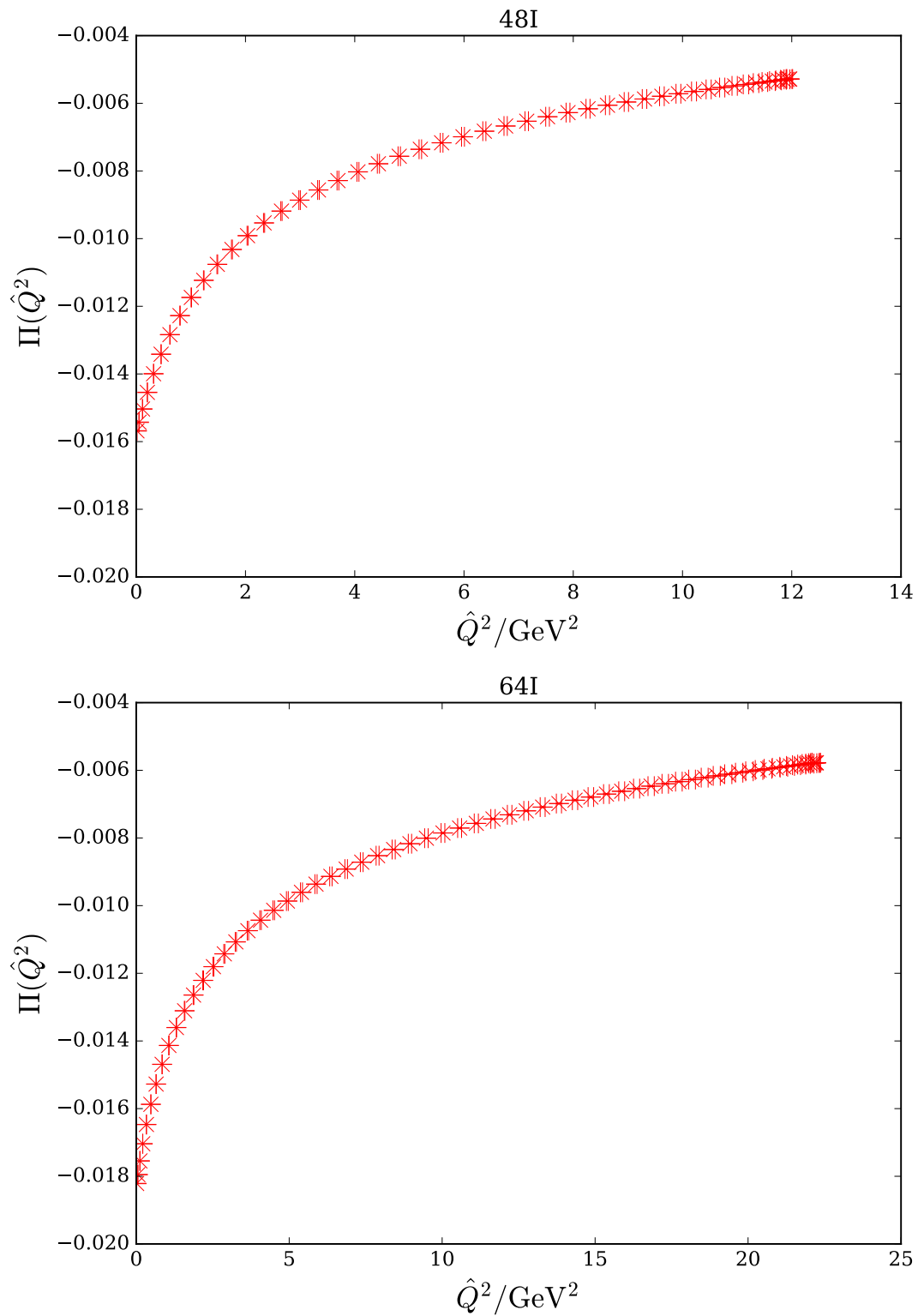


Figure 5.1: The strange quark-connected HVPs computed as a result of the two unitary measurements using \mathbb{Z}_2 wall sources described in Table 5.2. The upper plot shows data computed using the 48I ensemble, whilst the lower plot shows data for the 64I ensemble. The corresponding partially quenched HVPs are closely aligned with the unitary data, and so I do not show them here.

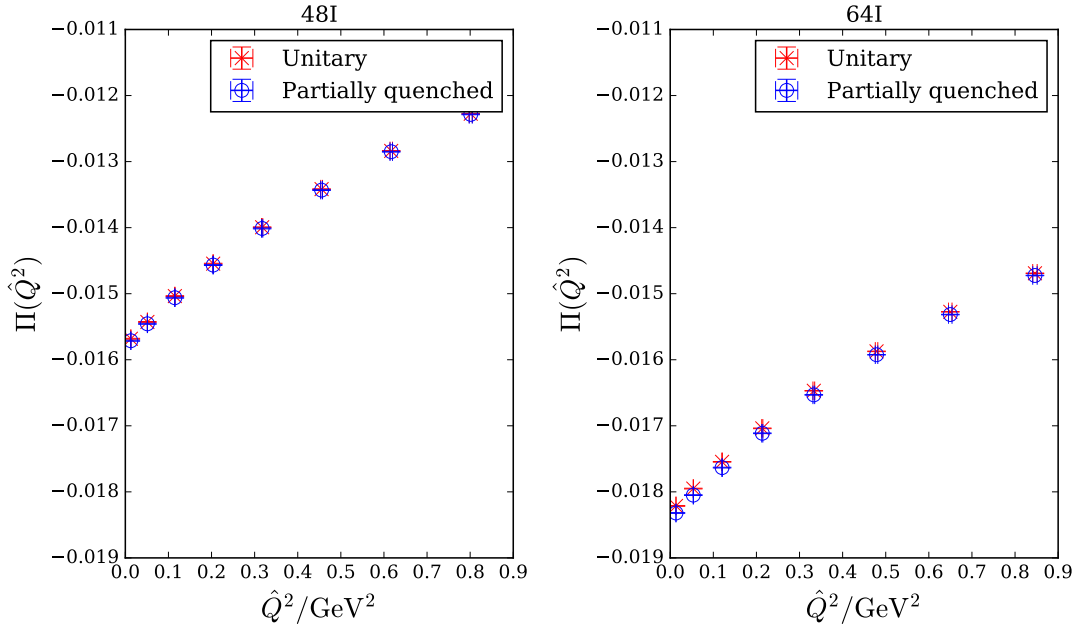


Figure 5.2: The low- Q^2 region of the strange, quark-connected HVPs shown in Figure 5.1. The left-hand plot shows data from the 48I ensemble, whilst the right-hand plot shows data from the 64I ensemble.

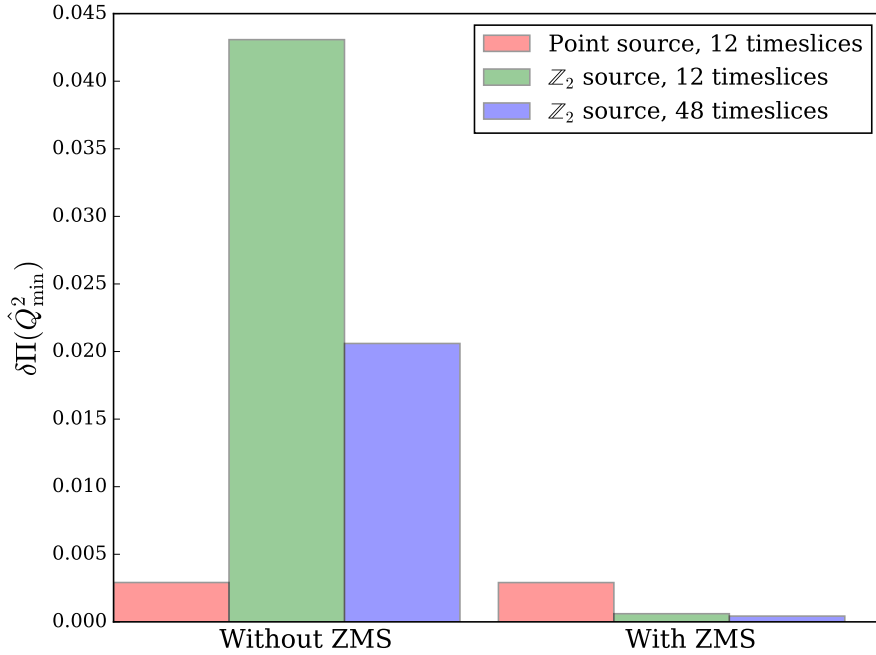


Figure 5.3: Values of $\delta\Pi(\hat{Q}_{\min}^2)$ under various analysis conditions, where $\delta\Pi$ is defined in Equation (5.8). Here \hat{Q}_{\min}^2 refers to the lowest non-zero value of \hat{Q}^2 . Note that the \mathbb{Z}_2 wall sources only provide an improvement over point sources when the ZMS procedure is used.

in general is computed for two observables X and Y as

$$\sigma^2 \equiv \text{cov}(X, Y) = \langle XY \rangle - \langle X \rangle \langle Y \rangle. \quad (5.9)$$

To incorporate the effect of ZMS into $C_{ii}(x)$ I inverse Fourier transformed the HVP tensor computed using ZMS as specified in Equation (5.2), introducing

$$C_{ii}^{\text{ZMS}}(x) = \frac{1}{a^4} \sum_{Q \in \bar{\Lambda}} e^{iQ \cdot x} \Pi_{ii}(Q). \quad (5.10)$$

I illustrate the first five rows and columns of the covariance matrix σ^2 of both C_{11} and C_{11}^{ZMS} in Figure 5.4 using both point and \mathbb{Z}_2 wall sources¹. Where point sources are used in panel (a) there is a strong anti-correlation between the first and second timeslices of the correlator C_{11} . In panel (b), where \mathbb{Z}_2 wall sources are used without ZMS, this anti-correlation is absent. Comparing the left- and right-hand plots of panel (a), there is no noticeable change in the covariance matrix arising from the use of ZMS along with point sources. In contrast, ZMS greatly alters the covariance matrix computed from \mathbb{Z}_2 wall source correlators (see both plots in panel (b)). Indeed, there is anti-correlation between the first and second timeslices of C_{11}^{ZMS} where in C_{11} there was none. The effect of ZMS can be explored in more detail by considering the relationship between C_{ii} and C_{ii}^{ZMS} , which can be computed by evaluating the aforementioned Fourier transforms to give

$$C_{ii}^{\text{ZMS}}(x) = C_{ii}(x) - \delta_{x,0} \sum_y C_{ii}(y). \quad (5.11)$$

This indicates that $C_{ii}^{\text{ZMS}}(0)$ receives contributions from the entire lattice volume. I show histograms of the values of $\sum_x C_{11}(x)$ as computed using both \mathbb{Z}_2 wall and point sources in Figure 5.5. From this figure it is apparent that the volume sum of $C_{ii}(x)$ in the point source case exhibits far less variation than in the \mathbb{Z}_2 wall source case. In addition, the values in the point source case all lie close to zero. Although this is not apparent from the figure, each of the 2000 bootstrap samples of $\sum_x C_{11}(x)$ has a magnitude of less than 4×10^{-7} . The small magnitude of this volume sum is therefore the main reason that the correlators produced by point sources are not noticeably affected by ZMS.

This evidence suggests that the spatial volume average performed by \mathbb{Z}_2 wall sources achieves mixing between sites within the wall sufficient to destroy the complex structure of correlations that would otherwise manifest if point sources were used. Accounting for these correlations is essential in reducing the relative error in $\Pi(Q^2)$ at small Q^2 . ZMS restores some of these suppressed correlations through the use of the sum of the correlator over the entire lattice volume.

¹Although I only show plots and results for the case where $i = 1$, I also observed similar behaviour in the $i = 2, 3$ cases.

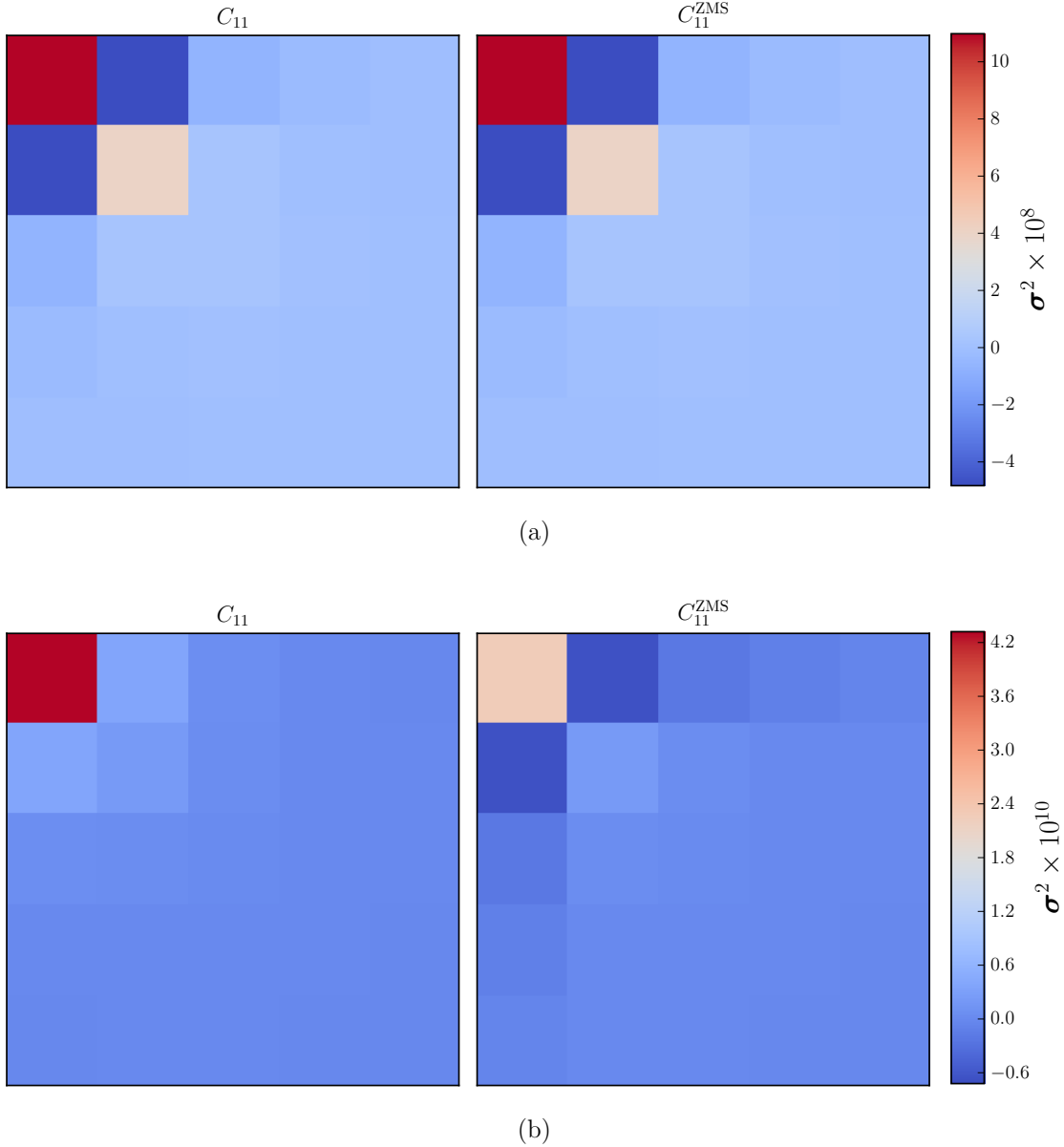


Figure 5.4: The first five rows and columns of the covariance matrix of $C_{11}(t, \mathbf{Q} = \mathbf{0})$ (left) and $C_{11}^{\text{ZMS}}(t, \mathbf{Q} = \mathbf{0})$ (right), for both point sources (panel (a)) and \mathbb{Z}_2 wall sources (panel (b)). $C_{11}(t, \mathbf{Q} = \mathbf{0})$ is the original position-space two-point function defined in Equation (5.1), projected to zero spatial momentum with $\mu = \nu = 1$. $C_{11}^{\text{ZMS}}(t, \mathbf{Q} = \mathbf{0})$ is the position-space representation of the HVP correlator at zero spatial momentum, computed with ZMS as defined in Equation (5.10), also with $\mu = \nu = 1$. The data shown here was computed using the unitary strange quark mass on the 48I ensemble.

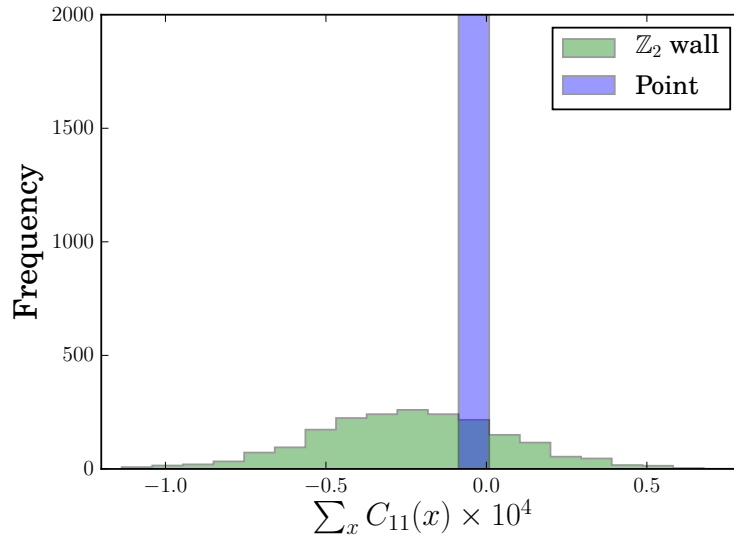


Figure 5.5: The distribution of bootstrap values of $\sum_x C_{11}(x)$ where $C_{11}(x)$ was computed using both point and \mathbb{Z}_2 wall sources. This data was computed using unitary strange quark masses on the 48I ensemble.

5.2 The Hybrid Method

The integral in Equation (3.54) does not lend itself well to an evaluation using data from lattice simulations because of the wide range of energy scales involved in the integral. As I described in Chapter 3, the integrand is highly peaked at low- Q^2 such that more than 95% of the value of the integrand lies below 0.5 GeV^2 . One therefore requires that the integrand in this region is known to a high level of accuracy down to $Q^2 \simeq 0$ to ensure that the final value of $a_\mu^{(2)\text{had}}$ is also accurate. However, the periodic boundary conditions used in the majority of lattice simulations mean that there is a limit on the smallest non-zero value of Q^2 that can be accessed. For example, the lowest non-zero value of Q^2 accessible using the ensembles described in Table 5.1 is approximately 0.013 GeV^2 , or $1.2m_\mu^2$. This contrasts with the location of the peak in the integrand, which is typically around $m_\mu^2/4$. At large Q^2 the contribution to the integral from this region is small, with the region above 5 GeV^2 contributing approximately 0.2% to the total value. However, there is still the risk of significant cut-off effects that must be properly accounted for when taking a continuum extrapolation.

Until now I have omitted twisted boundary conditions (TBCs) from the discussion of momentum accessibility. This technique involves the introduction of a *twist angle* ω_μ at each boundary of the lattice such that the fermion field ψ obeys the boundary condition $\psi(x + L_\mu) = e^{i\omega_\mu} \psi(x)$ [158]. This induces momentum in the fermion field, allowing momenta with values other than $2\pi n_\mu/L_\mu$ to be accessed. Since twisting alters the properties of the fermion field, it must be done as part of the propagator computation. This means that each separate twist requires its own solution to $D\psi = \eta$. Within lattice

simulations there are two available approaches to implementing TBCs. The first involves generating an ensemble using TBCs before computing quark propagators that are also twisted. The second involves computing twisted quark propagators on ensembles that are themselves not twisted, a technique known as partial twisting. This second option is computationally far cheaper whilst remaining theoretically valid [158]. However, multiple inversions of the Dirac operator are still required, making this technique more computationally expensive than the more common periodic boundary conditions. Although some groups have applied TBCs to the determination of the HVP and $a_\mu^{(2)\text{had}}$ [75, 152, 159], they are not pursued here.

Early approaches to a lattice computation of $a_\mu^{(2)\text{had}}$ involved partitioning the Euclidean integral into two regions separated by some cut Q_{cut}^2 [72, 73, 160]. The data below this cut was then used to determine a parametrisation or model of the HVP that could be used to compute the contribution to the total integral from this region. Above Q_{cut}^2 an analytical expression from perturbation theory was used. The two results would then be summed to obtain the final value of $a_\mu^{(2)\text{had}}$. The disadvantage of this approach is that one must select Q_{cut}^2 carefully to ensure that the perturbative result remains valid over the interval $[Q_{\text{cut}}^2, \infty)$ whilst also minimising the systematic error arising from using a model or parametrisation over a range of Q^2 . This is especially difficult to achieve when one considers that the curvature of the HVP is much greater at small Q^2 than at large Q^2 [161]. This, combined with the fact that lattice data at large Q^2 is more precise than at small Q^2 , means that fitting a model or parametrisation to $\Pi(Q^2)$ in order to extrapolate to $Q^2 = 0$ produces a value of $\Pi(0)$ that may be strongly affected by systematic uncertainty due to the location of the cut.

The hybrid method remedies these difficulties by partitioning the integral into three regions instead of two (see Figure 5.6) using cuts at low- and high- Q^2 (Q_{low}^2 and Q_{high}^2) [162, 163]. The region at low- Q^2 is computed by constraining some parametrisation or model of $\Pi(Q^2)$ using lattice data. From this the values of $\Pi(0)$ and hence $\hat{\Pi}(Q^2)$ may be computed. This result may then be combined with the QED kernel f to obtain the integrand of interest, which may then be evaluated numerically. The mid- Q^2 region is integrated directly by multiplying the lattice data by $f(Q^2)$ then using a numerical integration algorithm such as the trapezium rule. Finally, the high- Q^2 integral is computed using perturbation theory. In this work I use the three-loop expression given in [164], which is adequate for the purposes of the present computation, given that the contribution from this region is several orders of magnitude smaller than the total value of the integral. When performing the integration of the mid- Q^2 region, if either of the specified values of Q_{low}^2 and Q_{high}^2 are not directly accessible on the lattice, then a simple linear interpolation is performed to compute a value of $\hat{\Pi}(Q_{\text{low}}^2)$ or $\hat{\Pi}(Q_{\text{high}}^2)$.

The hybrid method provides a general framework for the evaluation of the Euclidean integral in Equation (3.54), but there remains much flexibility in how an analysis is implemented, with many possible variations. The most obvious of these are the values of

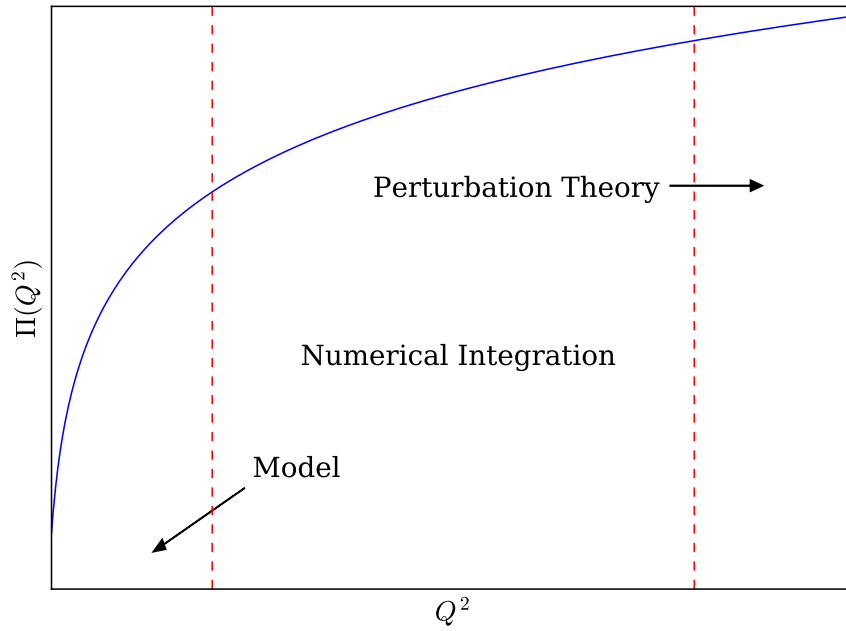


Figure 5.6: Schematic overview of the hybrid method, with a sketch of some HVP overlaid with dashed lines denoting the three regions that the integral in Equation (3.54) is partitioned into.

Q_{low}^2 and Q_{high}^2 . There is an incentive to reduce Q_{low}^2 in order to minimise the systematic error arising from the use of a parametrisation for the HVP. However, there is also an incentive to increase Q_{low}^2 to increase the amount of data available to the parametrisation, improving the statistical error on the low- Q^2 integral. I have hence performed the hybrid analysis with various Q_{low}^2 in an attempt to ascertain the effect of varying this parameter on the final result. Similarly, the value of Q_{high}^2 may be varied to determine the systematic uncertainty arising from both lattice cut-off effects and the application of the perturbation theory expression at Q_{high}^2 . However, since $a_\mu^{(2)\text{had}}$ is dominated by contributions from the low- Q^2 region, the variation of Q_{high}^2 is not expected to significantly affect the final value of $a_\mu^{(2)\text{had}}$.

In addition to the variation of Q_{low}^2 and Q_{high}^2 , there are a variety of candidates for the parametrisation or model used to compute the low- Q^2 integral. The method used to constrain these parametrisations and models may also be varied. In the following subsections I will discuss the parametrisations and matching methods I use in this work in more detail.

5.2.1 Low- Q^2 Parametrisations

I use two types of parametrisations for the low- Q^2 region of the HVP: Padé approximants and conformal polynomials. Both of these representations are founded on the

analyticity of the HVP and have been shown to converge to the HVP as the number of parameters they contain is increased [162, 165]. In this sense they can be considered model-independent. Other representations of the HVP at low- Q^2 also exist. Vector meson dominance and chiral perturbation theory both have associated representations [166–168], for example. In the former case one assumes that interactions between photons and hadronic matter are dominated by the lowest-lying vector meson states (i.e. the ρ , ω and ϕ [5]), using this assumption to construct an effective theory. In this work, I have opted to restrict the analysis to representations of the HVP that are motivated by knowledge of the form factor rather than effective field theories, thus removing a significant source of model dependence in this analysis.

The Padé approximants are motivated by the once-subtracted dispersion relation of the HVP [169], which in turn is founded on the analyticity of the form factor, i.e.

$$\Pi(Q^2) = \Pi(0) + Q^2\Phi(Q^2), \quad \Phi(Q^2) = \int_{4m_\pi^2}^{\infty} ds \frac{\rho(s)}{s(s+Q^2)}, \quad (5.12)$$

where $\rho(s) = \text{Im}\Pi(s)/\pi$ is the non-negative vector spectral function. Since the spectral function is non-negative, we can express Φ as the Stieltjes function

$$\Phi(z) = \int_0^{1/R} \frac{d\nu(\tau)}{1+\tau z}, \quad (5.13)$$

where $d\nu(\tau) = \rho(1/\tau)d\tau$, $\tau = 1/s$ and $R = 4m_\pi^2$, where m_π is the pion mass. It has been shown that Stieltjes functions can be related to Padé approximants in [170, 171]. Specifically, given a set of N points $(Q_i^2, \Phi(Q_i^2))$ for $i \in \{1, \dots, N\}$ it is possible to construct a sequence of Padé approximants that converge to $\Phi(Q^2)$ as $N \rightarrow \infty$ on any closed, bounded region of the complex plane, excluding the branch cut on the interval $(-\infty, -4m_\pi^2]$. Since we are working in the context of a finite set of lattice HVP data points, this result is highly useful. The sequence of Padés $\{\Psi_1, \dots, \Psi_N\}$ produces the continued fraction [170]

$$\Phi(Q^2) = \frac{\Phi(Q_1^2)}{1 + \frac{(Q^2 - Q_1^2)\Psi_1(Q_2^2)}{1 + \dots \frac{(Q^2 - Q_{N-1}^2)\Psi_{N-1}(Q_N^2)}{1 + (Q^2 - Q_N^2)\Psi_N(Q^2)}}}. \quad (5.14)$$

Furthermore, it has been shown in [172] that such a continued fraction, and hence the function Φ , can be written as the Padé approximant

$$R_{mn}(x) = \frac{\sum_{k=0}^m a_k x^k}{\sum_{k=0}^{n-1} b_k x^k + x^n}, \quad (5.15)$$

where a_k and b_k are coefficients to be determined. It is therefore possible, given a finite set of data points $\Phi(Q_i^2)$ and Q_i^2 that lie on the function $\Phi(Q^2)$, to construct a Padé

approximant that is exact at these points. In particular, as the number of points (and hence Padé parameters) is increased, the Padé approximant will converge uniformly to the function $\Phi(Q^2)$. Given the statistical nature of lattice QCD simulations, it is not possible to determine the exact values of the points $(Q_i^2, \Phi(Q_i^2))$. This means that it is not possible to construct such Padé approximants directly from the lattice determination of the HVP. Instead, I use the above argument to interpret a given Padé approximant as a valid functional form for the HVP before constraining it using one of the methods described in Section 5.2.2. Such an approach was proposed in [165, 169], with the authors noting that Padés are advantageous compared to the ansätze prescribed by vector meson dominance, since there are no assumptions of the underlying physics in the former case.

In this work I adopt the parametrisation suggested in [169] and approximate the HVP using the following expression for the Padé

$$R_{mn}(\hat{Q}^2) = \Pi_0 + \hat{Q}^2 \left(\sum_{k=0}^{m-1} \frac{a_k}{b_k + \hat{Q}^2} + \delta_{mn} c \right), \quad n = m, m + 1, \quad (5.16)$$

where a_k, b_k, Π_0 and c are parameters to be determined.

As I discussed in Section 3.3.1, the HVP form factor contains a branch cut on the real interval $(-\infty, -4m_\pi^2]$. The strange HVP will have an analogous branch cut specified by the two-particle mass threshold, E_{\min} . Because of this, its Taylor series is only convergent for Q^2 less than the square of the two-particle mass threshold. To overcome this limitation the complex plane can be mapped onto a unit disc using the conformal transformation

$$w = \frac{1 - \sqrt{1+z}}{1 + \sqrt{1+z}}, \quad z = \frac{\hat{Q}^2}{E^2}, \quad (5.17)$$

where E is an energy parameter with the requirement $E < E_{\min}$. This transformation maps the complex plane, excluding the real interval $(-\infty, -E^2)$, onto the interior of the unit disc, with the interval $(-\infty, -E^2)$ being mapped onto the boundary. A Taylor expansion of Π in w will then be convergent for all $Q^2 \geq 0$, provided that the parameter $E < E_{\min}$. This expansion can then be truncated at some order n to give the conformal polynomial

$$P_n^E(\hat{Q}^2) = \Pi_0 + \sum_{k=1}^n p_k w^k, \quad (5.18)$$

where p_k and Π_0 are parameters to be determined.

Both of these parametrisations have been studied extensively in [162], where they were applied within the context of the hybrid method to the light HVP. The study used a dispersive model and lattice data to generate an HVP form factor with statistical properties similar to that generated using lattice QCD. The ability of each of these parametrisations to reproduce the observed curvature in this HVP at low- Q^2 was then studied. Both of these parametrisations were capable of producing a value of $a_\mu^{(2)\text{had},l}$

with a systematic error of less than 1% where $Q_{\text{low}}^2 \lesssim 0.1 \text{ GeV}^2$. Furthermore, the low-order Padé approximants produced a similar level of systematic error for values of $Q_{\text{low}}^2 \sim 0.2 \text{ GeV}^2$ and beyond. The authors note there are circumstances where the systematic uncertainty associated with a conformal polynomial of a particular order is larger than that produced by a Padé approximant with the same number of parameters. Specifically this can occur when one applies conformal polynomials to a larger range of Q^2 values or constrains such parametrisations using a χ^2 fit (see Section 5.2.2). Within the study it is noted that the strange HVP form factor exhibits significantly less curvature than the light, so it is anticipated in the present work that the systematic error associated with a particular parametrisation and value of Q_{low}^2 will be smaller in this case. In practice this means that larger values of Q_{low}^2 should be permissible for any given parametrisation.

5.2.2 Matching at Low- Q^2

In this work I use two methods to constrain the parametrisations at low- Q^2 : a fit performed using χ^2 minimisation and discrete time moments. The latter is based on the moments method described in [82].

A χ^2 fit is performed by minimising

$$\chi^2 = \mathbf{r}^T \cdot (\boldsymbol{\sigma}^2)^{-1} \cdot \mathbf{r}, \quad \mathbf{r} = \mathbf{y} - \mathbf{f}(\mathbf{p}, \mathbf{x}), \quad (5.19)$$

where \mathbf{y} are the set of data depending on independent variables \mathbf{x} , and \mathbf{f} is a function that may approximate the relationship between \mathbf{x} and \mathbf{y} given a particular set of parameters \mathbf{p} to be determined from the fit. The object $\boldsymbol{\sigma}^2$ is the covariance matrix defined in Equation (5.9). Under the assumption that the errors on the data \mathbf{x} and \mathbf{y} follow a Gaussian distribution, the value of χ^2 can be considered as a measure of the goodness of fit of the model \mathbf{f} to the data. In computing χ^2 from Equation (5.19), data with a greater statistical precision are given more weight. In the case of the HVP this means that data at large Q^2 , where the data is more precise, have more influence over the fit parameters than data at small Q^2 .

In practice the value of χ^2 is represented as a floating point number with a finite level of numerical precision. One then uses an iterative minimisation procedure to systematically vary \mathbf{p} such that the value of χ^2 converges with some tolerance to a minimum value. Given a final χ^2 and the number of *degrees of freedom* (d.o.f.), the level of confidence in the fit parameters \mathbf{p} can be quantified by determining the p -value from the cumulative distribution function associated with the χ^2 distribution. As a general rule of thumb, if the reduced χ^2 , computed as $\chi^2/\text{d.o.f.}$, is far greater than unity, this indicates that the parameters \mathbf{p} and the function \mathbf{f} fit the data poorly. If $\chi^2/\text{d.o.f.} \approx 1$, then the function is able to fit the data up to the variance available. If $\chi^2/\text{d.o.f.} \ll 1$ then the function is “over-fitting” the data, meaning it is fitting noise rather than the signal of interest.

Interpreting the χ^2 and its associated p -value in this way is a valid procedure only when all sources of correlation have been accounted for.

It is sometimes the case that the covariance matrix may be singular at the available level of arithmetic precision such that its inverse is impossible to determine. In those cases where it is possible to determine the inverse, the fit may not converge successfully. A possible alternative in these scenarios is to compute the Moore–Penrose pseudoinverse [173,174] of the matrix and use this in the fit instead. Computing the pseudoinverse can be achieved using a singular value decomposition (SVD), whereby a matrix \mathbf{M} is decomposed as $\mathbf{M} = \mathbf{U}\mathbf{\Sigma}\mathbf{V}^\dagger$. Here \mathbf{U} and \mathbf{V} are two unitary matrices and $\mathbf{\Sigma}$ is a diagonal matrix containing the singular values of \mathbf{M} , equal to the square roots of the non-zero eigenvalues of $\mathbf{M}^\dagger\mathbf{M}$. The pseudoinverse is then constructed from these matrices in the following manner. First the pseudoinverse of $\mathbf{\Sigma}$ is computed by replacing those elements on the diagonal that are greater than some threshold ε with their reciprocals. The other diagonal elements of this matrix are left unaltered. This result is then left-multiplied by \mathbf{V} and right-multiplied by \mathbf{U}^\dagger to obtain the pseudoinverse of \mathbf{M} . This process of removing a number of singular values from the covariance matrix means that some of the correlation information is necessarily disturbed. As a result, the fidelity of the χ^2 and its associated p -value will decrease in a way that it is impossible to accommodate in a mathematically rigorous manner.

The covariance matrix computed from the strange HVP form factor was singular at the available level of numerical precision, making a fully correlated fit impossible to perform. I attempted to approximate the inverse of the covariance matrix using the pseudoinverse, using values of ε equal to 10^{-9} , 10^{-8} and 10^{-7} . The values of the χ^2 obtained from these fits indicated either the lingering presence of highly singular correlations or a complete lack of any correlation ($\chi^2/\text{d.o.f.} \approx 0$). I therefore conclude that it is not possible to approximate the inverse to the covariance matrix in a way that preserves the essential correlation information contained within it. In light of this I approximate the covariance matrix using its diagonal only, sacrificing the χ^2 and p -value as indicators of the fit quality. As I will demonstrate later when I present results of $a_\mu^{(2)\text{had},s}$, this approximation is justified at the empirical level.

Discrete time moments are based on the tensor decomposition described in Equation (5.3), which I here combine with the lattice Fourier transform of the electromagnetic two-point function to give

$$\frac{a^4}{3} \sum_{t,\mathbf{x},i} e^{-iQ_t t} C_{ii}(\mathbf{x}, t) = \hat{Q}_t^2 \Pi(\hat{Q}_t^2). \quad (5.20)$$

In [82] it is noted that this equation can be used to relate the time moments of the correlator $C_{ii}(\mathbf{x}, t)$ to an even number of continuous derivatives of the right-hand side.

Specifically, we can write

$$(-1)^n \frac{a^4}{3} \sum_{t,\mathbf{x},i} t^{2n} C_{ii}(\mathbf{x}, t) = \frac{\partial^{2n}}{\partial Q_t^{2n}} \left(\hat{Q}_t^2 \Pi(\hat{Q}_t^2) \right) \Big|_{Q_t=0}, \quad n \in \mathbb{N}. \quad (5.21)$$

Given some parametrisation of the HVP it is then possible to generate a set of equations using these moments that can then be solved to determine the parameters needed by the parametrisation. Note that although the HVP is expressed as a function of \hat{Q}_t , derivatives are taken with respect to Q_t . In contrast to a χ^2 fit, where the fit is performed over all available data in the range $[0, Q_{\text{low}}^2]$, the value of Q_{low}^2 is not a direct input in the moments method, meaning the parameters constrained using this method are independent of the value of the low cut. (This is not to say that the final value of $a_\mu^{(2)\text{had},s}$ will be independent of Q_{low}^2 , however, since the latter quantity is used to when defining the three integral regions in the hybrid method.) Furthermore, since the derivatives are evaluated at $Q_t = 0$, the moments method lends more weight to data nearest $Q^2 = 0$.

Continuous moments make the assumption that lattice momenta are continuous, meaning an infinite volume is assumed. In addition, analytical continuous derivatives are difficult to incorporate into a completely numerical framework. To address both of these issues, we can instead use discrete time moments, rewriting Equation (5.21) as

$$\hat{\Delta}_{Q_t}^{(2n)} \left(\frac{a^4}{3} \sum_{t,\mathbf{x},i} e^{-iQ_t t} C_{ii}(\mathbf{x}, t) \right) \Big|_{Q_t=0} = \hat{\Delta}_{Q_t}^{(2n)} \left(\hat{Q}_t^2 \Pi(\hat{Q}_t^2) \right) \Big|_{Q_t=0}, \quad (5.22)$$

where $\hat{\Delta}_{Q_t}$ is a general discrete derivative operator. In this particular analysis I use a central discrete derivative improved to $\mathcal{O}(h^2)$, where $h = 2\pi/T$. The generated system of equations can then be solved numerically to determine the HVP ansatz parameters.

In Section 5.1.1 I mentioned that the HVP is parametrised as a function of \hat{Q}^2 rather than Q^2 . In Figure 5.7 I demonstrate that this choice is justified empirically, comparing the a^2 scaling behaviour under the two momentum definitions. I plot $a_\mu^{(2)\text{had},s}$ against a^2 rather than a since the MDWF fermion action is $\mathcal{O}(a)$ improved. Where a χ^2 fit has been used in panel (a) there is a significant reduction in the slope when the continuum limit is taken, to the extent that the central value in the continuum limit shifts downwards by 1σ .

In Figure 5.8 I show a typical result of constraining the $R_{1,1}$ Padé. In this specific instance the parametrisation was constrained via a χ^2 fit with a low cut of 0.7 GeV^2 using unitary data from the 48I ensemble. The deviation of the parametrisation from the lattice data is negligible. I find little deviation from the behaviour shown in Figure 5.8 as the parametrisation, cuts and matching method are varied.

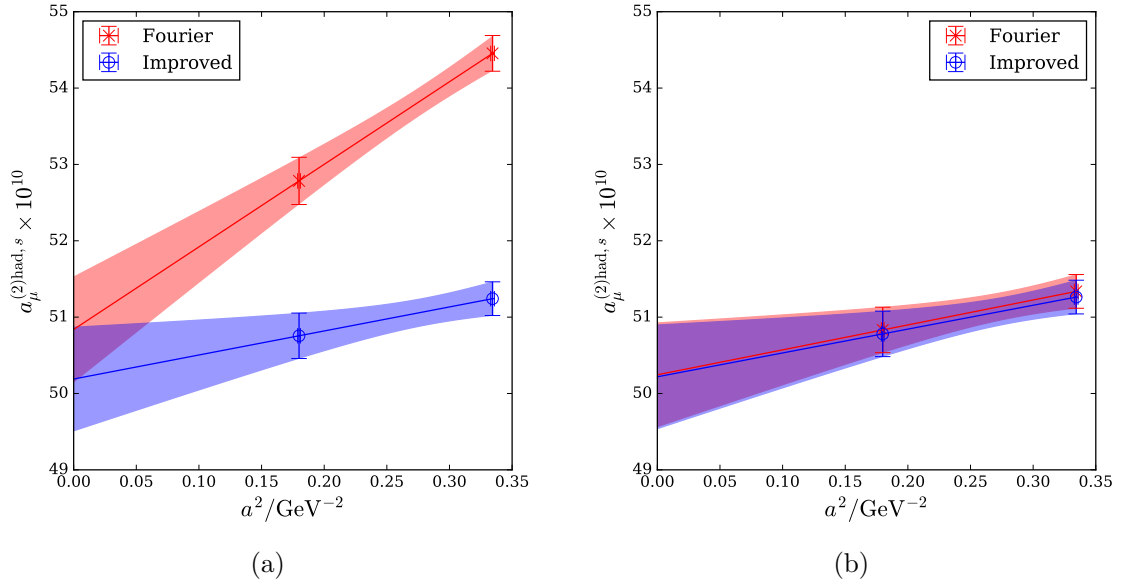


Figure 5.7: A comparison of the a^2 scaling behaviour of $a_\mu^{(2)\text{had},s}$ when the analysis is performed with either lattice Fourier momenta $Q_\mu = 2\pi n_\mu/L_\mu$ or improved momenta $\hat{Q}_\mu = \frac{2}{a} \sin(aQ_\mu/2)$. Note that in both cases the lattice Fourier transform is performed with respect to the Fourier momentum Q_μ . Panel (a) shows values of $a_\mu^{(2)\text{had},s}$ computed using a χ^2 fit and panel (b) shows values of $a_\mu^{(2)\text{had},s}$ computed using discrete moments. In both cases the HVP form factor was parametrised using an $R_{1,1}$ Padé approximant, with $Q_{\text{low}}^2 = 0.7 \text{ GeV}^2$ and $Q_{\text{high}}^2 = 5.0 \text{ GeV}^2$. Note also that I neglect the effects of the strange quark mass mistuning, presenting results here computed using only unitary strange quark masses.

5.2.3 Integrating the Low- and Mid- Q^2 Regions

As discussed earlier, the integrand of Equation (3.54) is highly peaked near $Q^2 = 0$. Panel (a) of Figure 5.9 shows a typical integrand, produced by constraining an $R_{1,1}$ Padé using discrete moments. Note that a logarithmic scale has been used for the x -axis to better show the behaviour of the integrand at low- Q^2 . If this scale were not used, the sharp peak in the integrand at low- Q^2 would be immediately apparent. When integrating functions such as this it is necessary to sample the region occupied by the peak sufficiently in order to minimise integration errors. To achieve this I employed the change of variables recommended in [76], introducing the integration variable

$$t = \frac{1}{1 + \log\left(\frac{\hat{Q}_{\text{high}}^2}{Q^2}\right)}, \quad (5.23)$$

such that the low- and mid- Q^2 regions of the integral can be written as

$$4\alpha^2 \int_0^{Q_{\text{high}}^2} dQ^2 f(Q^2) \hat{\Pi}(Q^2) \rightarrow 4\alpha^2 \int_0^1 dt \frac{Q^2}{t^2} f(Q^2) \hat{\Pi}(Q^2). \quad (5.24)$$

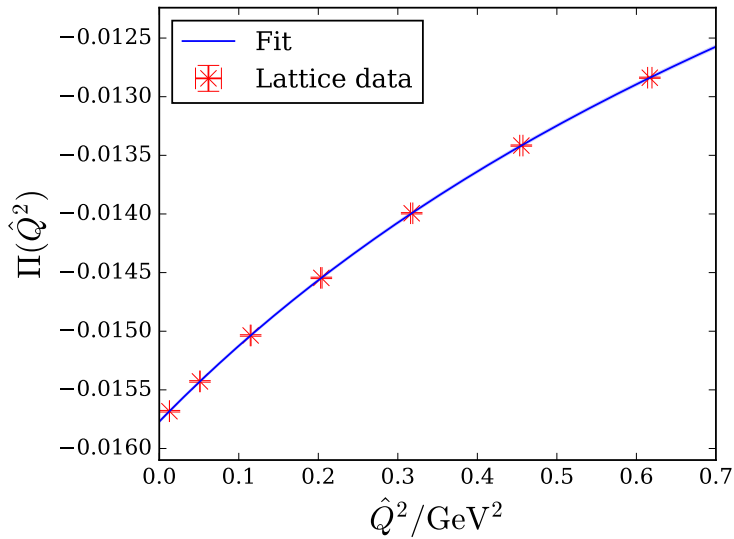


Figure 5.8: Resulting parametrisation after matching the Padé $R_{1,1}$ (see Equation (5.16)) using a χ^2 fit. The low cut in this case is 0.7 GeV^2 . This curve is typical of the parametrisations generated using the various analytical expressions and matching methods described in this paper. I find that these results typically pass within negligible distance of the lattice data point central values, meaning a fraction of the error on the lattice data points.

The effect of this variable change on the shape of the integrand can be observed in panel (b) of Figure 5.9. Whereas before the peak of the integrand was very narrow, it is now much broader, making it much easier for numerical integration techniques to accommodate. In addition to this change of variables, I also used an adaptive integrator to better account for variations in the derivatives of the integrand. I specified a relative error on the final value of the integral of 10^{-5} , which was achieved in all cases. This is far below the level of statistical uncertainty in the final value of $a_\mu^{(2)\text{had},s}$.

5.2.4 Integrating the High- Q^2 Region

I use the perturbation theory expression for the HVP at three loops in $\overline{\text{MS}}$ [164]. This formula requires a value for α_s and the strange quark mass in $\overline{\text{MS}}$. I run α_s from the mass of the Z boson² to 3 GeV at three flavours by integrating the differential equation [5]

$$\mu^2 \frac{d\alpha_s}{d\mu^2} = \beta(\alpha_s(\mu^2)), \quad (5.25)$$

where

$$\beta(\alpha_s(\mu^2)) = -4\pi \sum_{n=0}^3 \beta_n \left(\frac{\alpha_s(\mu^2)}{\pi} \right)^{n+2}, \quad (5.26)$$

and the beta coefficients β_n are given in Appendix F.

²I use $m_Z = 91.1876 \text{ GeV}$ [5].

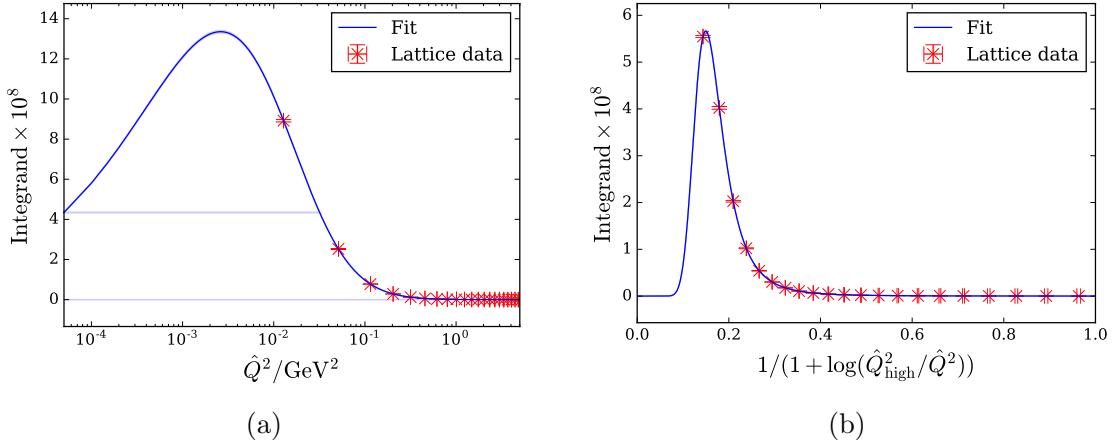


Figure 5.9: Effect of the change of variables specified in Equation (5.23) on the form of the integrand in Equation (3.54). In panel (a) I show the integrand before the change of variables (note the logarithmic scale on the x -axis), whilst in panel (b) I show the integrand resulting from the change of variables. The parametrisation is achieved using discrete moments to constrain an $R_{1,1}$ Padé. The red lattice data points are computed using unitary strange data on the 48I ensemble. The blue curves indicate the result of multiplying the constrained parametrisation with the QED kernel.

In the process of integrating Equation (5.25) from m_Z to 3 GeV one necessarily crosses at least one flavour boundary, which I define in the on-shell scheme. More specifically, the on-shell scheme specifies that the charm quark mass is equal to 1.6 GeV, the bottom mass is equal to 4.7 GeV and the top mass is equal to 175 GeV [5]. At $\mu = m_Z$, therefore, QCD can contain at most five quark flavours. At the flavour boundaries one must match the value of α_s in a theory with N_f flavours to that of a theory with $N_f - 1$. To achieve this I used the following equation [5]:

$$\alpha_s^{(N_f-1)}(\mu^2) = \left[1 - 0.02955201190 \left(\alpha_s^{(N_f)} \right)^2 + ((N_f - 1) \times 0.008465086429 - 0.1717036285) \left(\alpha_s^{(N_f)} \right)^3 \right] \alpha_s^{(N_f)}. \quad (5.27)$$

Since I require α_s in the three flavour theory, it is necessary to integrate α_s down to 1.6 GeV before integrating back up to 3 GeV without performing any flavour matching. Starting from $\alpha(m_Z) = 0.1185$, this procedure gives $\alpha_s(3 \text{ GeV}) = 0.24734$.

I use the strange quark mass in $\overline{\text{MS}}$ at 3 GeV for each ensemble. This is computed using the quark mass renormalisation constants taken from the results in [9], which I quote in Table 5.1. In summary:

$$m_s^{\overline{\text{MS}},3\text{GeV}} = Z_{\text{RI/SMOM} \rightarrow \overline{\text{MS}},3\text{GeV}} \times Z_m \times a^{-1} \times (am_s + am_{\text{res}}), \quad (5.28)$$

where $Z_{\text{RI/SMOM} \rightarrow \overline{\text{MS}},3\text{GeV}}$ is the conversion constant to move from the RI/SMOM scheme

to $\overline{\text{MS}}$ at 3 GeV and Z_m is the quark mass renormalisation constant for the given ensemble. I take $Z_{\text{RI}/\text{SMOM} \rightarrow \overline{\text{MS}}, 3\text{GeV}} = 0.9830$ from [175].

One might reasonably ask whether it is possible to compare the HVP as computed using lattice QCD with the result from perturbation theory. To make such a comparison one must first address the poorly understood UV cut-off effects present in the HVP at high- Q^2 . Unfortunately there is currently no immediate way to achieve this. However, advances in computing power coupled with possible algorithmic developments mean that it should be possible to generate gauge ensembles with much finer lattice spacings in the future, thus reducing the cut-off effects present in measurable quantities more generally. This would promote confidence in a comparison between the lattice HVP and that of perturbative QCD.

5.3 Sine Cardinal Interpolation

I also employ an alternative to the hybrid method that involves computing the HVP directly at an arbitrary momentum by performing the Fourier transform in Equation (5.2) at this momentum [155]. Instead of using $Q_t = 2\pi n_t/T$ with $n_t \in \mathbb{Z} \cap [-T/2, T/2)$ I now let n_t lie anywhere in the half-closed interval $[-T/2, T/2)$. This allows $a_\mu^{(2)\text{had}}$ to be computed without the need for a parametrisation of the HVP in the low- Q^2 region. This method is closely related to the existing field of sampling theory [176, 177], which is concerned with reconstructing continuous signals from discrete data. Specifically, the Nyquist–Shannon theorem provides a method for constructing the continuous function $x(t)$ from a set of discrete samples $x(nT)$ [178–181]:

$$x(t) = \sum_{n=-\infty}^{\infty} x(nT) \cdot \text{sinc}\left(\frac{t - nT}{T}\right), \quad (5.29)$$

where the sine cardinal function $\text{sinc}(x) = \frac{\sin x}{x}$. Because of this relationship, I refer to the technique used in this work as sine cardinal interpolation (SCI).

This method is closely related to the continuous time moments method described above. To understand this, consider the effect of varying Q_t when computing the HVP tensor. If Q_t is some Fourier momentum in the time direction on the lattice, and we wish to perform the SCI at some inaccessible momentum $Q'_t = Q_t + \delta Q_t$, we can expand the lattice Fourier transform as follows

$$\Pi_{ii}(Q'_t) = a^4 \sum_{t, \mathbf{x}} e^{iQ'_t t} C_{ii}(t, \mathbf{x}) \quad (5.30)$$

$$= a^4 \sum_{t, \mathbf{x}} e^{iQ_t t} C_{ii}(t, \mathbf{x}) + i\delta Q_t a^4 \sum_{t, \mathbf{x}} t e^{iQ_t t} C_{ii}(t, \mathbf{x}) + \mathcal{O}(\delta Q_t^2), \quad (5.31)$$

which gives:

$$\delta\Pi_{ii}(Q_t) = i\delta Q_t a^4 \sum_{t,\mathbf{x}} t e^{iQ_t t} C_{ii}(t, \mathbf{x}) + \mathcal{O}(\delta Q_t^2). \quad (5.32)$$

Dividing through by δQ_t and taking the limit $\delta Q_t \rightarrow 0$ gives the derivative of the Fourier transform with the respect to Q_t . Iterating this procedure an even number of times and taking $Q_t = 0$ produces the left-hand side of Equation (5.21). In a similar manner to the case of continuous moments, using values of Q_t that are inaccessible on the lattice incurs the possibility of finite-time effects. There are currently efforts underway within UKQCD to show that these effects decay exponentially with $m_\pi T$ [176, 177].

I use SCI to compute the HVP at arbitrary momenta up to Q_{high}^2 , after which I use the perturbative result. The portion of the integral below Q_{high}^2 is transformed in the same manner as described in Section 5.2.3.

5.4 Physical Mass and Continuum Extrapolations

I perform extrapolations to reach both the continuum limit and the physical strange quark mass using the values of $a_\mu^{(2)\text{had},s}$ computed on the two ensembles 48I and 64I in the unitary and partially quenched theories. To achieve this I perform a correlated fit using the ansatz

$$a_\mu^{(2)\text{had},s}(a^2, am_s) = a_{\mu,0}^{(2)\text{had},s} + \alpha a^2 + \beta \frac{am_s - am_s^{\text{phys}}}{am_s^{\text{phys}} + am_{\text{res}}}, \quad (5.33)$$

where am_{res} is the residual mass discussed in Section 4.4 and am_s^{phys} is the lattice strange quark mass required to give the target kaon mass for the ensemble in question, as specified in [9] and Table 5.1. The $\mathcal{O}(a)$ improvement of the MDWF action allows cut-off effects of this order to be neglected so that the extrapolation ansatz is a function of a^2 instead of a . The physical strange quark masses computed in [9] and stated in Table 5.1 have $\sim 0.5\%$ errors. As explained in Section 5.1.2, I did not repeat the analysis of [9] to account for the error on am_s^{phys} . Instead I accounted for the error on am_s^{phys} by sampling values from a Gaussian distribution for each of the two ensembles, using their respective errors and central values to define the distributions. Although this makes an assumption on the distribution of the values of am_s^{phys} , the systematic error associated with this assumption is likely to be negligible when compared to the level of noise introduced by the distribution. I then perform a correlated fit to the four values of $a_\mu^{(2)\text{had},s}$ computed in the aforementioned simulations.

I also performed a physical point extrapolation where the value of α in Equation (5.33) was set to zero, meaning the fit was constant with respect to a^2 . Since the fit was correlated, I was able to use the value of $\chi^2/\text{d.o.f.}$ and its associated p -value to determine the quality of the fit. In this particular case the values produced were not sufficient to

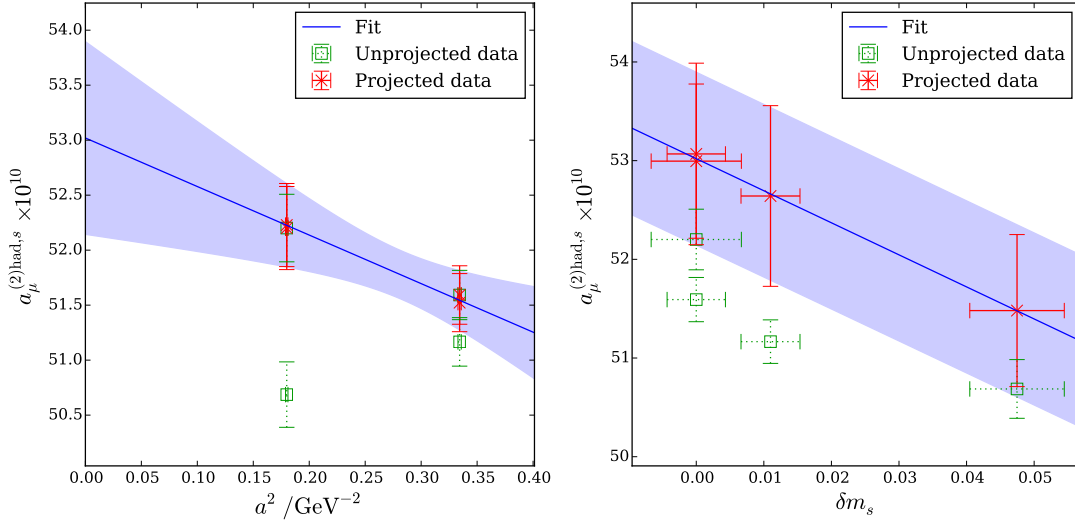


Figure 5.10: Example continuum and strange quark mass extrapolations. Here δm_s denotes the relative error in the strange quark mass as compared to the physical value. In the continuum limit plot we have subtracted out the variation in the values of $a_\mu^{(2)\text{had},s}$ resulting from the strange quark mass variation, and vice versa.

exclude this fit from the analysis. However, there is no theoretical justification for a lack of a^2 dependence in $a_\mu^{(2)\text{had},s}$ when MDWF is used. Furthermore, forcing $\alpha = 0$ could artificially reduce the error in the extrapolated value of $a_\mu^{(2)\text{had},s}$. I therefore deem it necessary to include the a^2 term in the fit ansatz.

I show an example set of extrapolations in Figure 5.10. Each panel illustrates the effect of projecting the simulation data into the limit described by the other panel in the figure. Specifically, in panel (a) the effects arising from the variation of the strange quark mass have been subtracted. In panel (b) the effects arising from the variation of the lattice spacing have been subtracted. This particular plot shows data computed using the conformal polynomial $P_3^{0.6\text{GeV}}$ parametrisation (see Equation (5.18)), constrained using discrete moments with a low cut of 0.7 GeV^2 . The effect of the strange quark mass mistuning on $a_\mu^{(2)\text{had},s}$ is striking: in the absence of the set of partially quenched measurements I observed a change in the sign on α when performing this extrapolation. This resulted in a shift in the value of $a_\mu^{(2)\text{had},s}$ from approximately 50×10^{-10} to 53×10^{-10} (see Figure 5.10).

5.5 Statistical Error Propagation

The evaluation of $a_\mu^{(2)\text{had},s}$ relies on several values determined by the analysis in [9], which used a number of different DWF ensembles as described above in Section 5.1.2. The lattice spacing is of particular importance to the present work as it facilitates the

reconciliation of the dimensionful muon mass m_μ and the dimensionless lattice momenta used in the QED kernel f . Indeed, the sensitivity of the peak of the integrand in the Euclidean integral for $a_\mu^{(2)\text{had},s}$ means that the final value of this integral is highly sensitive to fluctuations in the lattice spacing, or equivalently the muon mass. This effect can be observed by perturbing the muon mass m_μ and studying the effect on the value of $a_\mu^{(2)\text{had},s}$. On the 48I ensemble, for example, a 1% variation in m_μ produces a $\sim 2\%$ movement in the value of $a_\mu^{(2)\text{had},s}$. This effect will be amplified when the continuum and physical strange quark mass limits are taken. Accounting for the variation in the lattice spacing is therefore essential when quantifying the statistical uncertainty in $a_\mu^{(2)\text{had},s}$. Since, as I describe in Section 5.1.2, the present work does not make use of the global fit approach taken in [9], the error on the lattice spacing must be propagated using other means. Furthermore, the degree of sensitivity of the integrand towards the lattice spacing necessitates using samples of the latter that reflect its true distribution.

To account for the possible lack of Gaussianity in the lattice spacing a , I drew samples from the jackknife data computed and used in [9]. The nature of the analysis meant that a^{-1} received contributions from measurements on eighteen different ensembles, including the 48I and 64I ensembles. When constructing the bootstrap samples for use in this analysis it was therefore necessary to account for the fluctuations arising from each of these ensembles in the following way:

$$(a_e^{-1})^{(i)} = \langle a_e^{-1} \rangle + \sum_{e'} \delta(a_e^{-1})_{e'}^{(i)}, \quad (5.34)$$

where $(a_e^{-1})^{(i)}$ is the i th generated bootstrap value for ensemble e (in this case 48I or 64I) and $\langle a_e^{-1} \rangle$ is the central value of a^{-1} for ensemble e computed in the global fit. The value of $\delta(a_e^{-1})_{e'}^{(i)}$ is generated from a distribution of the fluctuations in a_e^{-1} arising from ensemble e' . This process involves building a histogram of the fluctuations, centred about zero, from which random samples are drawn. The sum over e' includes fluctuations from all eighteen ensembles used in the global fit of [9]. The resulting histograms of $a_{48\text{I}}^{-1}$ and $a_{64\text{I}}^{-1}$ are shown in Figure 5.11, accompanied by Gaussian curves generated using the central value and bootstrap error of each set of data. I applied the Shapiro–Wilk test of normality [182] to the data used to produce the histograms in Figure 5.11. I selected this test for normality based on the findings in [183], which suggests that the Shapiro–Wilk test has the greatest statistical power compared to other tests for normality. I obtained p -values of 1.7×10^{-13} for the 48I distribution and 7.9×10^{-6} for the 64I distribution. I therefore conclude that the null-hypothesis for the Shapiro–Wilk test, which states that the population is normally distributed, is false. It is therefore understood that, in the cases of the 48I and 64I ensembles, the inverse lattice spacing a^{-1} is not normally distributed. This indicates that generating a set of bootstrap samples using the original jackknife samples of [9] is a worthwhile procedure.

Including the lattice spacing error in the computation of $a_\mu^{(2)\text{had},s}$ produced a significant

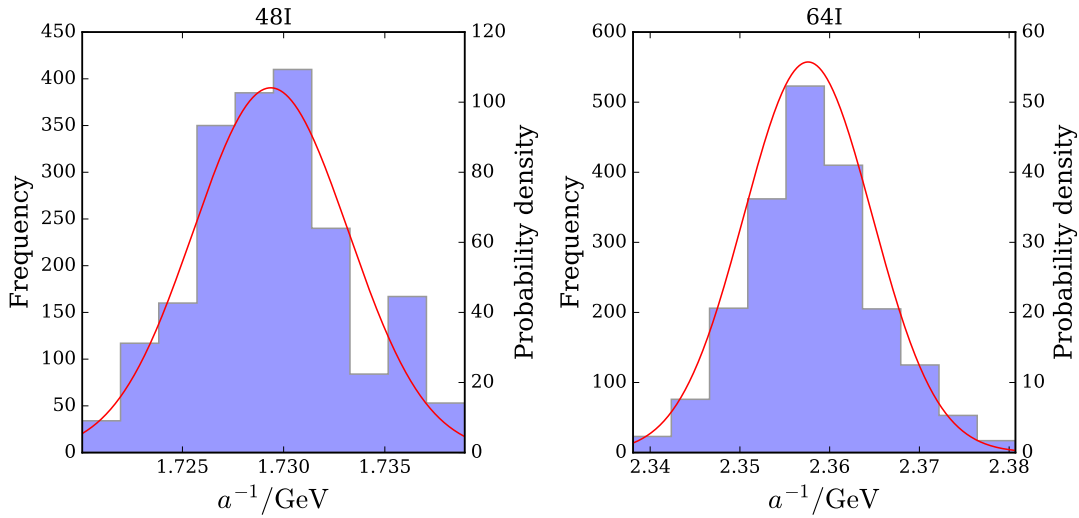


Figure 5.11: Histograms of a^{-1} for each of the ensembles used in this study, each overlaid with a normal distribution generated using the central value and the associated bootstrap error of the data. The left-hand plot illustrates the distribution of a^{-1} values for the 48I ensemble, whilst the right-hand plot corresponds to the 64I ensemble.

increase in the error on the final value of this quantity, a result of the strong dependence of the peak in the integrand (see Figure 5.9 for example) on the muon mass.

I also account for the error on Z_V , since $a_\mu^{(2)\text{had},s}$ is directly proportional to this quantity. Since the error on the former quantity is so small (0.04% for the 48I ensemble and 0.02% on the 64I ensemble), I propagate this effect through by sampling a normal distribution. As I argued in the case of am_s^{phys} , the systematic arising from this choice of distribution will likely be far smaller than the error it introduces into the final value of $a_\mu^{(2)\text{had},s}$.

One other error that one may consider propagating is the quark mass renormalisation constant Z_m . I do not include the effect of the error on this quantity, since the contribution to $a_\mu^{(2)\text{had},s}$ from the high- Q^2 region is a small fraction of the total value of $a_\mu^{(2)\text{had},s}$ ($\sim 0.2\%$ at the ensemble level).

5.6 Systematic Error Estimation

Given the range of available variations of the hybrid method, as well as the option of using SCI to compute $a_\mu^{(2)\text{had},s}$, it is worthwhile investigating the systematic uncertainty arising from the use of any one analysis technique. To this end I compute $a_\mu^{(2)\text{had},s}$ by varying the hybrid method in the ways described above before comparing the various results both with each other and with the result computed using SCI. From the various results a distribution can be constructed from which a systematic error may be determined.

5.6.1 Parametrisation Selection

In varying the parametrisation for the low- Q^2 region of the HVP, I initially selected three Padé approximants and six conformal polynomials, meaning nine parametrisations in total:

- $P_2^{0.5\text{GeV}}$, $P_2^{0.6\text{GeV}}$ and $R_{0,1}$, which each contain three parameters;
- $P_3^{0.5\text{GeV}}$, $P_3^{0.6\text{GeV}}$ and $R_{1,1}$, which each contain four parameters;
- $P_4^{0.5\text{GeV}}$, $P_4^{0.6\text{GeV}}$ and $R_{1,2}$, which each contain five parameters.

When specifying the conformal polynomials P_n^E , a value for E must be selected that lies below the two-particle mass threshold for the HVP. I have selected 0.5 and 0.6 GeV for the following reason. The vector meson resonance associated with an $\bar{s}\gamma_\mu s$ interpolating operator is the ϕ , with a mass of 1019.461(19) MeV [5]. As I discussed in Section 3.3.1, this is a resonance, and it is quite possible to consider a two particle state with the same quantum numbers as the ϕ but a smaller total mass. In Section 2.4.3 I also described how QCD conserves isospin and G -parity in the isospin limit. Since the $\bar{s}\gamma_\mu s$ is an *isoscalar* (meaning it has $I = 0$) and G -parity odd interpolating operator, this restricts the possible two-particle states that can couple to this operator. The lightest two-particle state we can construct with these quantum numbers would contain two kaons (see Table 2.3), suggesting that we require $E < 2m_K = 995$ MeV³. To be conservative and account for the uncertainty in the value of E , I selected two energy thresholds of 0.5 and 0.6 GeV, both of which are well below 0.995 GeV. Selecting two thresholds also allowed me to study how this quantity affects the final value of $a_\mu^{(2)\text{had},s}$.

As I discussed earlier in Section 5.2.1, the convergence of both Padé approximants and conformal polynomials to the HVP has been shown analytically [162, 165]. I observed that the value of $a_\mu^{(2)\text{had},s}$ saturated as the number of parameters in the parametrisations were increased. Figure 5.12 shows an example of this behaviour for the 48I ensemble. The movement in $a_\mu^{(2)\text{had},s}$ with the number of parameters is statistically resolvable in this case, which I take as a manifestation of this behaviour. Although this effect will be masked by larger statistical errors after the values of $a_\mu^{(2)\text{had},s}$ are extrapolated to the continuum and physical strange quark mass, the presence of this behaviour at the ensemble level is grounds for regarding the corresponding extrapolated values with suspicion. On this basis I decided to remove the parametrisations with only three parameters ($P_2^{0.5\text{GeV}}$, $P_2^{0.6\text{GeV}}$ and $R_{0,1}$) from the final determination of the systematic error. This decision is also in agreement with the findings in [162].

³This value is determined using the definition of the isoscalar kaon mass taken in [9].

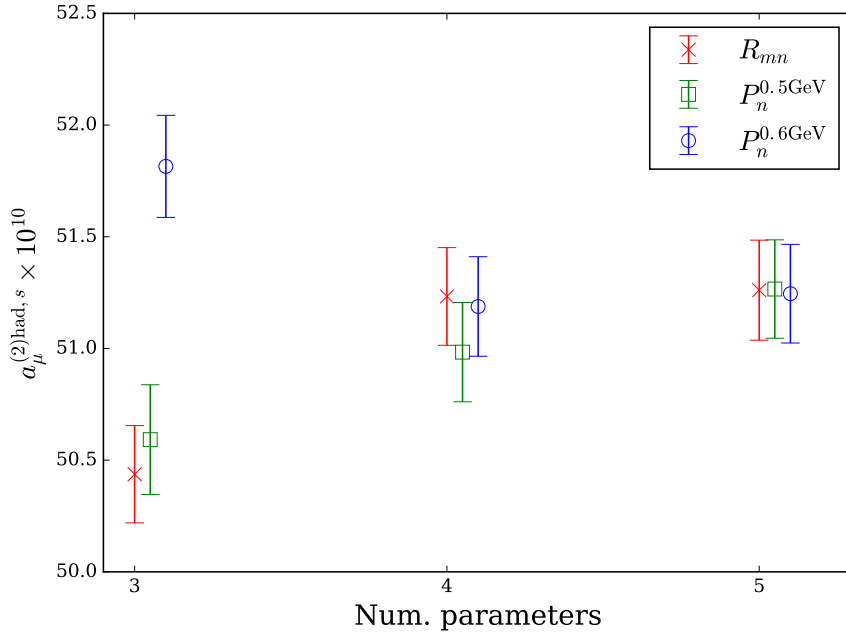


Figure 5.12: Dependence of $a_\mu^{(2)\text{had},s}$ on the number of parameters in the parametrisation used to represent the HVP in the low- Q^2 region. The data here was computed using the 48I ensemble with unitary strange quark masses. Within the hybrid method a fit was used to constrain the parametrisations with a low cut of 0.9 GeV² and a high cut of 5.0 GeV².

5.6.2 Selection of Momentum Cuts

I selected three low cuts: 0.5 GeV², 0.7 GeV² and 0.9 GeV². The lowest of these was chosen as it provided the single degree of freedom needed to perform a χ^2 fit for the parametrisations with five parameters. These cuts do not therefore prejudice any particular parametrisation by inhibiting a χ^2 fit: fits were possible for all the parametrisations above with all three cuts. These selections are also in accordance with the findings of the dispersive model study in [162] and those based on the recommendations of [169]. Accordingly, all the parametrisations and low cuts entering the final assessment of $a_\mu^{(2)\text{had},s}$ would be acceptable for use in computing the light quark, or *isovector*, contribution to $a_\mu^{(2)\text{had},s}$, with the exception of the $R_{1,1}$ parametrisation in the case where $Q_{\text{low}}^2 = 0.7$ and 0.9 GeV². Given the strange HVP form factor exhibits far weaker curvature than the light quark HVP at small Q^2 [161], it is anticipated that larger values of Q_{low}^2 are usable for any given parametrisation in the former case.

I also observed a saturation in the value of $a_\mu^{(2)\text{had},s}$ as the high cut was increased. Figure 5.13 illustrates this behaviour. To account for correlations between these determinations of $a_\mu^{(2)\text{had},s}$ we can examine their correlated differences. For example, the correlated difference between the values of $a_\mu^{(2)\text{had},s}$ computed with $Q_{\text{high}}^2 = 3.0$ GeV² and 7.0 GeV² is $1.463(1) \times 10^{-11}$, or $\sim 0.7\sigma$. Above 5.0 GeV² there is little movement

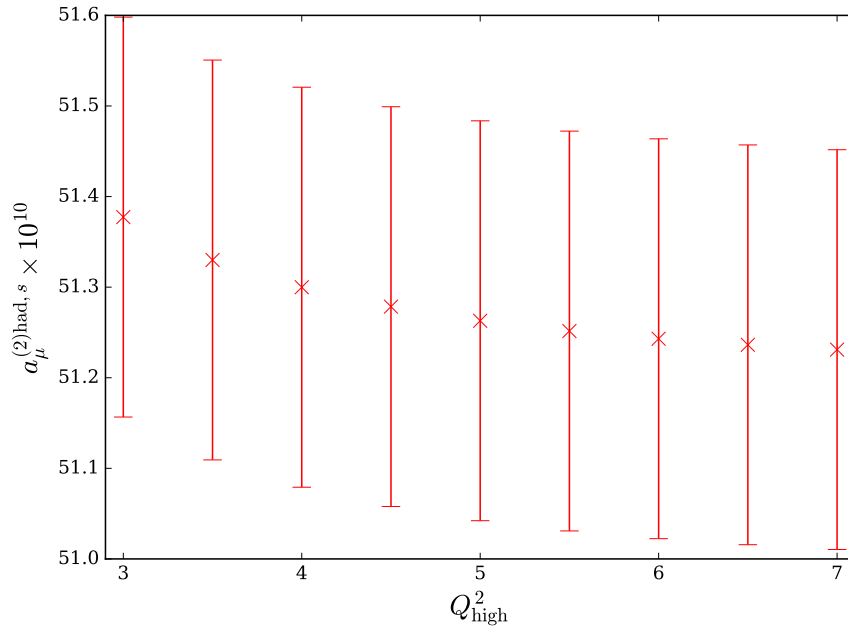


Figure 5.13: Dependence of $a_\mu^{(2)\text{had},s}$ on the value of Q_{high}^2 for values computed using unitary strange quark masses on the 48I ensemble. Here I have used the hybrid method, constraining the $R_{1,1}$ parametrisation using discrete time moments with a low cut of 0.7 GeV².

in the value of $a_\mu^{(2)\text{had},s}$, particularly when compared to the statistical error. For example, the separation between the values of $a_\mu^{(2)\text{had},s}$ computed using $Q_{\text{high}}^2 = 5.0$ GeV² and 7.0 GeV² is $\sim 0.1\sigma$. Although the correlated difference between these two values, equal to $3.18(1) \times 10^{-12}$, is statistically significant, one must consider it in the context of both the statistical error and the relative difference in $a_\mu^{(2)\text{had},s}$. In this latter case the correlated difference corresponds to approximately 0.06% of the central value of $a_\mu^{(2)\text{had},s}$. In addition, the exact cut-off dependence of $\Pi(\hat{Q}^2)$ is difficult to quantify, so a conservative choice for Q_{high}^2 is desirable. Furthermore, the statistical error on the final value of $a_\mu^{(2)\text{had},s}$ will be larger as a result of the continuum and strange quark mass extrapolations, such that the effect of the variation of Q_{high}^2 will be masked by the overall statistical error. On these grounds I have selected a single high cut of 5.0 GeV² in this analysis.

5.6.3 Numerical Integration Technique Selection

I selected two numerical techniques for use when integrating the mid- Q^2 region in the hybrid method. I used the trapezium rule and Simpson's rule.

When constraining the low- Q^2 parametrisations I used both discrete time moments and χ^2 fits to determine the extent to which either of these methods affected the final value of $a_\mu^{(2)\text{had},s}$.

5.6.4 Sine Cardinal Interpolation Tuning

In the case of SCI I selected a step in n_t of 0.005. This step size was sufficient to produce a value of $a_\mu^{(2)\text{had},s}$ where the integration error was negligible when compared to the statistical error. Specifically if the step in n_t was decreased to 0.001, the central value on $a_\mu^{(2)\text{had},s}$ shifted by approximately 1 part in 25000, which is far below the statistical error on the final value of $a_\mu^{(2)\text{had},s}$. In this case I used the same high cut of 5.0 GeV² as I selected for use in the hybrid method.

5.6.5 Distribution Results

The above variations in the analysis technique amount to 73 different analyses. Figure 5.14 contains stacked histograms of these 73 values of $a_\mu^{(2)\text{had},s}$, each colour coded according to which aspect of the analysis is being varied. This distribution is used to devise the determination of a systematic error in $a_\mu^{(2)\text{had},s}$ arising from any particular choice of analysis technique. I compute the central value in my final determination of $a_\mu^{(2)\text{had},s}$ by taking the median of this distribution. Since there are 73 separate analyses in this distribution this means that the central value will correspond to a particular technique, rather than an average of two. I then define the final statistical error as the bootstrap error on this central value. This process overlooks the spread in the statistical errors associated with the 73 separate central values. However, in the present case this spread is very small, with a total range of 1.8×10^{-12} . To determine the systematic error in $a_\mu^{(2)\text{had},s}$ I take the difference between the central value and the smallest and largest values in the distribution.

The resulting error is asymmetric, and from panels (a) and (b) in Figure 5.14 it is apparent that this asymmetry is predominantly due to the $P_3^{0.5\text{GeV}}$ parametrisation constrained using a χ^2 fit. This indicates that $a_\mu^{(2)\text{had},s}$ exhibits some dependence on the value of E , though for the two values under consideration this dependence is slight. Figure 5.15 illustrates this effect for a wider range of E , down to 0.2 GeV. Despite the conformal mapping that should guarantee the convergence of this parametrisation, conformal polynomials still appear subject to significant systematic errors when the two-particle mass threshold E is sufficiently small. Figure 5.16 shows the parametrisations resulting from constraining the $P_3^{0.2\text{GeV}}$ polynomial using both matching approaches. Both plots are indicative of the conformal polynomial being unable to represent the HVP. Where a fit is used, the polynomial is overconstrained by data at large \hat{Q}^2 , resulting in the parametrisation overestimating the magnitude of $\Pi(0)$. Where moments are used, the polynomial is well-constrained at small \hat{Q}^2 but begins to diverge from the true HVP as the low cut is approached. Requiring a smaller value of Q_{low}^2 given a reduction in the value of E is not entirely unexpected, since a smaller value of E will produce a larger value of w in the definition of the conformal polynomial. In this particular case

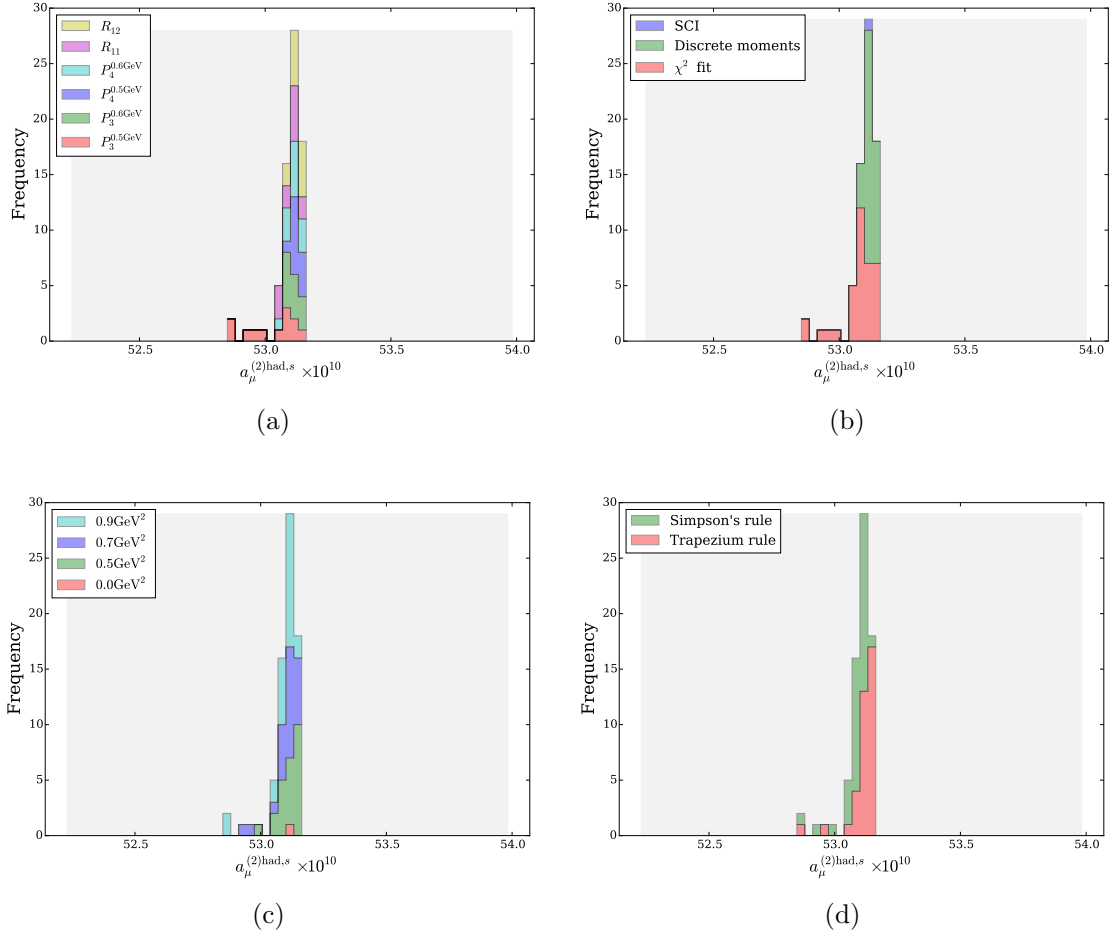


Figure 5.14: Stacked histograms describing the 73 values of $a_\mu^{(2)\text{had},s}$ computed using the various analysis techniques, colour coded by the low- Q^2 parametrisation (panel (a)), the method used to match these parametrisations (panel (b)), the low- Q^2 cut (panel (c)) and the numerical method used to integrate the mid- Q^2 region (panel (d)). The large grey band illustrates the final statistical error in the result.

where $Q^2 = Q_{\text{low}}^2 = 0.5 \text{ GeV}^2$, w moves from ~ -0.27 when $E = 0.5 \text{ GeV}$ to ~ -0.57 when $E = 0.2 \text{ GeV}$. The Taylor series in w upon which conformal polynomials are based will therefore converge more slowly for a given set of parameters. One would also expect a conformal polynomial of a given order to be more sensitive to variations in the parameters p_k that define it, making it more challenging to constrain to the level of numerical precision required.

Panel (a) also indicates the greater level of consistency amongst results computed using Padé approximants, denoted R_{mn} , compared to conformal polynomials, denoted P_n^E . It is evident that, for a given number of parameters, Padé approximants produce more consistent values of $a_\mu^{(2)\text{had},s}$ compared to conformal polynomials. This is in good agreement with the findings and recommendations of [162].

One feature immediately apparent in Figure 5.14 is the apparent lack of sensitivity of the

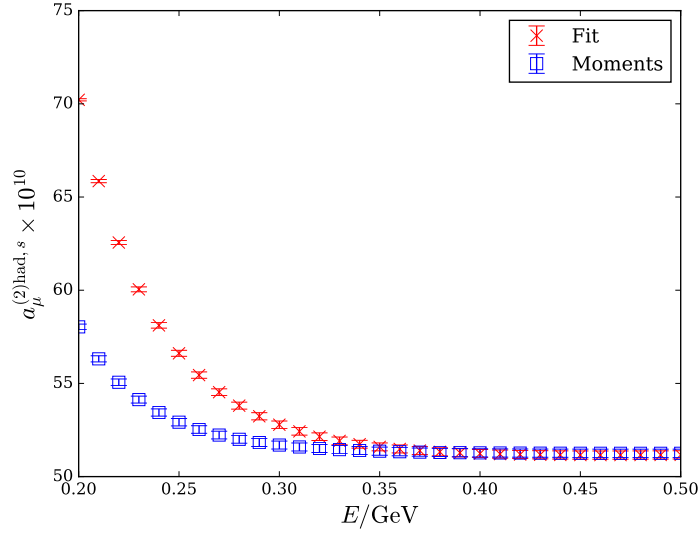


Figure 5.15: Dependence of $a_\mu^{(2)\text{had},s}$ on the value of the energy threshold used in the definition of the conformal polynomial. In this figure I show data for the P_3^E parametrisation, constrained using both matching methods with low and high cuts of 0.5 GeV^2 and 5.0 GeV^2 .

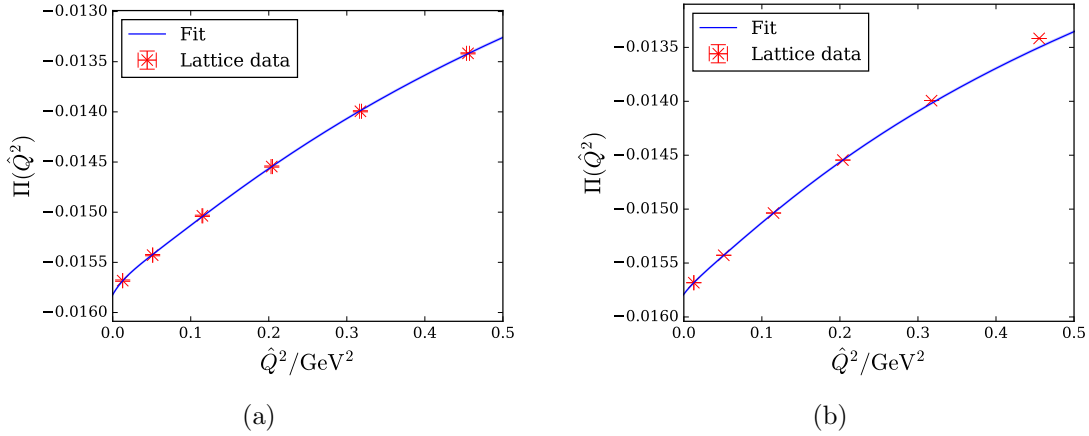


Figure 5.16: Parametrisations resulting from constraining the $P_3^{0.2\text{GeV}}$ parametrisation using both a χ^2 fit (left) and discrete moments (right). In both cases a high cut of 0.5 GeV^2 was used.

final value of $a_\mu^{(2)\text{had},s}$ towards the choice of analysis technique, particularly when compared to the overall statistical error. Indeed, the one set of analyses that could be considered outliers is approximately 0.25σ from the band of central values around 53×10^{-10} .

From panel (b) it is evident that the values of $a_\mu^{(2)\text{had},s}$ computed using the discrete moments are more self-consistent than those computed using a χ^2 fit. There are two reasons for this. First, the discrete moments method does not depend directly on the value of the low- Q^2 cut, meaning that the parameters for a particular parametrisation will be the same regardless of the choice of low cut. Second, since the moments method is based on a Taylor expansion of the HVP around $Q^2 = 0$, this method gives more

weight to long-distance contributions to the HVP. As a result, the parameters are more sensitive to variations in the HVP at low- Q^2 . This is in contrast to the χ^2 fit strategy, where the points at larger Q^2 have a greater statistical accuracy and so contribute more to the χ^2 , playing a more dominant role in constraining the low- Q^2 parametrisation than those at small Q^2 .

This does not mean however that the moments method will always produce an excellent parametrisation of the HVP for all Q^2 , but given the peak at low- Q^2 in the integrand of Equation (3.54), deviations from the true HVP at large Q^2 by one of these parametrisations will be suppressed by the QED kernel f .

Finally, the central value of $a_\mu^{(2)\text{had},s}$ computed using SCI shows good agreement with those computed using the other analysis methods. This indicates that the finite-time effects that could affect this method are negligible.

5.6.6 Finite Volume Effects

The two ensembles used in this study both have the same physical volume. As such it is not possible to perform an infinite volume extrapolation. In these circumstances one usually relies on low-energy effective theories of QCD in order to quantify the anticipated finite volume (FV) effects. The most widely used effective field theory is chiral perturbation theory (ChPT). Although the details of such calculations are outside the scope of the present work, an overview of the applications of ChPT to lattice QCD calculations may be found in [39]. Using ChPT it has been shown that observable quantities in lattice QCD are subject to FV effects that are proportional to e^{-mL} , where m is the mass of the lowest-lying energy state present in the simulation and L is the spatial extent of the lattice [184].

With respect to the strange HVP I expect FV effects to be small according to the argument detailed in [1]. The isovector contribution to the HVP is expected to be subject to significant FV volume effects as the ground state of this contribution is that of two pions. The isoscalar HVP and the associated strange quarks, however, are not expected to couple to pions in the isospin limit since this would violate isospin and G -parity conservation, as discussed in Section 2.4.3. As a result, one should not expect any FV effects arising from two-pion states in the present study. Instead, one expects the ground state to be dominated by two kaons (see Table 2.3 and the argument presented in Section 5.6.1), implying the leading FV effects are expected to be suppressed as $e^{-m_K L}$, where $m_K L \approx 13.8$ (from Table 5.1).

5.7 Final Result

The procedure outlined in Section 5.6 gives the final result:

$$a_\mu^{(2)\text{had},s} = 53.1(9)_{(-3)}^{(+1)} \times 10^{-10}, \quad (5.35)$$

where the first error is that arising from the statistical uncertainty in the calculation and the second is that arising from systematic uncertainty. The central value and associated statistical error here correspond to the analysis performed with the $P_4^{0.5\text{GeV}}$ parametrisation, constrained using discrete moments, with a low cut of 0.5 GeV^2 and a high cut of 5.0 GeV^2 . Simpson's rule was used to compute the mid- Q^2 region of the integral in this case. If I omit those analysis where $P_n^{0.5\text{GeV}}$ is used to parametrise the low- Q^2 region, then the systematic error becomes much more symmetric:

$$a_\mu^{(2)\text{had},s} = 53.1(9)(1) \times 10^{-10}. \quad (5.36)$$

The total error in both of these values (approximately 2%) is dominated entirely by the statistical uncertainty in the result, illustrating the lack of sensitivity to any particular analysis technique. The total uncertainty is also small enough to permit future evaluations of $a_\mu^{(2)\text{had}}$ to obtain sub-percent precision.

Chapter 6

Conclusions

In this work I have computed the leading strange quark-connected contribution to the anomalous magnetic moment of the muon, producing the final result

$$a_{\mu}^{(2)\text{had},s} = 53.1(9)_{-3}^{+1} \times 10^{-10}, \quad (6.1)$$

where the first error is statistical and the second is systematic. The calculation used the chirally-symmetric domain wall fermion action, which provides $\mathcal{O}(a)$ improvement. The HVP, which is required in the calculation, was computed on two ensembles with physical sea-pion masses. To account for a slight mistuning in the mass of the strange quark on both ensembles, both unitary and partially quenched measurements of the HVP were performed. I then computed $a_{\mu}^{(2)\text{had},s}$ from the HVP using two methods. The first is the hybrid method as described in [162]. Since this method provides much scope for varying how the analysis is performed, I have computed $a_{\mu}^{(2)\text{had},s}$ using a number of variations to understand how its value is affected by each aspect of the analysis. The second method I use involves evaluating the HVP at arbitrary momenta using a Fourier transform, a technique called sine cardinal interpolation (SCI) [176]. From these analyses I was able to determine a systematic error associated with the use of any particular analysis technique.

The final error in the result is dominated by statistical uncertainty, indicating only a small degree of sensitivity toward the analysis technique used. This demonstrates that, for the strange contribution, both the hybrid method and SCI are robust analysis methods. Furthermore, my findings are in accordance with the results of the original paper on the hybrid method, which suggests that the weaker curvature of the strange HVP, as compared to the light, should be more forgiving towards parametrisation at small Q^2 [162]. The curvature of the HVP lessens as the quark mass is increased, which should reduce the sensitivity of the associated $a_{\mu}^{(2)\text{had}}$ contribution to the particular analysis method. We therefore expect that determinations of heavier contributions to $a_{\mu}^{(2)\text{had}}$,

such as that of the charm quark, will be largely insensitive to the variations on the hybrid method that have been considered here.

In comparing this result to that of others there is currently only one other determination of $a_\mu^{(2)\text{had},s}$. HPQCD quote a final value of $53.4(6) \times 10^{-10}$ [82], which agrees with our result. They cite the uncertainty in their lattice spacings as the main source of statistical uncertainty in their final result, which agrees with our observations in this work. The error on this determination of $a_\mu^{(2)\text{had},s}$ is far below that required to produce a total value of $a_\mu^{(2)\text{had}}$ with errors comparable to the value stated in the PDG.

In contrast to previous determinations of $a_\mu^{(2)\text{had}}$, and in particular that of [82], the present work explores the possible systematic effects resulting from the variation of the analysis technique in far greater detail. In [82], an $R_{2,1}$ Padé approximant is applied to parametrise the entire HVP, including the large Q^2 regime. The authors do study the effect of the order of the Padé used to parametrise the HVP, though the analysis and discussion of more general systematic effects on $a_\mu^{(2)\text{had},s}$ are less thorough than in the present work. In addition, the exact method used to derive the error budget presented towards the end of [82] could be more clear. In contrast, the use of the hybrid method in the present work provides an immediate advantage when reconciling perturbation theory with a parametrisation of the HVP at low- Q^2 . In addition, I have avoided any parametrisation of the HVP that is motivated by an effective theory, instead opting for those that are founded on the analytical properties of the HVP. I have thoroughly explored the dependence of $a_\mu^{(2)\text{had},s}$ on the particular way in which the hybrid method is performed. Furthermore, the present work uses ensembles with physical pion masses and measurements both at and close to the physical strange quark mass. In the former case this removes the need for an extrapolation that would increase the error on the final value of $a_\mu^{(2)\text{had},s}$. In the latter case the systematic error arising from an extrapolation to the physical strange quark mass is minimised. These results provide a strong foundation upon which the computation of additional contributions to $a_\mu^{(2)\text{had}}$ can be based.

RBC/UKQCD is making significant progress towards a complete lattice determination of the total value of $a_\mu^{(2)\text{had}}$. Earlier this year we published a determination of the quark-disconnected contribution with a statistical error that does not significantly reduce the signal-to-noise ratio on the total value of $a_\mu^{(2)\text{had}}$ [79], thus permitting a reasonable comparison with the value stated in the PDG. This calculation combined several computational techniques and recent theoretical developments to achieve significant statistical gains. In overview, $SU(3)$ flavour suppression, anticipated theoretically and studied in detail in [81], implied correlations between the light and strange quark-disconnected contributions needed to be accounted for. In addition, a full spacetime average over the lattice volume, without introducing additional noise, was sought. These points were addressed as follows:

- the light quark propagators were split into low and high eigenmode contributions such that the resulting eigenvectors could be used to compute the former contribution exactly;
- the high mode contribution was computed using sparse (or diluted) \mathbb{Z}_2 wall sources, which achieve the necessary volume average without introducing additional noise¹.

Finally, the mixed representation of the HVP described in [153] was used to gain a more detailed understanding of how each correlator timeslice, particularly those at large distances, contributes to $a_\mu^{(2)\text{had,disc}}$. This facilitated the removal of additional noise from the final determination of $a_\mu^{(2)\text{had,disc}}$ at the expense of an additional systematic error included in the total error budget.

Looking to the future, it is hoped that a similar set of techniques may be used to calculate the light contribution to a sufficient level of accuracy so that the total may be reasonably compared to both the current theoretical determination and the experimental measurement. Besides the light contribution, the charm will also be required, since this contribution is expected to be greater than the statistical uncertainty on the total. Finally, work on isospin corrections, which are expected to be of the order of 1% of the total value of $a_\mu^{(2)\text{had}}$, is currently in progress.

¹A study of such sources, motivated by the findings detailed in Section 5.1.3, formed my contribution to [79].

Appendix A

The Dirac Gamma Matrices

Here I summarise the Dirac gamma matrices γ_μ in Minkowski and Euclidean space.

A.1 Pauli Matrices

The Dirac gamma matrices in a given basis are sometimes described as 2×2 block matrices containing the Pauli matrices [49, 185]

$$\sigma_1 = \begin{pmatrix} 0 & 1 \\ 1 & 0 \end{pmatrix}, \quad \sigma_2 = \begin{pmatrix} 0 & -i \\ i & 0 \end{pmatrix}, \quad \sigma_3 = \begin{pmatrix} 1 & 0 \\ 0 & -1 \end{pmatrix}. \quad (\text{A.1})$$

These are also the generators of $SU(2)$, satisfying the Lie bracket

$$\left[\frac{\sigma_i}{2}, \frac{\sigma_j}{2} \right] = i\epsilon_{ijk}\sigma_k, \quad (\text{A.2})$$

where ϵ_{ijk} is the totally antisymmetric Levi-Civita tensor satisfying $\epsilon_{123} = +1$.

A.2 Minkowski Space

The Minkowski Dirac gamma matrices in four spacetime dimensions, with indices $\mu, \nu \in \{0, 1, 2, 3\}$, obey the following Clifford algebra [49, 186]:

$$\{\gamma_\mu, \gamma_\nu\} = 2g_{\mu\nu}. \quad (\text{A.3})$$

The fifth gamma matrix is Hermitian and defined by $\gamma^5 = i\gamma^0\gamma^1\gamma^2\gamma^3$. It satisfies the anti-commutator $\{\gamma^\mu, \gamma^5\} = 0$.

The adjoint of a gamma matrix can be expressed as $(\gamma^\mu)^\dagger = \gamma^0 \gamma^\mu \gamma^0$. Contractions of gamma matrices can be simplified using the following identities:

$$\gamma^\mu \gamma_\mu = 4\mathbb{1}_4, \quad (\text{A.4})$$

$$\gamma^\mu \gamma^\nu \gamma_\mu = -2\gamma^\nu, \quad (\text{A.5})$$

$$\gamma^\mu \gamma^\nu \gamma^\rho \gamma_\mu = 4g^{\nu\rho}, \quad (\text{A.6})$$

$$\gamma^\mu \gamma^\nu \gamma^\rho \gamma^\sigma \gamma_\mu = -2\gamma^\sigma \gamma^\rho \gamma^\nu. \quad (\text{A.7})$$

Gamma matrices also satisfy the following trace identities:

$$\text{Tr}(\text{odd number of } \gamma\text{'s}) = 0, \quad (\text{A.8})$$

$$\text{Tr}(\gamma^\mu \gamma^\nu) = 4g^{\mu\nu}, \quad (\text{A.9})$$

$$\text{Tr}(\gamma^5) = 0, \quad (\text{A.10})$$

$$\text{Tr}(\gamma^\mu \gamma^\nu \gamma^5) = 0. \quad (\text{A.11})$$

In this work I use the Weyl or chiral representation of the gamma matrices, given by:

$$\gamma^0 = \begin{pmatrix} 0 & \mathbb{1}_2 \\ \mathbb{1}_2 & 0 \end{pmatrix}, \quad \gamma^i = \begin{pmatrix} 0 & \sigma_i \\ -\sigma_i & 0 \end{pmatrix}, \quad \gamma^5 = \begin{pmatrix} -\mathbb{1}_2 & 0 \\ 0 & \mathbb{1}_2 \end{pmatrix}. \quad (\text{A.12})$$

A.3 Euclidean Space

In Euclidean space the Dirac gamma matrices obey the following Clifford algebra:

$$\{\gamma_\mu, \gamma_\nu\} = 2\delta_{\mu\nu}, \quad (\text{A.13})$$

where the indices $\mu, \nu \in 1, 2, 3, 4$. Here 4 corresponds to the time direction. In Euclidean space all gamma matrices are Hermitian, and the fifth gamma matrix is now defined as $\gamma_5 = \gamma_1 \gamma_2 \gamma_3 \gamma_4$, satisfying $\{\gamma_\mu, \gamma_5\} = 0$.

The chiral representation of the gamma matrices in Euclidean space is now given by

$$\gamma_i = \begin{pmatrix} 0 & -i\sigma_i \\ i\sigma_i & 0 \end{pmatrix}, \quad \gamma_4 = \begin{pmatrix} 0 & \mathbb{1}_2 \\ \mathbb{1}_2 & 0 \end{pmatrix}, \quad \gamma_5 = \begin{pmatrix} \mathbb{1}_2 & 0 \\ 0 & -\mathbb{1}_2 \end{pmatrix}. \quad (\text{A.14})$$

Appendix B

Euclidean Space Integral for the Anomalous Magnetic Moment

Here I present a more complete and pedagogical version of the derivation of the Euclidean space integral for the computation of the LO hadronic contribution to the anomalous magnetic moment. I follow closely the derivations and arguments in [72] and [101]

We begin by computing the NLO vertex diagram in QED, also known as the Schwinger term (panel (a) of Figure 3.1). This corresponds to the following replacement of the QED vertex Feynman rule:

$$-ie\gamma^\mu \rightarrow -ie(\gamma^\mu + \delta\Gamma^\mu(p, p')), \quad (\text{B.1})$$

where p and p' are the momenta of the incoming and outgoing leptons, respectively, and $\delta\Gamma^\mu$ is computed from the Feynman diagram as

$$\begin{aligned} & \bar{u}(p')\delta\Gamma^\mu(p, p')u(p) \\ &= -ie^2 \int \frac{d^4q}{(2\pi)^4} \frac{\bar{u}(p') [\gamma^\nu(\not{p}' - \not{q} + m_\ell)\gamma^\mu(\not{p} - \not{q} + m_\ell)\gamma_\nu] u(p)}{(q^2 + i\epsilon)((p' - q)^2 - m_\ell^2 + i\epsilon)((p - q)^2 - m_\ell^2 + i\epsilon)}, \quad (\text{B.2}) \end{aligned}$$

where $k = p' - p$, $u(p)$ and $\bar{u}(p')$ are spinors for the incoming and outgoing leptons, respectively, and m_ℓ is the lepton mass. Using naïve power counting, the superficial degree of divergence of this integral is zero, meaning it is superficially logarithmically divergent. Indeed, whilst the superficial degree of divergence of a diagram does not generally indicate the actual degree of divergence of an integral, in this particular case the two are in agreement. Furthermore, there are both infrared and ultraviolet divergences, the infrared arising from the photon propagator. However, the divergences do not affect the form factor F_2 , as I will explain below.

From the general form of the vertex function in Equation (3.5) and the Gordon identity it is possible to project out the form factor F_2 as [101]

$$F_2(k^2) = \frac{m_\ell^2}{k^2(k^2 - 4m_\ell^2)} \text{Tr} [P_\mu(p, p') \Gamma^\mu(p, p')], \quad (\text{B.3})$$

where the projector P_μ is given by

$$P_\mu(p, p') = (\not{p} - m_\ell) \left(\gamma_\mu - \frac{k^2 + 2m_\ell^2}{k^2 - 4m_\ell^2} \frac{p_\mu + p'_\mu}{m_\ell} \right) (\not{p}' - m_\ell). \quad (\text{B.4})$$

Applying this projection to the correction $\delta\Gamma^\mu$ gives

$$\begin{aligned} F_2(k^2) &= \frac{m_\ell^2}{k^2(k^2 - 4m_\ell^2)} \text{Tr} [P_\mu(p, p') \delta\Gamma^\mu(p, p')] \\ &= ie^2 \int \frac{d^4q}{(2\pi)^4} \frac{1}{(q^2 + i\epsilon)((p' - q)^2 - m_\ell^2 + i\epsilon)((p - q)^2 - m_\ell^2 + i\epsilon)} \\ &\quad \times \left[\frac{8m_\ell^2}{k^2 - 4m_\ell^2} \left(2(\ell \cdot q) + q^2 + \frac{(k \cdot q)^2}{k^2} \right) - 96 \frac{m_\ell^2(\ell \cdot q)^2}{(k^2 - 4m_\ell^2)^2} \right], \quad (\text{B.5}) \end{aligned}$$

where $\ell = (p + p')/2$. It is evident from this equation that the powers of q in the numerator are sufficient to remove the infrared divergence in the original integral. In addition, it should be noted that although each of the terms in the numerator that is quadratic in q is ultraviolet divergent, their combination is not. Since we desire $a_\ell = F_2(0)$, we must now take the limit $k^2 \rightarrow 0$. In this limit $p' \rightarrow p$ and hence $\ell \rightarrow p$, which allows us to write

$$\begin{aligned} a_\ell^{(1)\text{QED}} &= -ie^2 \int \frac{d^4q}{(2\pi)^4} \frac{1}{(q^2 + i\epsilon)((p - q)^2 - m_\ell^2 + i\epsilon)^2} \\ &\quad \times \left[\frac{16(p \cdot q)^2}{3m_\ell^2} + \frac{4}{3}q^2 + 4(p \cdot q) \right]. \quad (\text{B.6}) \end{aligned}$$

With a convergent integral for the anomalous magnetic moment derived, it remains to analytically continue it to Euclidean space and integrate out the angular dependence of q . The integrand in Equation (B.6) contains two Feynman propagators with poles at $\pm(E_q - i\epsilon)$ and $\pm(E_{\mathbf{p}-\mathbf{q}} - i\epsilon)$. The analytic continuation to Euclidean space is easily performed through the use of a Wick rotation [104]. We apply a phase dependence for the temporal component of each momentum. For example, in the case of the loop momentum q , we replace q_0 with $e^{i\theta}q_0$. It is then possible to vary θ from 0 to $\pi/2$ without crossing any of the poles present in the integrand. We can hence transform each Minkowski four-momentum into the corresponding one in Euclidean space. In the case of q , for example, we would introduce Q such that $Q_0 = iq_0$ and $Q_i = q_i$.

Equation (B.6) then becomes

$$a_\ell^{(1)\text{QED}} = -e^2 \int \frac{d^4 Q}{(2\pi)^4} \frac{1}{(Q^2 - i\epsilon)((P - Q)^2 + m_\ell^2 - i\epsilon)^2} \times \left[\frac{16(P \cdot Q)^2}{3m_\ell^2} - \frac{4}{3}Q^2 - 4(P \cdot Q) \right], \quad (\text{B.7})$$

where P and Q are the Euclidean four-momenta corresponding to the Minkowski four-momenta p and q . This reformulation in Euclidean space allows us to rewrite the angular dependence of the integrand in terms of Gegenbauer polynomials. The latter can be computed using the recurrence relation [187]

$$C_0(x) = 1 \quad (\text{B.8})$$

$$C_1(x) = 2x \quad (\text{B.9})$$

$$C_n(x) = 2xC_{n-1}(x) - C_{n-2}(x). \quad (\text{B.10})$$

For example, $C_2(x) = -1 + 4x^2$. Since there are now just two momenta involved in the integrand, we can also make use of the following relationship:

$$\frac{1}{((P - Q)^2 + m_\ell^2)^2} = \frac{\tilde{Z}^2(P, Q)}{P^2 Q^2} \frac{1}{1 - \tilde{Z}^2(P, Q)} \sum_{n=0}^{\infty} (n+1) \tilde{Z}^n(P, Q) C_n(\hat{P} \cdot \hat{Q}), \quad (\text{B.11})$$

where \hat{P} and \hat{Q} are unit vectors in the directions of the momenta P and Q , and

$$\tilde{Z}(P, Q) = \frac{P^2 + Q^2 + m_\ell^2 - \sqrt{(P^2 + Q^2 + m_\ell^2)^2 - 4P^2 Q^2}}{2\sqrt{P^2 Q^2}}. \quad (\text{B.12})$$

The numerator can similarly be rewritten using Gegenbauer polynomials:

$$\begin{aligned} & \frac{16(P \cdot Q)^2}{3m_\ell^2} - \frac{4}{3}Q^2 - 4(P \cdot Q) \\ &= -4 \left(\frac{1}{3}Q^2 \left(1 + \frac{P^2}{m_\ell^2} \right) C_0(\hat{P} \cdot \hat{Q}) + \frac{1}{2}\sqrt{P^2 Q^2} C_1(\hat{P} \cdot \hat{Q}) - \frac{P^2 Q^2}{3m_\ell^2} C_2(\hat{P} \cdot \hat{Q}) \right). \end{aligned} \quad (\text{B.13})$$

Combining these expressions allows us to write

$$\begin{aligned} a_\ell^{(1)\text{QED}} &= 4e^2 \int \frac{d^4 Q}{(2\pi)^4} \frac{\tilde{Z}^2(P, Q)}{P^2(Q^2)^2} \frac{1}{1 - \tilde{Z}^2(P, Q)} \sum_{n=0}^{\infty} (n+1) \tilde{Z}^n(P, Q) C_n(\hat{P} \cdot \hat{Q}) \\ &\times \left[\frac{1}{3}Q^2 \left(1 + \frac{P^2}{m_\ell^2} \right) C_0(\hat{P} \cdot \hat{Q}) + \frac{1}{2}\sqrt{P^2 Q^2} C_1(\hat{P} \cdot \hat{Q}) - \frac{P^2 Q^2}{3m_\ell^2} C_2(\hat{P} \cdot \hat{Q}) \right]. \end{aligned} \quad (\text{B.14})$$

To remove the angular dependence, we can split the integration measure into its separate radial and angular components, such that $d^4 Q = Q^3 dQ d\Omega_Q$, where $d\Omega_Q$ is the angular integration measure associated with Q . We can then make use of the following relation

to simplify this integral:

$$\int \frac{d\Omega_b}{2\pi^2} C_n(\hat{a} \cdot \hat{b}) C_m(\hat{b} \cdot \hat{c}) = \frac{\delta_{mn}}{n+1} C_n(\hat{a} \cdot \hat{b}), \quad (\text{B.15})$$

for some arbitrary unit vectors \hat{a} , \hat{b} and \hat{c} . Equation (B.14) hence reduces to

$$a_\ell^{(1)\text{QED}} = \frac{e^2}{2\pi^2} \int dQ \frac{\tilde{Z}^2(P, Q)}{QP^2} \frac{1}{1 - \tilde{Z}^2(P, Q)} \times \left[\frac{1}{3} Q^2 \left(1 + \frac{P^2}{m_\ell^2} \right) + \sqrt{P^2 Q^2} \tilde{Z}(P, Q) - \frac{P^2 Q^2}{m_\ell^2} \tilde{Z}^2(P, Q) \right], \quad (\text{B.16})$$

where we note that Q is now understood as the magnitude of the Euclidean loop momentum. Constraining the muon momentum P to be on-shell, such that $P^2 = -m_\ell^2$, introducing $Z = -\sqrt{P^2 Q^2} \tilde{Z}(P, Q)$, and using $\alpha = e^2/4\pi$, our result for $a_\ell^{(1)\text{QED}}$ simplifies to

$$a_\ell^{(1)\text{QED}} = \frac{\alpha}{\pi} \int dQ^2 \frac{m_\ell^2 Q^2 Z^3 (1 - Q^2 Z)}{1 + m_\ell^2 Q^2 Z^2} \equiv \frac{\alpha}{\pi} \int dQ^2 f(Q^2). \quad (\text{B.17})$$

With P on-shell, Z is given by

$$Z = -\frac{Q^2 - \sqrt{Q^4 + 4m_\ell^2 Q^2}}{2m_\ell^2 Q^2}. \quad (\text{B.18})$$

We have hence derived a formula for the calculation of the NLO contribution to a_ℓ in QED in Euclidean space, such that the loop momentum being integrated over is that of the photon. Note that the integrand $f(Q^2) \rightarrow \infty$ as $Q^2 \rightarrow 0$. Despite this, it is possible to evaluate the integral in Equation (B.17), with the result giving the historic Schwinger term, $\alpha/2\pi \approx 1.1614 \times 10^{-3}$.

Appendix C

The Källén–Lehmann Representation of the HVP

Here I derive the Källén–Lehmann spectral representation [64, 65] of the HVP, given by

$$\Pi_{\mu\nu}(q) = \int_0^\infty \frac{d\mu^2}{2\pi} \rho(\mu^2) \frac{-i}{q^2 - \mu^2 + i\epsilon} \left(g_{\mu\nu} - \frac{q_\mu q_\nu}{q^2} \right), \quad (\text{C.1})$$

where the spectral density $\rho(\mu^2)$ is given by

$$\rho(\mu^2) = \frac{1}{3} \sum_\lambda (2\pi) \delta(\mu^2 - m_\lambda^2) \langle \Omega | j^\mu(0) | \lambda_{\mathbf{0}}^s \rangle \langle \lambda_{\mathbf{0}}^s | j_\mu(0) | \Omega \rangle, \quad (\text{C.2})$$

and $|\Omega\rangle$ is the vector ground state, $|\lambda_{\mathbf{0}}^s\rangle$ is a simultaneous eigenstate of energy, momentum and spin and $j^\mu(x)$ is a general conserved vector current. What follows is based on the discussion of field strength renormalisation in Chapter 7 of [40].

To begin we consider the vector two-point function $\langle \Omega | j^\mu(x) j^\nu(y) | \Omega \rangle$. We wish to insert a complete set of multi-particle states between the two currents. We can select the states to be eigenstates of the Hamiltonian H and hence the momentum operator \mathbf{P} . In addition, the two-point function is Lorentz invariant. This means that any energy eigenstate of the system with momentum \mathbf{p} can be boosted to zero momentum whilst remaining an eigenstate of H . The intermediate states are vectors and so must have spin. We can assume that we are working in a theory where the spin and Hamiltonian operators commute. Combining this information we consider the completeness relation as the sum over all possible intermediate eigenstates $|\lambda_{\mathbf{p}}^s\rangle$ of momentum \mathbf{p} and spin s :

$$\mathbf{1} = |\Omega\rangle\langle\Omega| + \sum_\lambda \int \frac{d^3\mathbf{p}}{(2\pi)^3} \frac{1}{2E_{\mathbf{p}}(\lambda)} |\lambda_{\mathbf{p}}^s\rangle\langle\lambda_{\mathbf{p}}^s|. \quad (\text{C.3})$$

Inserting this into the expression for the two-point function gives

$$\langle \Omega | j^\mu(x) j^\nu(y) | \Omega \rangle = \sum_\lambda \int \frac{d^3 \mathbf{p}}{(2\pi)^3} \frac{1}{2E_{\mathbf{p}}(\lambda)} \langle \Omega | j^\mu(x) | \lambda_{\mathbf{p}}^s \rangle \langle \lambda_{\mathbf{p}}^s | j^\nu(y) | \Omega \rangle, \quad (\text{C.4})$$

where for now I have assumed $x^0 > y^0$ whilst dropping the term $\langle \Omega | j^\mu(x) | \Omega \rangle \langle \Omega | j^\nu(y) | \Omega \rangle$ to preserve Lorentz invariance of the two-point function. I now consider each of the bra-ket objects under the integral, starting with $\langle \Omega | j^\mu(x) | \lambda_{\mathbf{p}}^s \rangle$:

$$\langle \Omega | j^\mu(x) | \lambda_{\mathbf{p}}^s \rangle = \langle \Omega | e^{i\mathbf{P}\cdot\mathbf{x}} j^\mu(0) e^{-i\mathbf{P}\cdot\mathbf{x}} | \lambda_{\mathbf{p}}^s \rangle \quad (\text{C.5})$$

$$= \langle \Omega | j^\mu(0) | \lambda_{\mathbf{p}}^s \rangle e^{-ip\cdot x} \Big|_{p^0=E_{\mathbf{p}}} \quad (\text{C.6})$$

$$= \langle \Omega | U^{-1} U j^\mu(0) U^{-1} U | \lambda_{\mathbf{p}}^s \rangle e^{-ip\cdot x} \Big|_{p^0=E_{\mathbf{p}}} \quad (\text{C.7})$$

$$= (\Lambda^{-1})^\mu{}_\nu \langle \Omega | j^\nu(0) | \lambda_{\mathbf{0}}^s \rangle e^{-ip\cdot x} \Big|_{p^0=E_{\mathbf{p}}}, \quad (\text{C.8})$$

where I have inserted Lorentz boost operators U and U^{-1} on the third line to boost the state from momentum \mathbf{p} to $\mathbf{0}$. For the other bra-ket one similarly obtains

$$\langle \lambda_{\mathbf{p}}^s | j^\mu(x) | \Omega \rangle = (\Lambda^{-1})^\mu{}_\nu \langle \lambda_{\mathbf{0}}^s | j^\nu(0) | \Omega \rangle e^{ip\cdot x} \Big|_{p^0=E_{\mathbf{p}}}. \quad (\text{C.9})$$

Inserting these results into Equation (C.4) gives

$$\begin{aligned} \langle \Omega | j^\mu(x) j^\nu(y) | \Omega \rangle &= \sum_\lambda \int \frac{d^3 \mathbf{p}}{(2\pi)^3} \frac{1}{2E_{\mathbf{p}}(\lambda)} (\Lambda^{-1})^\mu{}_\rho (\Lambda^{-1})^\nu{}_\sigma \\ &\quad \times e^{-ip\cdot(x-y)} \langle \Omega | j^\rho(0) | \lambda_{\mathbf{0}}^s \rangle \langle \lambda_{\mathbf{0}}^s | j^\sigma(0) | \Omega \rangle \Big|_{p^0=E_{\mathbf{p}}}. \end{aligned} \quad (\text{C.10})$$

Next we can introduce an integral over p^0 and use the causality of the two-point function (still assuming that $x^0 > y^0$) to make the replacement

$$\int \frac{d^3 \mathbf{p}}{(2\pi)^3} \frac{1}{2E_{\mathbf{p}}} e^{-ip\cdot(x-y)} \Big|_{p^0=E_{\mathbf{p}}} = \int \frac{d^4 p}{(2\pi)^4} \frac{-i}{p^2 - m^2} e^{-ip\cdot(x-y)}, \quad (\text{C.11})$$

allowing us to write

$$\begin{aligned} \langle \Omega | j^\mu(x) j^\nu(y) | \Omega \rangle &= \sum_\lambda \int \frac{d^3 p}{(2\pi)^4} \frac{-i}{p^2 - m_\lambda^2} (\Lambda^{-1})^\mu{}_\rho (\Lambda^{-1})^\nu{}_\sigma \\ &\quad \times e^{-ip\cdot(x-y)} \langle \Omega | j^\rho(0) | \lambda_{\mathbf{0}}^s \rangle \langle \lambda_{\mathbf{0}}^s | j^\sigma(0) | \Omega \rangle. \end{aligned} \quad (\text{C.12})$$

We now wish to extract tensor structure present in $(\Lambda^{-1})^\mu{}_\rho (\Lambda^{-1})^\nu{}_\sigma \langle \Omega | j^\rho(0) | \lambda_{\mathbf{0}}^s \rangle \langle \lambda_{\mathbf{0}}^s | j^\sigma(0) | \Omega \rangle$. To achieve this I note that the only two possible symmetric Lorentz structures are $g^{\mu\nu}$ and $p^\mu p^\nu$ and hence use the following form factor decomposition

$$(\Lambda^{-1})^\mu{}_\rho (\Lambda^{-1})^\nu{}_\sigma \langle \Omega | j^\rho(0) | \lambda_{\mathbf{0}}^s \rangle \langle \lambda_{\mathbf{0}}^s | j^\sigma(0) | \Omega \rangle = \pi_1(p^2) g^{\mu\nu} + \pi_2(p^2) \frac{p^\mu p^\nu}{p^2}. \quad (\text{C.13})$$

This can be simplified immediately using the vector Ward identity (see Section 3.3.2)

such that we require $\pi_1(p^2) = -\pi_2(p^2) \equiv \pi(p^2)$. Contracting the metric on both sides allows π to be expressed as a product of bra-kets:

$$\pi(p^2) = \frac{1}{3} \langle \Omega | j^\mu(0) | \lambda_{\mathbf{0}}^s \rangle \langle \lambda_{\mathbf{0}}^s | j_\mu(0) | \Omega \rangle. \quad (\text{C.14})$$

We can therefore write:

$$\langle \Omega | j^\mu(x) j^\nu(y) | \Omega \rangle = \sum_\lambda \int \frac{d^4 p}{(2\pi)^4} \pi(p^2) \frac{-ie^{-ip \cdot (x-y)}}{p^2 - m_\lambda^2} \left(g^{\mu\nu} - \frac{p^\mu p^\nu}{p^2} \right). \quad (\text{C.15})$$

A similar derivation holds for the case where $x^0 < y^0$, and combining these results allows us to write the time-ordered two-point function as

$$\langle \Omega | T j^\mu(x) j^\nu(y) | \Omega \rangle = \sum_\lambda \int \frac{d^4 p}{(2\pi)^4} \pi(p^2) \frac{-ie^{-ip \cdot (x-y)}}{p^2 - m_\lambda^2 + i\epsilon} \left(g^{\mu\nu} - \frac{p^\mu p^\nu}{p^2} \right). \quad (\text{C.16})$$

Finally, we can insert $\int_0^\infty \frac{d\mu^2}{2\pi} \delta(\mu^2 - m_\lambda^2)$ and write

$$\langle \Omega | T j^\mu(x) j^\nu(y) | \Omega \rangle = \int_0^\infty \frac{d\mu^2}{2\pi} \int \frac{d^4 p}{(2\pi)^4} \rho(p^2) \frac{-ie^{-ip \cdot (x-y)}}{p^2 - \mu^2 + i\epsilon} \left(g^{\mu\nu} - \frac{p^\mu p^\nu}{p^2} \right), \quad (\text{C.17})$$

where

$$\rho(p^2) = \frac{1}{3} \sum_\lambda 2\pi \delta(\mu^2 - m_\lambda^2) \langle \Omega | j^\mu(0) | \lambda_{\mathbf{0}}^s \rangle \langle \lambda_{\mathbf{0}}^s | j_\mu(0) | \Omega \rangle. \quad (\text{C.18})$$

Equivalently we can write this in momentum space, using the HVP tensor $\Pi^{\mu\nu}$ to write

$$\Pi^{\mu\nu}(q) = \int_0^\infty \frac{d\mu^2}{2\pi} \rho(p^2) \frac{-i}{q^2 - \mu^2 + i\epsilon} \left(g^{\mu\nu} - \frac{q^\mu q^\nu}{q^2} \right), \quad (\text{C.19})$$

which is the Källén–Lehmann representation of the HVP given in Equation (3.23).

Appendix D

The Equivalence of Domain Wall and Overlap Fermions

Here I describe the relationship between the five-dimensional domain wall theory and the effective four-dimensional theory, following the same derivation as in [9] and [142]. We first perform a change of basis:

$$S^5 = \bar{\Psi} D_{\text{DWF}}^5 \Psi = \bar{\chi} D_\chi^5 \chi, \quad (\text{D.1})$$

where $\chi = \mathcal{P}^{-1} \Psi$, $\bar{\chi} = \bar{\Psi} \gamma_5 Q_-$ and $D_\chi^5 = Q_-^{-1} \gamma_5 D_{\text{DWF}}^5 \mathcal{P}$. The matrices Q_\pm and \mathcal{P} are defined by $Q_\pm = \gamma_5 D_-^{-1} D_+ P_\pm \pm P_\mp$ and

$$\mathcal{P} = \begin{pmatrix} P_- & P_+ & 0 & \cdots & 0 \\ 0 & \ddots & \ddots & \ddots & \vdots \\ \vdots & \ddots & \ddots & \ddots & 0 \\ 0 & \cdots & \ddots & \ddots & P_+ \\ P_+ & 0 & \cdots & 0 & P_- \end{pmatrix}. \quad (\text{D.2})$$

The matrix D_χ^5 can be written explicitly as

$$D_\chi^5 = \begin{pmatrix} P_- - mP_+ & -T^{-1} & 0 & \cdots & 0 \\ 0 & 1 & T^{-1} & \ddots & \vdots \\ \vdots & \ddots & \ddots & \ddots & \vdots \\ 0 & \cdots & 0 & 1 & -T^{-1} \\ -T^{-1}(P_+ - mP_-) & 0 & \cdots & 0 & 1 \end{pmatrix}, \quad (\text{D.3})$$

where the transfer matrix T is defined by

$$T^{-1} = \frac{1 + H_M}{1 - H_M}, \quad H_M = \gamma_5 \frac{(b+c)D_W}{2 + (b-c)D_W}. \quad (\text{D.4})$$

We next extract the Schur complement of the matrix D_χ^5 . The Schur complement of some matrix can be extracted using the UDL decomposition

$$\begin{pmatrix} A & B \\ C & D \end{pmatrix} = \begin{pmatrix} 1 & BD^{-1} \\ 0 & 1 \end{pmatrix} \begin{pmatrix} S_\chi & 0 \\ 0 & D \end{pmatrix} \begin{pmatrix} 1 & 0 \\ D^{-1}C & 1 \end{pmatrix}, \quad (\text{D.5})$$

where A , B , C and D are block matrices. The element $S_\chi = A - BD^{-1}C$ is the Schur complement of the original matrix. Applying this procedure to D_χ^5 with $A = P_- - mP_+$ gives

$$S_\chi(m) = -(1 + T^{-L_s})\gamma_5 \left[\frac{1+m}{2} + \frac{1-m}{2} \gamma_5 \frac{T^{-L_s} - 1}{T^{-L_s} + 1} \right]. \quad (\text{D.6})$$

$S_\chi(m)$ can also be written as

$$S_\chi(m) = -(1 + T^{-L_s})\gamma_5 \left[\frac{1+m}{2} + \frac{1-m}{2} \gamma_5 \frac{(1 + H_M)^{L_s} - (1 - H_M)^{L_s}}{(1 + H_M)^{L_s} + (1 - H_M)^{L_s}} \right]. \quad (\text{D.7})$$

Setting $m = 0$ allows us to compare the four-dimensional matrix S_χ and the overlap operator in Equation (4.54). It is immediately apparent that the Schur complement S_χ contains the additional factor $-(1 + T^{-L_s})\gamma_5$, which results in massive degrees of freedom propagating in the fifth dimension. This is removed by the effect of pseudofermion Pauli–Villars fields $\bar{\Phi}$ and Φ , which obey Bose-Einstein statistics rather than Fermi-Dirac statistics [149, 150]. Including these fields in the five-dimensional path integral gives

$$\langle O \rangle_5 = \int \mathcal{D}[\bar{\Psi}, \Psi, \bar{\Phi}, \Phi, U] O e^{-S[\bar{\Psi}, \Psi, \bar{\Phi}, \Phi, U]}, \quad (\text{D.8})$$

where the action can be written as

$$S[\bar{\Psi}, \Psi, \bar{\Phi}, \Phi, U] = S_G[U] + \bar{\Psi} D_{\text{DWF}}^5 \Psi + \bar{\Phi} D_{\text{PV}}^5 \Phi. \quad (\text{D.9})$$

The operator D_{PV}^5 is defined similarly to D_{DWF}^5 in that the four-dimensional operator is the same, though there is some freedom in how the kinetic term in the fifth dimension is specified. From a numerical standpoint it is convenient to define $D_{\text{PV}}^5 \equiv D_{\text{DWF}}^5(m = 1)$ [151]. With the inclusion of the Pauli-Villars fields, the effective operator can be written

$$D_{\text{ov}} = S_\chi^{-1}(m = 1) S_\chi(m) = \frac{1+m}{2} + \frac{1-m}{2} \gamma_5 \frac{(1 + H_M)^{L_s} - (1 - H_M)^{L_s}}{(1 + H_M)^{L_s} + (1 - H_M)^{L_s}}. \quad (\text{D.10})$$

DWFs therefore approximate the sign function in the overlap operator as

$$\epsilon(H_M) \approx \epsilon_{L_s}(H_M) = \frac{(1 + H_M)^{L_s} - (1 - H_M)^{L_s}}{(1 + H_M)^{L_s} + (1 - H_M)^{L_s}} = \tanh(L_s \tanh^{-1} H_M). \quad (\text{D.11})$$

In the limit $L_s \rightarrow \infty$ this approximation becomes exact, and exact chiral symmetry is restored. Some simple matrix algebra allows the effective overlap operator to be written

using the original domain wall operator D_{DWF}^5 :

$$D_{\text{ov}} = \left[\mathcal{P}^{-1} (D_{\text{PV}}^5)^{-1} D_{\text{DWF}}^5(m) \mathcal{P} \right]_{00}. \quad (\text{D.12})$$

Appendix E

Transverse Projectors

Here I justify the lattice transverse projector given in Section 5.1.1:

$$P_{\mu\nu} = \delta_{\mu\nu} - e^{iaQ_\mu/2} e^{-iaQ_\nu/2} \frac{\hat{Q}_\mu \hat{Q}_\nu}{\hat{Q}^2}. \quad (5.5)$$

I do this by first considering the continuum transverse projector

$$P_{\mu\nu} = \delta_{\mu\nu} - \frac{q_\mu q_\nu}{q^2}, \quad (E.1)$$

which satisfies $P_{\mu\nu} P_{\nu\rho} = P_{\mu\rho}$. In position space this projector is given by

$$P_{\mu\nu} = \delta_{\mu\nu} + \partial_\mu (\partial^2)^{-1} \partial_\nu, \quad (E.2)$$

where $\partial^2 = \partial_\mu \partial^\mu$ is the Laplacian.

First I consider the momentum-space representations of the discrete derivatives in Equations (4.4) and (4.5). These can be derived using the lattice Fourier transform, which I define as

$$\tilde{f}(Q) = a^4 \sum_{x \in \Lambda} e^{-iQ \cdot x} f(x), \quad (E.3)$$

for a function f and its dual \tilde{f} defined on the lattice. To Fourier transform the forward and backward derivatives Δ_μ and Δ_μ^* , I consider the effect of Fourier transforming each derivative applied to f . For the forward derivative,

$$\tilde{\Delta}_\mu \tilde{f}(Q) = a^4 \sum_{x \in \Lambda} e^{-iQ \cdot x} \Delta_\mu f(x) \quad (E.4)$$

$$= a^4 \sum_{x \in \Lambda} \frac{f(x + \hat{\mu}) - f(x)}{a} e^{-iQ \cdot x}, \quad (E.5)$$

where $\hat{\mu}$ is translation of distance a in the μ th dimension and a is the lattice spacing. The periodic boundary conditions on the lattice mean that

$$\sum_{x \in \Lambda} f(x + \hat{\mu}) e^{-iQ \cdot x} = \sum_{x \in \Lambda} f(x) e^{-iQ \cdot (x - \hat{\mu})}. \quad (\text{E.6})$$

Using this I can complete the Fourier transform

$$\tilde{\Delta}_\mu \tilde{f}(Q) = a^4 \sum_{x \in \Lambda} \frac{f(x + \hat{\mu}) - f(x)}{a} e^{-iQ \cdot x} \quad (\text{E.7})$$

$$= a^4 \sum_{x \in \Lambda} \frac{1}{a} (e^{iaQ_\mu} - 1) f(x) e^{-iQ \cdot x} \quad (\text{E.8})$$

$$= ie^{iaQ_\mu/2} \frac{2}{a} \sin\left(\frac{aQ_\mu}{2}\right) \tilde{f}(Q), \quad (\text{E.9})$$

for convenience I now write $\hat{Q}_\mu = \frac{2}{a} \sin(aQ_\mu/2)$. A similar derivation for the backward derivative gives its dual $ie^{-iaQ_\mu/2} \hat{Q}_\mu$. We can therefore summarise

$$\Delta_\mu f(x) \Leftrightarrow ie^{iaQ_\mu/2} \hat{Q}_\mu \tilde{f}(Q), \quad (\text{E.10})$$

$$\Delta_\mu^* f(x) \Leftrightarrow ie^{-iaQ_\mu/2} \hat{Q}_\mu \tilde{f}(Q). \quad (\text{E.11})$$

Now that we know the duals of the discrete derivatives, we can determine the form of the transverse projector on the lattice. Rather than deriving this I will make an ansatz and show that it is both transverse and a projector. I choose to write the lattice Laplacian as $\Delta^2 = \sum_\mu \Delta_\mu^* \Delta_\mu$. Using this definition, the projector can be written in position space as

$$P_{\mu\nu} = \delta_{\mu\nu} + \Delta_\mu (\Delta^2)^{-1} \Delta_\nu^*, \quad (\text{E.12})$$

which has the dual given in Equation (5.5). It now remains to show that this is a transverse projector. First I note the context where transversality is required, namely the HVP, which obeys the Ward identity

$$\sum_\mu \Delta_\mu^* C_{\mu\nu}(x) = 0, \quad (\text{E.13})$$

where $C_{\mu\nu}(x)$ is the electromagnetic current two-point function defined in Equation (5.1). In momentum space we therefore require $\sum_\mu e^{-iaQ_\mu} \hat{Q}_\mu P_{\mu\nu} = 0$. This is straightforward to show:

$$\sum_\mu e^{-iaQ_\mu} \hat{Q}_\mu \left(\delta_{\mu\nu} - e^{iaQ_\mu/2} e^{-iaQ_\nu/2} \frac{\hat{Q}_\mu \hat{Q}_\nu}{\hat{Q}^2} \right) = e^{-iaQ_\nu} \hat{Q}_\nu - e^{-iaQ_\nu} \frac{\hat{Q}^2 \hat{Q}_\nu}{\hat{Q}^2} = 0. \quad (\text{E.14})$$

It is also straightforward to show that $P_{\mu\nu}$ obeys $\sum_{\nu} P_{\mu\nu} P_{\nu\rho} = P_{\mu\rho}$:

$$\begin{aligned}
& \sum_{\nu} P_{\mu\nu} P_{\nu\rho} \\
&= \sum_{\nu} \left(\delta_{\mu\nu} - e^{iaQ_{\mu}/2} e^{-iaQ_{\nu}/2} \frac{\hat{Q}_{\mu} \hat{Q}_{\nu}}{\hat{Q}^2} \right) \left(\delta_{\nu\rho} - e^{iaQ_{\nu}/2} e^{-iaQ_{\rho}/2} \frac{\hat{Q}_{\nu} \hat{Q}_{\rho}}{\hat{Q}^2} \right) \\
&= \delta_{\mu\rho} - 2e^{iaQ_{\mu}/2} e^{-iaQ_{\rho}/2} \frac{\hat{Q}_{\mu} \hat{Q}_{\rho}}{\hat{Q}^2} + e^{iaQ_{\mu}/2} e^{-iaQ_{\rho}/2} \frac{\hat{Q}_{\mu} \hat{Q}_{\rho} \hat{Q}^2}{\hat{Q}^4} = P_{\mu\rho}. \quad (\text{E.15})
\end{aligned}$$

$P_{\mu\nu}$ is therefore a transverse projector satisfying $\sum_{\mu} e^{-iaQ_{\mu}/2} \hat{Q}_{\mu} P_{\mu\nu} = 0$.

Appendix F

The QCD β -function

When running α_s I use the following form of the QCD β -function:

$$\beta(\alpha_s(\mu^2)) = -4\pi \sum_{n=0}^3 \beta_n \left(\frac{\alpha_s(\mu^2)}{\pi} \right)^{n+2}, \quad (\text{F.1})$$

where the beta coefficients β_n for QCD with N_f flavours are defined by [5]

$$\beta_0 = \frac{33 - 2N_f}{12} \quad (\text{F.2})$$

$$\beta_1 = \frac{102 - 38N_f}{16} \quad (\text{F.3})$$

$$\beta_2 = \frac{2857}{2} - \frac{5033}{18}N_f + \frac{325}{54}N_f^2 \quad (\text{F.4})$$

$$\beta_3 = 29243 - 6946.3N_f + 405.089N_f^2 + 1.49931N_f^3. \quad (\text{F.5})$$

References

- [1] RBC/UKQCD collaboration, T. Blum et al., *Lattice calculation of the leading strange quark-connected contribution to the muon g_2* , *JHEP* **04** (2016) 063, [[1602.01767](#)].
- [2] M. Spraggs, P. Boyle, L. Del Debbio, A. Jüttner, C. Lehner, K. Maltman et al., *The strange contribution to a_μ with physical quark masses using Möbius domain wall fermions*, *PoS LATTICE2015* (2016) 106, [[1601.00537](#)].
- [3] ATLAS collaboration, G. Aad et al., *Observation of a new particle in the search for the Standard Model Higgs boson with the ATLAS detector at the LHC*, *Phys. Lett.* **B716** (2012) 1–29, [[1207.7214](#)].
- [4] CMS collaboration, S. Chatrchyan et al., *Observation of a new boson at a mass of 125 GeV with the CMS experiment at the LHC*, *Phys. Lett.* **B716** (2012) 30–61, [[1207.7235](#)].
- [5] PARTICLE DATA GROUP collaboration, K. A. Olive et al., *Review of Particle Physics*, *Chin. Phys.* **C38** (2014) 090001.
- [6] F. Jegerlehner and A. Nyffeler, *The Muon $g - 2$* , *Phys. Rept.* **477** (2009) 1–110, [[0902.3360](#)].
- [7] FERMILAB E989 collaboration, J. Kaspar, *Status of the Fermilab $g - 2$ experiment*, *Nucl. Part. Phys. Proc.* **260** (2015) 243–246, [[1504.01201](#)].
- [8] J-PARC $G-2$ /EDM collaboration, N. Saito, *A novel precision measurement of muon $g-2$ and EDM at J-PARC*, *AIP Conf. Proc.* **1467** (2012) 45–56.
- [9] RBC, UKQCD collaboration, T. Blum et al., *Domain wall QCD with physical quark masses*, *Phys. Rev.* **D93** (2016) 074505, [[1411.7017](#)].
- [10] ETM collaboration, A. Abdel-Rehim, C. Alexandrou, M. Constantinou, K. Hadjiyiannakou, K. Jansen, C. Kallidonis et al., *Direct Evaluation of the Quark Content of Nucleons from Lattice QCD at the Physical Point*, *Phys. Rev. Lett.* **116** (2016) 252001, [[1601.01624](#)].

- [11] J. Koponen, F. Bursa, C. T. H. Davies, R. J. Dowdall and G. P. Lepage, *Size of the pion from full lattice QCD with physical u , d , s and c quarks*, *Phys. Rev. D* **93** (2016) 054503, [[1511.07382](#)].
- [12] S. Durr et al., *Lattice computation of the nucleon scalar quark contents at the physical point*, *Phys. Rev. Lett.* **116** (2016) 172001, [[1510.08013](#)].
- [13] RBC/UKQCD collaboration, P. A. Boyle et al., *The kaon semileptonic form factor in $N_f = 2 + 1$ domain wall lattice QCD with physical light quark masses*, *JHEP* **06** (2015) 164, [[1504.01692](#)].
- [14] R. J. Dowdall, C. T. H. Davies, R. R. Horgan, G. P. Lepage, C. J. Monahan and J. Shigemitsu, *B-meson mixing from full lattice QCD with physical u , d , s and c quarks*, [1411.6989](#).
- [15] T. Bhattacharya et al., *QCD Phase Transition with Chiral Quarks and Physical Quark Masses*, *Phys. Rev. Lett.* **113** (2014) 082001, [[1402.5175](#)].
- [16] SUPER-KAMIOKANDE collaboration, Y. Fukuda et al., *Evidence for oscillation of atmospheric neutrinos*, *Phys. Rev. Lett.* **81** (1998) 1562–1567, [[hep-ex/9807003](#)].
- [17] SNO collaboration, Q. R. Ahmad et al., *Direct evidence for neutrino flavor transformation from neutral current interactions in the Sudbury Neutrino Observatory*, *Phys. Rev. Lett.* **89** (2002) 011301, [[nucl-ex/0204008](#)].
- [18] W. N. Cottingham and D. A. Greenwood, *An introduction to the standard model of particle physics*. Cambridge University Press, 2007.
- [19] W. Pauli, *The Connection Between Spin and Statistics*, *Phys. Rev.* **58** (1940) 716–722.
- [20] H. Fritzsch, M. Gell-Mann and H. Leutwyler, *Advantages of the Color Octet Gluon Picture*, *Phys. Lett.* **B47** (1973) 365–368.
- [21] H. D. Politzer, *Reliable Perturbative Results for Strong Interactions?*, *Phys. Rev. Lett.* **30** (1973) 1346–1349.
- [22] D. J. Gross and F. Wilczek, *Ultraviolet Behavior of Nonabelian Gauge Theories*, *Phys. Rev. Lett.* **30** (1973) 1343–1346.
- [23] J. Goldstone, A. Salam and S. Weinberg, *Broken Symmetries*, *Phys. Rev.* **127** (1962) 965–970.
- [24] S. Weinberg, *A Model of Leptons*, *Phys. Rev. Lett.* **19** (1967) 1264–1266.
- [25] S. L. Glashow, *Partial Symmetries of Weak Interactions*, *Nucl. Phys.* **22** (1961) 579–588.

- [26] P. W. Higgs, *Broken Symmetries and the Masses of Gauge Bosons*, *Phys. Rev. Lett.* **13** (1964) 508–509.
- [27] P. W. Higgs, *Broken symmetries, massless particles and gauge fields*, *Phys. Lett.* **12** (1964) 132–133.
- [28] F. Englert and R. Brout, *Broken Symmetry and the Mass of Gauge Vector Mesons*, *Phys. Rev. Lett.* **13** (1964) 321–323.
- [29] G. S. Guralnik, C. R. Hagen and T. W. B. Kibble, *Global Conservation Laws and Massless Particles*, *Phys. Rev. Lett.* **13** (1964) 585–587.
- [30] N. Cabibbo, *Unitary Symmetry and Leptonic Decays*, *Phys. Rev. Lett.* **10** (1963) 531–533.
- [31] M. Kobayashi and T. Maskawa, *CP Violation in the Renormalizable Theory of Weak Interaction*, *Prog. Theor. Phys.* **49** (1973) 652–657.
- [32] E. Noether, *Invariant Variation Problems*, *Gott. Nachr.* **1918** (1918) 235–257, [[physics/0503066](#)].
- [33] E. L. Hill, *Hamilton’s principle and the conservation theorems of mathematical physics*, *Reviews of Modern Physics* **23** (1951) 253.
- [34] S. L. Adler, *Axial vector vertex in spinor electrodynamics*, *Phys. Rev.* **177** (1969) 2426–2438.
- [35] J. S. Bell and R. Jackiw, *A PCAC puzzle: $\pi^0 \rightarrow \gamma \gamma$ in the sigma model*, *Nuovo Cim.* **A60** (1969) 47–61.
- [36] M. Gell-Mann, R. J. Oakes and B. Renner, *Behavior of current divergences under $SU(3) \times SU(3)$* , *Phys. Rev.* **175** (1968) 2195–2199.
- [37] M. Gell-Mann, *The Symmetry group of vector and axial vector currents*, *Physics* **1** (1964) 63–75.
- [38] S. Scherer and M. R. Schindler, *A Primer for Chiral Perturbation Theory*, *Lect. Notes Phys.* **830** (2012) pp.1–338.
- [39] M. Golterman, *Applications of chiral perturbation theory to lattice QCD*, in *Modern perspectives in lattice QCD: Quantum field theory and high performance computing. Proceedings, International School, 93rd Session, Les Houches, France, August 3-28, 2009*, pp. 423–515, 2009. [0912.4042](#).
- [40] M. Peskin and D. Schroeder, *An Introduction To Quantum Field Theory*. Frontiers in physics. Westview Press, 1995.
- [41] M. Gell-Mann, *The eightfold way: A theory of strong interaction symmetry*, tech. rep., California Inst. of Tech., Pasadena. Synchrotron Lab., 1961.

- [42] M. Gell-Mann, *Symmetries of baryons and mesons*, *Phys. Rev.* **125** (1962) 1067–1084.
- [43] S. Coleman, *The invariance of the vacuum is the invariance of the world*, *Journal of Mathematical Physics* **7** (1966) 787–787.
- [44] W. Heisenberg, *On the structure of atomic nuclei*, *Z. Phys.* **77** (1932) 1–11.
- [45] Y. Ne’eman, *Derivation of strong interactions from a gauge invariance*, *Nucl. Phys.* **26** (1961) 222–229.
- [46] T. D. Lee and C.-N. Yang, *Charge Conjugation, a New Quantum Number G , and Selection Rules Concerning a Nucleon Anti-nucleon System*, *Nuovo Cim.* **10** (1956) 749–753.
- [47] C. Goebel, *Selection rules for $n\bar{N}$ annihilation*, *Phys. Rev.* **103** (Jul, 1956) 258–261.
- [48] D. Griffiths, *Introduction to Elementary Particles*. Physics textbook. Wiley, 2008.
- [49] P. A. Dirac, *The quantum theory of the electron*, in *Proceedings of the Royal Society of London A: Mathematical, Physical and Engineering Sciences*, vol. 117, pp. 610–624, The Royal Society, 1928.
- [50] F. J. Dyson, *The Radiation theories of Tomonaga, Schwinger, and Feynman*, *Phys. Rev.* **75** (1949) 486–502.
- [51] R. P. Feynman, *The Theory of positrons*, *Phys. Rev.* **76** (1949) 749–759.
- [52] S. Tomonaga, *On a relativistically invariant formulation of the quantum theory of wave fields*, *Prog. Theor. Phys.* **1** (1946) 27–42.
- [53] J. S. Schwinger, *Quantum electrodynamics. I A covariant formulation*, *Phys. Rev.* **74** (1948) 1439.
- [54] J. S. Schwinger, *On Quantum electrodynamics and the magnetic moment of the electron*, *Phys. Rev.* **73** (1948) 416–417.
- [55] J. C. Ward, *An Identity in Quantum Electrodynamics*, *Phys. Rev.* **78** (1950) 182.
- [56] Y. Takahashi, *On the generalized Ward identity*, *Nuovo Cim.* **6** (1957) 371.
- [57] M. Davier, A. Hoecker, B. Malaescu and Z. Zhang, *Reevaluation of the Hadronic Contributions to the Muon $g - 2$ and to $\alpha(M_Z)$* , *Eur. Phys. J.* **C71** (2011) 1515, [[1010.4180](#)].
- [58] K. Hagiwara, R. Liao, A. D. Martin, D. Nomura and T. Teubner, *$(g - 2)_\mu$ and $\alpha(M_Z^2)$ re-evaluated using new precise data*, *J. Phys.* **G38** (2011) 085003, [[1105.3149](#)].

- [59] T. Aoyama, M. Hayakawa, T. Kinoshita and M. Nio, *Complete Tenth-Order QED Contribution to the Muon $g-2$* , *Phys. Rev. Lett.* **109** (2012) 111808, [[1205.5370](#)].
- [60] D. Hanneke, S. F. Hoogerheide and G. Gabrielse, *Cavity Control of a Single-Electron Quantum Cyclotron: Measuring the Electron Magnetic Moment*, *Phys. Rev.* **A83** (2011) 052122, [[1009.4831](#)].
- [61] D. Hanneke, S. Fogwell and G. Gabrielse, *New Measurement of the Electron Magnetic Moment and the Fine Structure Constant*, *Phys. Rev. Lett.* **100** (2008) 120801, [[0801.1134](#)].
- [62] V. B. Berestetskii, O. N. Krokhnin and A. X. Klebnikov, *Concerning the radiative correction to the μ -meson magnetic moment*, *Sov. Phys. JETP* **3** (1956) 761.
- [63] M. Davier, S. Eidelman, A. Hocker and Z. Zhang, *Updated estimate of the muon magnetic moment using revised results from $e^+ e^-$ annihilation*, *Eur. Phys. J.* **C31** (2003) 503–510, [[hep-ph/0308213](#)].
- [64] G. Kallen, *On the definition of the Renormalization Constants in Quantum Electrodynamics*, *Helv. Phys. Acta* **25** (1952) 417.
- [65] H. Lehmann, *On the Properties of propagation functions and renormalization constants of quantized fields*, *Nuovo Cim.* **11** (1954) 342–357.
- [66] L. Durand, *Pionic Contributions to the Magnetic Moment of the Muon*, *Phys. Rev.* **128** (1962) 441–448.
- [67] G. Mie, *Beiträge zur optik trüber medien, speziell kolloidaler metallösungen*, *Annalen der physik* **330** (1908) 377–445.
- [68] R. Gans and H. Happel, *Zur optik kolloidaler metallösungen*, *Annalen der Physik* **334** (1909) 277–300.
- [69] E. Feenberg, *The Scattering of Slow Electrons by Neutral Atoms*, *Phys. Rev.* **40** (1932) 40–54.
- [70] W. Heisenberg, *The observable quantities in the theory of elementary particles*, *Z. Phys* **120** (1943) 513.
- [71] M. Davier, S. Eidelman, A. Hocker and Z. Zhang, *Confronting spectral functions from $e^+ e^-$ annihilation and tau decays: Consequences for the muon magnetic moment*, *Eur. Phys. J.* **C27** (2003) 497–521, [[hep-ph/0208177](#)].
- [72] T. Blum, *Lattice calculation of the lowest order hadronic contribution to the muon anomalous magnetic moment*, *Phys. Rev. Lett.* **91** (2003) 052001, [[hep-lat/0212018](#)].

- [73] C. Aubin and T. Blum, *Calculating the hadronic vacuum polarization and leading hadronic contribution to the muon anomalous magnetic moment with improved staggered quarks*, *Phys. Rev.* **D75** (2007) 114502, [[hep-lat/0608011](#)].
- [74] X. Feng, K. Jansen, M. Petschlies and D. B. Renner, *Two-flavor QCD correction to lepton magnetic moments at leading-order in the electromagnetic coupling*, *Phys. Rev. Lett.* **107** (2011) 081802, [[1103.4818](#)].
- [75] M. Della Morte, B. Jager, A. Jüttner and H. Wittig, *Towards a precise lattice determination of the leading hadronic contribution to $(g - 2)_\mu$* , *JHEP* **03** (2012) 055, [[1112.2894](#)].
- [76] P. Boyle, L. Del Debbio, E. Kerrane and J. Zanotti, *Lattice Determination of the Hadronic Contribution to the Muon $g - 2$ using Dynamical Domain Wall Fermions*, *Phys. Rev.* **D85** (2012) 074504, [[1107.1497](#)].
- [77] ETM collaboration, F. Burger, X. Feng, G. Hotzel, K. Jansen, M. Petschlies and D. B. Renner, *Four-Flavour Leading-Order Hadronic Contribution To The Muon Anomalous Magnetic Moment*, *JHEP* **02** (2014) 099, [[1308.4327](#)].
- [78] HPQCD collaboration, B. Chakraborty, C. T. H. Davies, P. G. de Oliviera, J. Koponen and G. P. Lepage, *The hadronic vacuum polarization contribution to a_μ from full lattice QCD*, [[1601.03071](#)].
- [79] RBC-UKQCD collaboration, T. Blum, P. A. Boyle, T. Izubuchi, L. Jin, A. Jüttner, C. Lehner et al., *Calculation of the hadronic vacuum polarization disconnected contribution to the muon anomalous magnetic moment*, *Phys. Rev. Lett.* **116** (2016) 232002, [[1512.09054](#)].
- [80] B. Chakraborty, C. T. H. Davies, J. Koponen, G. P. Lepage, M. J. Peardon and S. M. Ryan, *Estimate of the hadronic vacuum polarization disconnected contribution to the anomalous magnetic moment of the muon from lattice QCD*, *Phys. Rev.* **D93** (2016) 074509, [[1512.03270](#)].
- [81] V. Gülpers, A. Francis, B. Jäger, H. Meyer, G. von Hippel and H. Wittig, *The leading disconnected contribution to the anomalous magnetic moment of the muon*, *PoS LATTICE2014* (2014) 128, [[1411.7592](#)].
- [82] HPQCD collaboration, B. Chakraborty, C. T. H. Davies, G. C. Donald, R. J. Dowdall, J. Koponen, G. P. Lepage et al., *Strange and charm quark contributions to the anomalous magnetic moment of the muon*, *Phys. Rev.* **D89** (2014) 114501, [[1403.1778](#)].
- [83] G. Colangelo, M. Hoferichter, M. Procura and P. Stoffer, *Dispersion relation for hadronic light-by-light scattering: theoretical foundations*, *JHEP* **09** (2015) 074, [[1506.01386](#)].

- [84] G. Colangelo, M. Hoferichter, B. Kubis, M. Procura and P. Stoffer, *Towards a data-driven analysis of hadronic light-by-light scattering*, *Phys. Lett.* **B738** (2014) 6–12, [[1408.2517](#)].
- [85] V. Pauk and M. Vanderhaeghen, *Two-loop massive scalar three-point function in a dispersive approach*, [1403.7503](#).
- [86] V. Pauk and M. Vanderhaeghen, *Anomalous magnetic moment of the muon in a dispersive approach*, *Phys. Rev.* **D90** (2014) 113012, [[1409.0819](#)].
- [87] G. Colangelo, M. Hoferichter, M. Procura and P. Stoffer, *Dispersive approach to hadronic light-by-light scattering*, *JHEP* **09** (2014) 091, [[1402.7081](#)].
- [88] T. Blum, S. Chowdhury, M. Hayakawa and T. Izubuchi, *Hadronic light-by-light scattering contribution to the muon anomalous magnetic moment from lattice QCD*, *Phys. Rev. Lett.* **114** (2015) 012001, [[1407.2923](#)].
- [89] T. Blum, N. Christ, M. Hayakawa, T. Izubuchi, L. Jin and C. Lehner, *Lattice Calculation of Hadronic Light-by-Light Contribution to the Muon Anomalous Magnetic Moment*, *Phys. Rev.* **D93** (2016) 014503, [[1510.07100](#)].
- [90] J. Green, O. Gryniuk, G. von Hippel, H. B. Meyer and V. Pascalutsa, *Lattice QCD calculation of hadronic light-by-light scattering*, *Phys. Rev. Lett.* **115** (2015) 222003, [[1507.01577](#)].
- [91] G. C. Wick, *The Evaluation of the Collision Matrix*, *Phys. Rev.* **80** (1950) 268–272.
- [92] M. Della Morte and A. Jüttner, *Quark disconnected diagrams in chiral perturbation theory*, *JHEP* **11** (2010) 154, [[1009.3783](#)].
- [93] R. E. Cutkosky, *Singularities and discontinuities of Feynman amplitudes*, *J. Math. Phys.* **1** (1960) 429–433.
- [94] F. J. Dyson, *Heisenberg Operators in Quantum Electrodynamics. II*, *Phys. Rev.* **83** (1951) 608.
- [95] F. J. Dyson, *Divergence of perturbation theory in quantum electrodynamics*, *Phys. Rev.* **85** (1952) 631–632.
- [96] J. S. Schwinger, *Quantum electrodynamics. 2. Vacuum polarization and selfenergy*, *Phys. Rev.* **75** (1948) 651.
- [97] J. S. Schwinger, *On the classical radiation of accelerated electrons*, *Phys. Rev.* **75** (1949) 1912.
- [98] W. Pauli and F. Villars, *On the Invariant regularization in relativistic quantum theory*, *Rev. Mod. Phys.* **21** (1949) 434–444.

- [99] J. Bjorken and S. Drell, *Relativistic quantum fields*. International series in pure and applied physics. McGraw-Hill, 1965.
- [100] G. 't Hooft and M. J. G. Veltman, *Regularization and Renormalization of Gauge Fields*, *Nucl. Phys.* **B44** (1972) 189–213.
- [101] R. Z. Roskies, M. J. Levine and E. Remiddi, *Analytic evaluation of sixth order contributions to the electron's g factor*, *Adv. Ser. Direct. High Energy Phys.* **7** (1990) 162–217.
- [102] H. Suura and E. H. Wichmann, *Magnetic Moment of the Mu Meson*, *Phys. Rev.* **105** (1957) 1930–1931.
- [103] H. Elend, *On the anomalous magnetic moment of the muon*, *Physics Letters* **20** (1966) 682–684.
- [104] G. C. Wick, *Properties of Bethe-Salpeter Wave Functions*, *Phys. Rev.* **96** (1954) 1124–1134.
- [105] K. G. Wilson and J. B. Kogut, *The Renormalization group and the epsilon expansion*, *Phys. Rept.* **12** (1974) 75–200.
- [106] K. G. Wilson, *Confinement of Quarks*, *Phys. Rev.* **D10** (1974) 2445–2459.
- [107] P. T. Matthews and A. Salam, *The Green's functions of quantized fields*, *Nuovo Cim.* **12** (1954) 563–565.
- [108] P. T. Matthews and A. Salam, *Propagators of quantized field*, *Nuovo Cim.* **2** (1955) 120–134.
- [109] M. Luscher and P. Weisz, *On-Shell Improved Lattice Gauge Theories*, *Commun. Math. Phys.* **97** (1985) 59.
- [110] P. Weisz, *Continuum Limit Improved Lattice Action for Pure Yang-Mills Theory. 1.*, *Nucl. Phys.* **B212** (1983) 1–17.
- [111] P. Weisz and R. Wohlert, *Continuum Limit Improved Lattice Action for Pure Yang-Mills Theory. 2.*, *Nucl. Phys.* **B236** (1984) 397.
- [112] Y. Iwasaki, *Renormalization Group Analysis of Lattice Theories and Improved Lattice Action. II. Four-dimensional non-Abelian $SU(N)$ gauge model*, [1111.7054](#).
- [113] Y. Iwasaki and T. Yoshie, *Renormalization group improved action for $SU(3)$ lattice gauge theory and the string tension*, *Phys. Lett.* **B143** (1984) 449.
- [114] T. Takaishi, *Heavy quark potential and effective actions on blocked configurations*, *Phys. Rev.* **D54** (1996) 1050–1053.

- [115] K. G. Wilson, *Quarks and Strings on a Lattice*, in *Boston Conf. 1975:99*, *Erice Subnucl.Phys.1975:0069*, p. 99, 1975.
- [116] H. B. Nielsen and M. Ninomiya, *No Go Theorem for Regularizing Chiral Fermions*, *Phys. Lett.* **B105** (1981) 219–223.
- [117] N. Metropolis, A. W. Rosenbluth, M. N. Rosenbluth, A. H. Teller and E. Teller, *Equation of state calculations by fast computing machines*, *J. Chem. Phys.* **21** (1953) 1087–1092.
- [118] B. Efron, *The jackknife, the bootstrap and other resampling plans*, vol. 38. SIAM, 1982.
- [119] N. Madras and A. D. Sokal, *The Pivot algorithm: a highly efficient Monte Carlo method for selfavoiding walk*, *J. Statist. Phys.* **50** (1988) 109–186.
- [120] ALPHA collaboration, U. Wolff, *Monte Carlo errors with less errors*, *Comput. Phys. Commun.* **156** (2004) 143–153, [[hep-lat/0306017](#)].
- [121] M. Creutz, *Monte Carlo Study of Quantized SU(2) Gauge Theory*, *Phys. Rev.* **D21** (1980) 2308–2315.
- [122] A. D. Kennedy and B. J. Pendleton, *Improved Heat Bath Method for Monte Carlo Calculations in Lattice Gauge Theories*, *Phys. Lett.* **B156** (1985) 393–399.
- [123] S. L. Adler, *An Overrelaxation Method for the Monte Carlo Evaluation of the Partition Function for Multiquadratic Actions*, *Phys. Rev.* **D23** (1981) 2901.
- [124] P. Geiger and N. Isgur, *The Quenched Approximation in the Quark Model*, *Phys. Rev.* **D41** (1990) 1595.
- [125] S. Duane, A. D. Kennedy, B. J. Pendleton and D. Roweth, *Hybrid Monte Carlo*, *Phys. Lett.* **B195** (1987) 216–222.
- [126] M. R. Hestenes and E. Stiefel, *Methods of conjugate gradients for solving linear systems1*, *Journal of Research of the National Bureau of Standards* **49** (1952) .
- [127] C. Gattringer and C. B. Lang, *Quantum chromodynamics on the lattice*, *Lect. Notes Phys.* **788** (2010) 1–343.
- [128] RBC-UKQCD collaboration, P. A. Boyle, A. Jüttner, C. Kelly and R. D. Kenway, *Use of stochastic sources for the lattice determination of light quark physics*, *JHEP* **08** (2008) 086, [[0804.1501](#)].
- [129] UKQCD collaboration, C. McNeile and C. Michael, *Decay width of light quark hybrid meson from the lattice*, *Phys. Rev.* **D73** (2006) 074506, [[hep-lat/0603007](#)].

- [130] J. Foley, K. Jimmy Juge, A. O’Cais, M. Peardon, S. M. Ryan and J.-I. Skullerud, *Practical all-to-all propagators for lattice QCD*, *Comput. Phys. Commun.* **172** (2005) 145–162, [[hep-lat/0505023](#)].
- [131] TRINLAT collaboration, A. Ó Cais, K. J. Juge, M. J. Peardon, S. M. Ryan and J.-I. Skullerud, *Improving algorithms to compute all elements of the lattice quark propagator*, *Nucl. Phys. Proc. Suppl.* **140** (2005) 844–849, [[hep-lat/0409069](#)].
- [132] TXL collaboration, N. Eicker et al., *Evaluating sea quark contributions to flavor singlet operators in lattice QCD*, *Phys. Lett.* **B389** (1996) 720–726, [[hep-lat/9608040](#)].
- [133] UKQCD collaboration, M. Foster and C. Michael, *Quark mass dependence of hadron masses from lattice QCD*, *Phys. Rev.* **D59** (1999) 074503, [[hep-lat/9810021](#)].
- [134] S.-J. Dong and K.-F. Liu, *Stochastic estimation with $Z(2)$ noise*, *Phys. Lett.* **B328** (1994) 130–136, [[hep-lat/9308015](#)].
- [135] R. Groot, J. Hoek and J. Smit, *Normalization of Currents in Lattice QCD*, *Nucl. Phys.* **B237** (1984) 111–127.
- [136] P. H. Ginsparg and K. G. Wilson, *A Remnant of Chiral Symmetry on the Lattice*, *Phys. Rev.* **D25** (1982) 2649.
- [137] M. Luscher, *Exact chiral symmetry on the lattice and the Ginsparg-Wilson relation*, *Phys. Lett.* **B428** (1998) 342–345, [[hep-lat/9802011](#)].
- [138] R. Narayanan and H. Neuberger, *A Construction of lattice chiral gauge theories*, *Nucl. Phys.* **B443** (1995) 305–385, [[hep-th/9411108](#)].
- [139] R. Narayanan and H. Neuberger, *Chiral determinant as an overlap of two vacua*, *Nucl. Phys.* **B412** (1994) 574–606, [[hep-lat/9307006](#)].
- [140] R. Narayanan and H. Neuberger, *Infinitely many regulator fields for chiral fermions*, *Phys. Lett.* **B302** (1993) 62–69, [[hep-lat/9212019](#)].
- [141] D. B. Kaplan, *A Method for simulating chiral fermions on the lattice*, *Phys. Lett.* **B288** (1992) 342–347, [[hep-lat/9206013](#)].
- [142] A. D. Kennedy, *Algorithms for dynamical fermions*, [hep-lat/0607038](#).
- [143] Y. Shamir, *Chiral fermions from lattice boundaries*, *Nucl. Phys.* **B406** (1993) 90–106, [[hep-lat/9303005](#)].
- [144] R. C. Brower, H. Neff and K. Orginos, *Möbius fermions: Improved domain wall chiral fermions*, *Nucl. Phys. Proc. Suppl.* **140** (2005) 686–688, [[hep-lat/0409118](#)].

- [145] R. Brower, H. Neff and K. Orginos, *Möbius fermions*, *Nucl.Phys.Proc.Suppl.* **153** (2006) 191–198, [[hep-lat/0511031](#)].
- [146] R. C. Brower, H. Neff and K. Orginos, *The Möbius Domain Wall Fermion Algorithm*, [1206.5214](#).
- [147] V. Furman and Y. Shamir, *Axial symmetries in lattice QCD with Kaplan fermions*, *Nucl. Phys.* **B439** (1995) 54–78, [[hep-lat/9405004](#)].
- [148] T. Blum et al., *Quenched lattice QCD with domain wall fermions and the chiral limit*, *Phys. Rev.* **D69** (2004) 074502, [[hep-lat/0007038](#)].
- [149] H. Neuberger, *Vector - like gauge theories with almost massless fermions on the lattice*, *Phys. Rev.* **D57** (1998) 5417–5433, [[hep-lat/9710089](#)].
- [150] Y. Kikukawa and T. Noguchi, *Low-energy effective action of domain wall fermion and the Ginsparg-Wilson relation*, *Nucl. Phys. Proc. Suppl.* **83** (2000) 630–632, [[hep-lat/9902022](#)].
- [151] P. M. Vranas, *Chiral symmetry restoration in the Schwinger model with domain wall fermions*, *Phys. Rev.* **D57** (1998) 1415–1432, [[hep-lat/9705023](#)].
- [152] C. Aubin, T. Blum, P. Chau, M. Golterman, S. Peris and C. Tu, *Finite-volume effects in the muon anomalous magnetic moment on the lattice*, *Phys. Rev.* **D93** (2016) 054508, [[1512.07555](#)].
- [153] D. Bernecker and H. B. Meyer, *Vector Correlators in Lattice QCD: Methods and applications*, *Eur. Phys. J.* **A47** (2011) 148, [[1107.4388](#)].
- [154] JLQCD collaboration, E. Shintani, S. Aoki, H. Fukaya, S. Hashimoto, T. Kaneko, H. Matsufuru et al., *S-parameter and pseudo-Nambu-Goldstone boson mass from lattice QCD*, *Phys. Rev. Lett.* **101** (2008) 242001, [[0806.4222](#)].
- [155] X. Feng, S. Hashimoto, G. Hotzel, K. Jansen, M. Petschlies and D. B. Renner, *Computing the hadronic vacuum polarization function by analytic continuation*, *Phys. Rev.* **D88** (2013) 034505, [[1305.5878](#)].
- [156] M. Della Morte, B. Jager, A. Juttner and H. Wittig, *The leading hadronic vacuum polarisation on the lattice*, *AIP Conf. Proc.* **1343** (2011) 337–339, [[1011.5793](#)].
- [157] A. Francis, V. Gülpers, G. Herdoíza, G. von Hippel, H. Horch, B. Jäger et al., *Lattice QCD Studies of the Leading Order Hadronic Contribution to the Muon $g - 2$* , in *Proceedings, 37th International Conference on High Energy Physics (ICHEP 2014): Valencia, Spain, July 2-9, 2014*, 2014. [1411.3031](#).
- [158] C. T. Sachrajda and G. Villadoro, *Twisted boundary conditions in lattice simulations*, *Phys. Lett.* **B609** (2005) 73–85, [[hep-lat/0411033](#)].

- [159] C. Aubin, T. Blum, M. Golterman and S. Peris, *Hadronic vacuum polarization with twisted boundary conditions*, *Phys. Rev.* **D88** (2013) 074505, [[1307.4701](#)].
- [160] T. Blum and S. Chowdhury, *Hadronic contributions to $g-2$ from the lattice*, *Nucl. Phys. Proc. Suppl.* **189** (2009) 251–256.
- [161] M. Golterman, K. Maltman and S. Peris, *Tests of hadronic vacuum polarization fits for the muon anomalous magnetic moment*, *Phys. Rev.* **D88** (2013) 114508, [[1309.2153](#)].
- [162] M. Golterman, K. Maltman and S. Peris, *New strategy for the lattice evaluation of the leading order hadronic contribution to $(g-2)_\mu$* , *Phys.Rev.* **D90** (2014) 074508, [[1405.2389](#)].
- [163] M. Golterman, K. Maltman and S. Peris, *A Hybrid Strategy for the Lattice Evaluation of the Leading Order Hadronic Contribution to $(g-2)_\mu$* , *Nucl. Part. Phys. Proc.* **273-275** (2016) 1650–1656, [[1410.8405](#)].
- [164] K. G. Chetyrkin, J. H. Kuhn and M. Steinhauser, *Three loop polarization function and $O(\alpha_s^2)$ corrections to the production of heavy quarks*, *Nucl. Phys.* **B482** (1996) 213–240, [[hep-ph/9606230](#)].
- [165] C. Aubin, T. Blum, M. Golterman and S. Peris, *Pade approximants and $g-2$ for the muon*, *PoS LATTICE2012* (2012) 176, [[1210.7611](#)].
- [166] J. J. Sakurai, *Theory of strong interactions*, *Annals Phys.* **11** (1960) 1–48.
- [167] G. Amoros, J. Bijnens and P. Talavera, *Two point functions at two loops in three flavor chiral perturbation theory*, *Nucl. Phys.* **B568** (2000) 319–363, [[hep-ph/9907264](#)].
- [168] E. Golowich and J. Kambor, *Two loop analysis of vector current propagators in chiral perturbation theory*, *Nucl. Phys.* **B447** (1995) 373–404, [[hep-ph/9501318](#)].
- [169] C. Aubin, T. Blum, M. Golterman and S. Peris, *Model-independent parametrization of the hadronic vacuum polarization and $g-2$ for the muon on the lattice*, *Phys. Rev.* **D86** (2012) 054509, [[1205.3695](#)].
- [170] G. A. Baker, *Best error bounds for pade approximants to convergent series of stieltjes*, *J. Math. Phys.* **10** (1969) 814–820.
- [171] M. Barnsley, *The bounding properties of the multipoint pade approximant to a series of stieltjes on the real line*, *J. Math. Phys.* **14** (1973) 299–313.
- [172] H. Wall, *Analytic Theory of Continued Fractions*. The University series in higher mathematics. Van Nostrand, 1948.
- [173] E. H. Moore, *On the reciprocal of the general algebraic matrix*, *Bulletin of the American Mathematical Society* **26** (1920) 394–395.

- [174] R. Penrose, *A Generalized inverse for matrices*, *Proc. Cambridge Phil. Soc.* **51** (1955) 406–413.
- [175] RBC, UKQCD collaboration, R. Arthur et al., *Domain Wall QCD with Near-Physical Pions*, *Phys. Rev.* **D87** (2013) 094514, [[1208.4412](#)].
- [176] A. Portelli and L. Del Debbio, “Finite volume hadronic vacuum polarisation at arbitrary momenta.” Presented at The 33rd International Symposium on Lattice Field Theory, July, 2015.
- [177] L. Del Debbio and A. Portelli, to appear.
- [178] H. Nyquist, *Certain topics in telegraph transmission theory*, .
- [179] C. E. Shannon, *Communication in the presence of noise*, *Proceedings of the IRE* **37** (1949) 10–21.
- [180] E. T. Whittaker, *Xviii. on the functions which are represented by the expansions of the interpolation-theory*, *Proceedings of the Royal Society of Edinburgh* **35** (1, 1915) 181–194.
- [181] V. A. Kotelnikov, *On the carrying capacity of the ether and wire in telecommunications*, in *Material for the First All-Union Conference on Questions of Communication*, *Izd. Red. Upr. Svyazi RKKA, Moscow*, vol. 1, 1933.
- [182] S. S. Shapiro and M. B. Wilk, *An analysis of variance test for normality (complete samples)*, *Biometrika* **52** (1965) 591–611.
- [183] N. Razali and Y. B. Wah, *Power comparisons of Shapiro-Wilk, Kolmogorov-Smirnov, lilliefors and Anderson-Darling tests*, *Journal of Statistical Modeling and Analytics* **2** (June, 2011) .
- [184] J. Gasser and H. Leutwyler, *Light Quarks at Low Temperatures*, *Phys. Lett.* **B184** (1987) 83–88.
- [185] W. Pauli, *Zur quantenmechanik des magnetischen elektrons*, *Zeitschrift für Physik* **43** (1927) 601–623.
- [186] P. Clifford, *Applications of grassmann’s extensive algebra*, *American Journal of Mathematics* **1** (1878) 350–358.
- [187] W. Magnus, F. Oberhettinger and R. Soni, *Formulas and theorems for the special functions of mathematical physics*. Grundlehren der mathematischen Wissenschaften. Berlin, 1966.